FACOLTÀ DI SCIENZE MATEMATICHE FISICHE E NATURALI

BIOPHYSICS AND NANOSCIENCE CENTRE
(CNISM)

CORSO DI DOTTORATO DI RICERCA
SCIENZE AMBIENTALI – XXIII Ciclo

ADVANCED BIOPHYSICAL APPROACHES TO NANO-BIO-SENSING: POTENTIAL ENVIRONMENTAL AND BIOMEDICAL APPLICATIONS BASED ON P53-AZURIN INTERACTION

(FIS/07)

Coordinatore:
Prof. Maurizio Petruccioli

Tutors:
Prof. Salvatore Cannistraro

Prof.ssa Anna Rita Bizzarri

Dottorando:
Fabio Domenici

“What goes up must come down”

Isaac Newton

Riassunto

I recenti progressi nanoscientifici e tecnologici permettono oggi l'impiego di metodologie biofisiche avanzate ad elevato potenziale analitico in campo ambientale e biomedico.
Infatti i peculiari fenomeni fisici che operano su scala nanometrica (per questo detti a campo vicino) possono essere rilevati e controllati per aumentare sensibilità e accuratezza diagnostica molecolare e di conseguenza il livello d'informazione utile nella prevenzione e cura di patologie umane e ambientali.
Particolare attenzione rivestono le metodologie ottiche di amplificazione di segnale basate sull'impiego dei plasmoni di superficie. La risonanza plasmonica superficiale (SPR) è una oscillazione della densità di carica indotta da una radiazione elettromagnetica che può aver luogo su superfici metalliche a contatto con un dielettrico costituito ad esempio da molecole organiche e proteine. La capacità di assemblare nanostrutture metalliche e molecole ha permesso di utilizzare le intense bande di diffusione e assorbimento, prodotte dai plasmoni di superficie sotto opportune condizioni di irraggiamento elettromagnetico, per trasformare tradizionali tecniche strumentali, quali la spettrofotometria Raman e di assorbimento UV-Visibile, in metodologie ultrasensibili note con il nome di Surface-Enhanced Raman Scattering (SERS) e Surface Plasmon Resonance (SPR).
La metodologia SERS sfrutta l'enorme incremento della sezione d'urto Raman (che può raggiungere un fattore 10^{10}) subito da un analita quando sottoposto al forte campo elettromagnetico e al trasferimento di carica indotti dalla adiacente presenza di opportune nanostrutture metalliche irraggiate, quali nanoparticelle d'oro e argento.
La tecnologia SPR sfrutta invece l'eccitazione ottica dei plasmoni di superficie prodotta in opportune strutture planari, la cui energia di risonanza risulta altamente sensibile solo nell'intorno dielettrico a distanze nanometriche dalla superficie di eccitazione. Questo ha permesso di sviluppare una nuova tecnologia che consente di monitorare in tempo reale e quindi di acquisire accurate informazioni cinetiche e di equilibrio su complessi biologici con rilevanza biomedica e ambientale.
Recenti lavori hanno messo in luce la possibilità di coniugare i vantaggi di queste metodologie nanoscientifiche con quelli dei metodi bioanalitici basati sul riconoscimento molecolare specifico e selettivo, quali il tradizionale metodo ELISA, al fine di ottenere nuovi e più efficaci approcci bioanalitici.

A tale scopo, abbiamo considerato l'interazione fisica e funzionale tra la proteina umana p53 e la proteina batterica a trasferimento elettronico Azzurrina.

p53, descritto come "il guardiano del genoma", rappresenta uno dei fattori di trascrizione più studiati con attività di repressore tumorale. In condizioni cellulari normali, la sua concentrazione e attività tumorale sono inibite principalmente mediante un meccanismo di regolazione mediato dall'interazione di p53 con l'ubiquitina ligasi Mdm2. In presenza di danni del DNA indotti da fattori chimico-fisici ambientali e biologici, p53 viene stabilizzato e attivato inibendo l'interazione con Mdm2, permettendo così l'espressione dei suoi geni target preposti alla riparazione del danno o all'apoptosi. p53 è direttamente coinvolto nella catena dei processi biochimici scaturiti da un danno al DNA e riveste quindi un ruolo importante come potenziale bioindicatore in grado di discriminare la presenza di alcuni agenti genotossici e patologie tumorali. p53 riveste anche un ruolo centrale nella realizzazione di nuovi farmaci in grado di stimolare la sua attività antitumorale.

Riguardo quest'ultimo aspetto è stato recentemente dimostrato che Azzurrina, membro della famiglia delle "blue copper protein", può essere internalizzata preferenzialmente in cellule tumorali, dove induce apoptosi con efficacia verificata *in vitro* e *in vivo*. L'azione apoptotica di Azzurrina (Az) è concomitante alla formazione di un complesso con p53, che porta alla stabilizzazione di quest'ultimo, agendo quindi in apparente opposizione rispetto all'azione di down-regolazione indotta dal legame Mdm2-p53. Studi molecolari hanno evidenziato che l'interazione tra Az e p53 è stabile ma fino ad oggi le caratteristiche stereochimiche e cinetiche di tale interazione non sono state completamente chiarite, pur essendo importanti per la comprensione del meccanismo anticancro di Azzurrina.

Partendo da questi concetti, in questo lavoro abbiamo sfruttato le potenzialità analitiche di questa interazione per la rilevazione ultrasensibile di p53 mediante un nuovo metodo nano-bio-sensoriale basato sul fenomeno SERS e supportato anche dalla spettrofotometria UV-Visibile e dai metodi a scansione di forza quali la Microscopia a Forza Atomica (AFM). In particolare abbiamo analizzato l'intenso segnale SERS prodotto dalla coniugazione covalente di p53 e nanoparticelle d'oro (Np) utilizzando come linker il marcatore Raman para-amminotiofenolo (4-ATP), già impiegato con successo nella realizzazione di "substrati SERS". Abbiamo quindi realizzato un substrato di cattura, utilizzando Azzurrina come proteina partner, sul quale abbiamo incubato il sistema p53-(4-ATP-Np) in condizioni fisiologiche. Seguendo le bande SERS caratteristiche del sistema p53-(4-ATP-Np), legato all'Azzurina, abbiamo rilevato p53 inizialmente presente a concentrazioni

subpicomolari, mettendo in evidenza che la metodologia utilizzata è ultrasensibile, rapida e di ampio respiro in ambito diagnostico.

Utilizzando la tecnologia SPR abbiamo studiato l'interazione Az-p53, rilevando i corrispondenti parametri cinetici e di affinità. Inoltre, allo scopo di fornire nuove informazioni riguardo al meccanismo di stabilizzazione di p53 in cellule tumorali, abbiamo valutato l'effetto della presenza di Azzurrina sull'interazione funzionale Mdm2-p53, utilizzando strutture proteiche intere nel loro corretto folding nativo. A tale scopo, abbiamo estratto le costanti di velocità di reazione dei complessi Mdm2-p53 e Az-p53, e li abbiamo comparati con quelle ottenute dall'interazione tra Azzurrina ed il preformato complesso Mdm2-p53, e tra Mdm2 ed il preformato complesso Az-p53. L'analisi ha rivelato che Azzurrina può legare p53 in maniera specifica e stabile senza subire variazioni cinetiche e di affinità significative anche in presenza di Mdm2, suggerendo quindi che Azzurrina ed Mdm2 non interagiscono con la stessa regione di p53. Questo risultato è stato confermato anche mediante studi competitivi eseguiti a livello di singola molecola utilizzando la Spettroscopia a Forza Atomica (AFS). Nonostante il sito di legame per p53 non sia lo stesso, quando Azzurrina lega p53 l'interazione tra Mdm2 e p53 viene significativamente influenzata poiché la costante di velocità di associazione tra le due proteine viene ridotta di più di 4 volte. Questo significa che Azzurrina può esercitare un'azione d'inibizione parziale del legame Mdm2-p53 attraverso un meccanismo a distanza che implica la formazione di un legame Az-p53 che può essere localizzato o sul dominio N-terminale di p53 ma in posizione distinta da quella preposta per l'interazione con Mdm2, oppure sul suo "DNA-binding domain" (DBD), come predetto da recenti lavori computazionali.

Inoltre sono state eseguite misure di dicroismo circolare allo scopo di verificare eventuali modificazioni strutturali indotte da Azzurrina sulla struttura di p53. Quest'indagine ha infatti evidenziato che p53 in presenza di Az è soggetta ad un aumento del 10% del folding secondario nativo. Ciò fa pensare che il meccanismo d'inibizione possa essere di tipo allosterico e suggerisce interessanti prospettive per la progettazione di farmaci in grado di riattivare le funzioni di repressore tumorale di p53, ad esempio nei tumori che sovraesprimendo Mdm2 mantengono inibita l'attività di p53.

Alla luce dei risultati ottenuti in questo lavoro, che hanno una rilevanza sia in campo diagnostico che terapeutico, crediamo che l'approccio nanoscientifico per la ricerca di analiti a bassissime concentrazioni possa realmente costituire uno strumento a tutela della salute umana.

Abstract

The availability of advanced methodologies, especially suited for sensitive and reliable screening of indicators of both environmental and human pathologies, is a crucial element for an effective early detection. For this reason, nanoscience and nanotechnology research combines efforts to improve environmental and biomedical diagnostic, often resorting to advanced biophysical approaches which have the potential to overcome detection limits of traditional methods. In particular, signal amplification methods, such as Surface-Enhanced Raman Scattering (SERS) and Surface Plasmon Resonance (SPR), are now entrenching in modern environmental and biomedical fields. By taking advantage of the peculiar optical properties of metal structures at the nanoscale, in fact, they offer the possibility of developing ultrasensitive nano-bio affinity assays.

Given the importance of health and safety in human society, considerable resources have been and are being expended in efforts to identify and classify human carcinogens, in order to reduce the risk of cancer. As the tumour suppressor protein p53 is directly involved in the chain of biochemical events that follow genotoxic damage, some researchers have tried to incorporate this information into testing protocols, evidencing a close correlation between the DNA damaging mechanism and the p53 induction pattern of a given chemical. Hence, p53 has a huge potential as a biological indicator of environmental conditions which threaten human health, and the novel biophysical approaches offer the adequate features to turn such p53 potential into novel, more accurate, quick and efficient methods to early screen substances for carcinogenicity.

In this connection, we have explored the analytical potential of advanced biophysical methods in an attempt to more deeply understand the improvement they can provide to traditional bio-affinity assays; successively, by means of these approaches, we have tried to reduce the detection threshold of the tumour marker p53.

To probe the presence of p53, we have used the blue copper protein Azurin (Az), whose physical interaction with the tumour suppressor has been recently proposed in connection with its demonstrated anticancer activity. By SPR, we have analysed the Az-p53 binding kinetics and ascertained the strong stability of their specific interaction even in presence of the protein Mdm2, which is one of the main regulators of p53; then we have exploited the specific interaction between Az and p53 to realize a novel SERS-based immunoassay detection method, made up by the synergic combination of SERS methodology and

bioaffinity assays. In this way it has been possible to strongly reduce the current detection limit for p53 down to levels which are appealing also for screening in human serum.
The importance of investigating the Az-p53 interaction is not limited to analytical detection aspects. Indeed our SPR measurements performed on the proteins p53, Mdm2 and Az indicate that these three proteins are likely engaged in a ternary structure where the interaction of Az with p53 modulates the Mdm2-p53 binding kinetics. Since the tumour repression activity of p53 is mainly down-regulated by Mdm2, the latter result could provide an useful insight into the possibility of designing new anticancer drugs.

This thesis is structured as follows:

- A general introduction dedicated to the general aspects of plasmonics-based signal amplification methods for improving molecular detection of conventional biosensing techniques, with particular emphasis on the experimental strategies developed and optimized to study the Az-p53 complex and its actual application in environmental and biomedical fields.
- Materials, methods and experimental techniques chapter.
- Results and discussion concerning the use of localized plasmonic on the ultrasensitive detection of wild type p53, performed using a micro-Raman equipment, and supported by absorbance spectroscopy and atomic force microscopy measurements.
- Results and discussion concerning the use of surface plasmons waves for binding kinetics investigations of Az-p53 interaction, also in presence of Mdm2, by using the SPR equipment.
- General conclusions of the research activity and perspectives.
- An appendix concerning the Surface plasmons: physical principles and applications.
- An appendix dedicated to the principles and applications of atomic force microscopy.

Contents

CHAPTER 1

General introduction

1.1 Nanoscience and bio-sensing

A great deal of the biophysics efforts, aimed at improving analytical detection limits in environmental and biomedical fields, is addressed toward the development of novel signal-based amplification methodologies leading to high sensitive and information-rich diagnostic assays (Giljohann and Mirkin, 2009; Nel et al., 2009; Wang et al., 2010). It is known that the human exposure to environmental stress factors, such as physical-chemical pollutants, is one of the main causes of pathological effects, whose gravity can be directly correlated to the intensity and the duration of their promoting causes (Moore and Simpson, 1992). Therefore, the availability of advanced methodologies, especially suited to the detection of indicators of both environmental and human pathologies, at very low concentrations, is a crucial element for the diagnosis of a disease when it is not yet significantly advanced.

Beside more traditional spectrophotometric, chromatographic and electrochemical analyses, which have a quantitative threshold sensitivity of 10^{-6} M with 1% margin of error, in the last years new analytical methods have been developed, aimed at decreasing such a threshold sensitivity. The approaches used to reach this goal take advantage of either instrumental sensitivity improvement or biologically-based analytical detection methods (Van Emon et al., 1998). Since 1980s, biologically-based analytical techniques, employing the high molecular affinity and specificity of antibody-antigen interaction to identify and separate compounds, have gained favour in environmental detection (Van Emon et al., 1998). Consequently, the development of immunoassay methods has revolutionized many laboratories and fields of analysis (Van Emon et al., 1998; Soper et al., 2006). The most common immunoassay format in environmental analysis is the ELISA (Enzyme-Linked ImmunoSorbent Assay). Quantitation by ELISA usually overcomes the sensitivity, selectivity, and reduces costs of previously used methods (Van Emon et al., 1998; Soper et al., 2006). To date, it permits detection of environmental analytes down to 10^{-10} M concentration, allowing the screening and quantitative analysis of pesticides, including: alachlor, aldrin, atrazine, benomyl, chlordane and 2,4,5-T. However, the conventional bioaffinity-based methods, which can be used to reveal also many biological

indicators of human exposure to such pollutants or other toxic and carcinogenic agents, require multiple steps, sample pretreatments and long incubation periods, providing only a semi-quantitative assay (Kenny and Dunsmoor, 1983; Yang et al., 1998; Guihong et al., 2004).

Today, thanks to nanoscientific and technological progresses, we dispose of novel signal-based amplification methods by which it may be possible to further increase the molecular detection sensitivity (Giljohann and Mirkin, 2009). Nano-approaches take advantage of the physical phenomena that are prevalent in the matter interaction at the nanoscale, to promote, control and distinguish recognition events (Giljohann and Mirkin, 2009; Nel et al., 2009). In particular, the ability to engineer metal surfaces (especially nanostructures) and biological molecules has led to the rapid development of innovative biosensing strategies based on the peculiar optical properties of metal structures at the nanoscale, called 'plasmonics' (Polman, 2008).

Surface plasmons are optically induced oscillations of the free electrons at the surface of suitable metal substrates and metal nanostructures, in which the plasmonics can be excited, directed and manipulated in function of the metal composition, shape and dielectric environment (Polman, 2008). The attractiveness of plasmonics is that they can effectively confine the optical excitation in a nanoscale volume and thus mediate strong optical interactions within this volume (see also Appendix A). In particular, the Localized Surface Plasmon Resonance (LSPR) of noble nanoparticles exhibits strong absorption bands and scattering properties that are not present in the bulk metal. Thus, such phenomenon has opened the possibility of developing protein-modified sensors with detection limits that are many order of magnitude lower than those of techniques like ELISA (Aslan, 2005; Klein, 2007; Nel et al., 2009). With regard to this last point, the enormous benefits of combining both plasmonic and molecular recognition based methodologies has been explored by recent pioneeristic works, evidencing the strong impact they could provide within the field of environment and biomedicine.

At variance of applied plasmonics, other nanoscientific approaches such as near field force (Bizzarri and Cannistraro, 2010) and conductive scanning spectroscopies and microscopies (Choi et al., 2008), which allow to detect the presence and the interaction between single molecules, are not commonly considered as high-sensitivity methods (Giljohann and Mirkin, 2009) for environmental and biomedical screening. However, the methodologies based on Atomic Force Microscopy (AFM) (see Appendix B), when used in support of

plasmonic-based tools (Bizzarri and Cannistraro, 2009), may be useful to open new analytical strategies for improving both diagnostics and therapeutics.

1.1.1 Plasmonic based methodologies

LSPR of noble nanoparticles exhibits strong absorption bands and scattering properties that are not present in the bulk metal. In particular, plasmon scattering cross section is responsible for the high increase of the Raman signal, achieved by Surface-Enhanced Raman Scattering (SERS) (Otto et al., 1992). In this phenomenon, which has been discovered quite recently, the optical properties of molecules placed in the vicinity of nanostructured metal surfaces are modified, causing an unusually large Raman cross section of analytes (see also paragraph A.2). It provides a strong increasing of conventional Raman detection sensitivity to an extent which depends on the chemical nature of the adsorbed molecules, the type of metal surface and its nature. The greatest enhancement occurs for molecules adsorbed on silver, gold or copper (Van Duyne et a., 1986). SERS allows circumventing many of the problems of conventional Raman vibrational spectroscopy (see paragraph A.2.1); indeed the sharp SERS signals obtained are molecularly specific, providing an easy way to discriminate from any broad background florescence, due to the non-adsorbed material, thus allowing *in situ* identification of specific analytes in a mixture (Fig. 1.1 panel A and B).

The large enhancements in Raman scattering can be substantially improved by coupling analytes to a metal so as to form systems able to give also a molecular resonance enhancement. With visible excitation, enhancements for SERS are often estimated as about 10^6 or slightly more, whereas enhancement for Surface Enhancement Resonance Raman Scattering (SERRS) as 10^{10}-10^{11}.

One of the major points in the application of SERS microspectroscopy for analytes detection is the preparation of metallic surfaces or media, called ‘SERS-active substrates’ or ‘SERS-active surfaces’, that have an easily controlled protrusion size and reproducible structures on the sub-micron scale.

Another peculiar point of this optical approach is the use of SERS labels, characterized by strong Raman bands, which are suitable to identify analytes at very low concentration.

Analytical labelling procedures may reduce the accuracy of detection and limit the application fields of the SERS approach, but such drawbacks can be overcome by measuring the change of the plasmon oscillations at the metal surface due to the presence of a specific analyte.

Localized plasmon absorption cross section of gold nanoparticles is responsible for the appearance of intense and adsorbate-dependent Surface Plasmon Absorption Bands (SPAB) in the UV-Vis optical region (see Fig. 1.1 panel A and panel B) (Slistan-Grijalva et al., 2005) (theoretical details are reported in paragraph A.2.3). Due to their potential to detect the presence of adsorbed species when the surface coverage is one monolayer or less, plasmon absorption feature of nanoparticles has recently emerged as a useful tool for a variety of chemical and biological sensor relevant applications (Cooper, 2003; Homola, 2003).

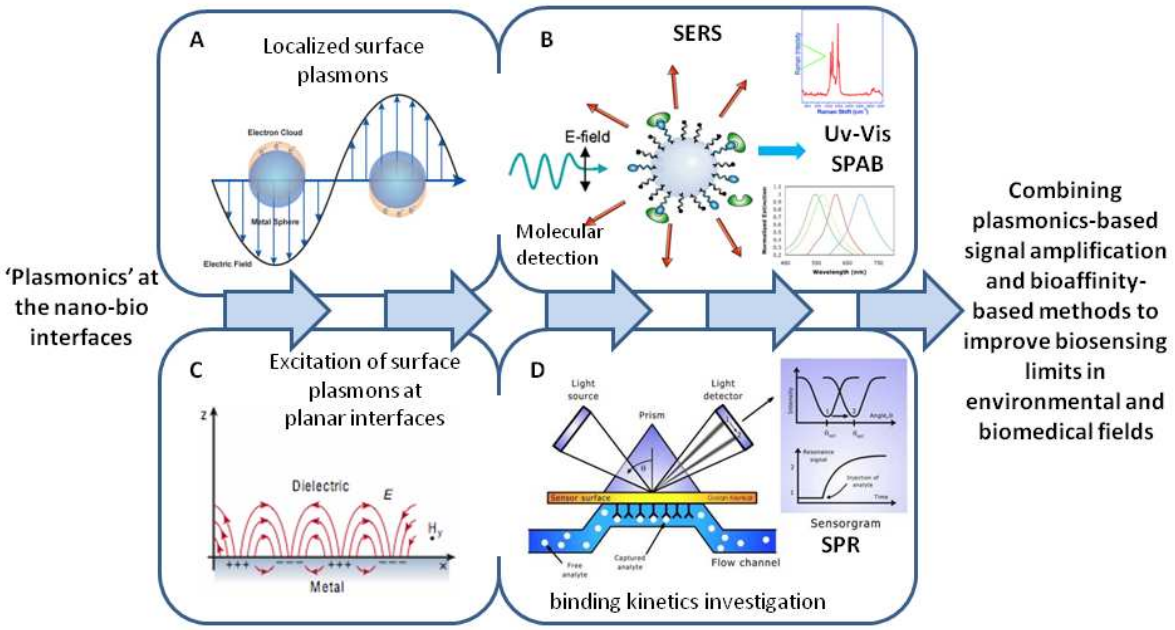

Fig. 1.1. Surface Plasmon is a coherent electron oscillation that propagates along suitable metal nanostructures (A) and planar substrates (C) together with an electromagnetic wave; derivatization of such metal surfaces with biomaterials provides nano-bio interfaces that improve molecular detection sensitivity and selectivity of conventional spectroscopies (B) and of bioaffinity-based assays (D).

Parallel to the studies of localized plasmonics in optical transmission and scattering geometries, Surface Plasmon Wavelength (SPW) propagation along noble metallic surfaces has been also recently employed by means of improved Surface Plasmon Resonance (SPR) equipments which are able to work in Attenuated Total Reflection (ATR) optical geometries (see Fig. 1.1 panel C and D). In such a configuration, SPR technology has gained a signal enhancement of up to about 40-times over the conventional absorption spectroscopies, becoming rapidly the most tremendous plasmon application in biochemical field (Wang et al., 2001; Cooper, 2002; Cooper, 2003). In a typical SPR experiment, a biomolecular recognition process can be followed in real time by registering

the time varying shift of the optical SPR angle which characterizes only the optical property of the region very close to the sensor surface, where the reaction occurs (see also paragraphs A.1.1 and A.1.3). Thus, SPR represents a strategic tool in protein-binding studies, especially suited for sensitive kinetic process investigations, in real time and without labeling procedures (Wang et al., 2001; Cooper, 2003).

1.1.2 Molecular recognition

A common event in living systems is the non-covalent binding of one or more molecules to a single macromolecule. A molecule bound to a macromolecule is called a ligand. In the cases usually studied, the ligand is a small molecule such as the substrate or a cofactor of an enzyme. The ligand may also be a macromolecule, as in the case of a regulatory molecule, such as a repressor protein binding to DNA. The study of ligand binding is important to understand the macromolecular mechanisms of action in regulatory systems which often require the knowledge of structural and kinetic features of the binding process, and it is also of special pharmacologic relevance to design novel clinical drugs.

There are many types of binding. For example, a molecule may have only a single or multiple binding sites. Experimentally the measurement of binding is straightforward, but in spite of this, interpretation of the data requires different modes of analysis that depend on various features of the binding process. However, if the binding of the ligand to one site does not affect the binding to the others, each single interaction can be treated as a simple one-to-one. If we consider this general and common case, the complex formation between two macromolecules P and A, at saturation one mole of P combines with one mole of A following the reaction:

$$P + A \leftrightarrow PA \tag{1.1}$$

The concentration of the different specimens at equilibrium provides information about the affinity of their interaction, as indicated by the law of mass action commonly expressed as follow:

$$K_d = \frac{[P][A]}{[PA]} \tag{1.2}$$

Where K_d is known as the dissociation constant. In chemistry the equilibrium constant K_a=1/K_d is usually used whereas biochemists and molecular biologist prefer to use K_d as a measure of the affinity level of the binding interaction.

A higher K_a suggests a higher affinity, while a higher K_d is associated to a lower affinity. Just to give some examples, the dissociation constant observed for antigen-antibody

complexes are in the range of 10^{-7}-10^{-12} M, whereas those found for enzyme-substrate interactions are in the range of 10^{-1}-10^{-6} M (Houk et al., 2003).

The equilibrium constants are related to the standard free energy (ΔG^o) of the reaction. If we consider the complex formation, the relation can be expressed as:

$$\Delta G^o = -RT \ln(K_a) \tag{1.3}$$

where R is the gas constant and T the absolute temperature. It means that more negative is the standard free energy, more favorable is the protein-protein association. The change in free energy is due to an interplay of entropic (S) and enthalpic (H) contributions, since:

$$\Delta G^o = \Delta H^o - T\Delta S^o \tag{1.4}$$

Various factors play a role in defining these parameters for a given complex formation. Hydrogen bonding, electrostatic and van der Waals interactions complementarily at the binding interface give a contribute to the enthalpy, whereas burial of hydrophobic groups and conformational disorder affect the entropic term.

Additional insights are provided by the kinetic of a complex formation and rupture. Biological systems are not at equilibrium and, for this reason, it is particularly informative to know the rate of proteins binding and dissociation. The concentration of a complex depends on the velocities of its formation (v_{on}) and rupture (v_{off}), as follows:

$$\frac{d[PA]}{d[t]} = k_{on}[P][A] - k_{off}[PA] = v_{on} - v_{off} \tag{1.5}$$

where k_{on} and k_{off} are the association and dissociation rate constants, respectively. They, in fact, multiplied by the substrates concentration, give the velocities of the complex formation and dissociation. At equilibrium, these two velocities are equal, so that the concentration of the complex does not change (d[PA]/dt = 0). Under these conditions, by comparing equations (1.2) and (1.5), we can easily deduce that the rate constants are related to the dissociation constant by:

$$K_d = \frac{k_{off}}{k_{on}} \tag{1.6}$$

It implies that interactions may have similar affinity, while displaying different timescales. However, often the association rates do not vary very much among different kind of protein complexes, since they are mainly governed by unspecific factors. For reactants in solution, the association rate is especially influenced by their diffusion through the medium. Then, other elements, such as the relative orientation of the binding sites during the encounter and long-range forces, due to the charges on the reactants surface, can

contribute to define the association rates, most commonly found in the range of 10^4-10^8 $M^{-1} \cdot s^{-1}$ (Janin, 1995). Much effort has been exerted to measure association rates between receptors and ligands in solution (three-dimensional k_{on}). More recently, different techniques involving atomic-force microscopy, surface plasmon resonance and fluorescence measurements, have also yielded quantitative information on association rates between surface-bound molecules (two-dimensional k_{on}). It is now well-recognized that relating association rates measured in solution (i.e., three-dimensional conditions) to the behavior of membrane-bound receptors (i.e., two-dimensional reactions) is difficult.

To deal with this problem it has been recently suggested (Robert et al., 2009) that in addition to conventional k_{on} it is possible to define the probability of bond formation between a ligand and a receptor maintained at binding distance during a sufficiently short time interval of duration t, thus extracting the minimum contact time for bond formation. In this respect a single-bond formation in two-dimensional reactions could be modeled as a multi-kinetic trap resulting in different threshold contact times.

Nevertheless, for a correct binding data extrapolation in a two dimensional binding experiment both transport process of flow and diffusion should be taken into account to figure out the net analyte flux (Myszka et al., 1998). In particular, binding of analyte to the immobilized ligand is in principle a two step event. First, the analyte is transferred out of the bulk solution towards the ligand surface. Second, the binding of the analyte to the ligand takes place. The first step is also known as mass transfer (and is carried out by convection and diffusion). Both events have their own rate constants. The coefficient for mass transfer k_t, which describes the first one, is the same in both binding and unbinding directions of the reaction. A common operative model used for kinetic investigations is explained in paragraph 2.3.3.

By contrast, the rates of dissociation are stringently dependent on the properties of the interaction, like the shape and electrostatic complementarity of the binding interface, and the number and strength of the bonds holding the proteins together.

It means that the dissociation rate constants of protein complexes, falling within 10^3-10^{-7} s^{-1} (Janin, 1995), are the main responsible in defining the equilibrium dissociation constant, (and thus the affinity), and in turn the life-time ($1/k_{off}$) of protein-protein interactions. This is because protein dissociations need the overcoming of an energy barrier. The dissociation rate constant, in fact, depends on the activation energy ΔG^* of the reaction, as follow:

$$k_{off} = A\exp\left(\frac{-\Delta G^{*}}{k_B T}\right) \quad (1.7)$$

where A is the Arrhenius prefactor, k_B the Boltzmann constant and T the absolute temperature. It indicates that higher is the energy barrier, slower is the complex dissociation.

As mentioned, many biological molecules have more than one binding site. In this latter case the binding sites are considered interactive when the occupation of one site influences, by a cooperative mechanism a second site. In particular, many cellular processes are mediated by allosteric protein interactions (Hilser, 2010). In this latter case, binding of the first ligand molecule A (often called effector) alters the shape of the protein P and this results in a change of the site where a further ligand B may interact. In other words, upon binding A, the protein P undergoes a binding affinity modulation of the further PB complex formation. Allosteric mechanisms can be figured out by two different theoretical approaches called symmetric (or concerted) model and sequential model. Both models follow the assumption that:

(1) each protein P exists in two forms, usually called (*T*) and (*R*), able to bind a ligand with low and high affinity, respectively;

(2) if a ligand molecule is firmly bound to a subunit of a protein P, that subunit must be in the (*R*) form.

In the concerted model it is assumed that:

(1) (*T*) and (*R*) forms of the P protein are in equilibrium,

(2) significant binding only occurs to the (*R*) form,

(3) the binding between P and the effector ligand A shifts the equilibrium strongly in the (*R*) direction.

In contrast, the sequential model assumes that binding tends to occur first in the (*T*) state of P, thus inducing the conformational transition in the (*R*) state.

1.2 Environmental and biomedical relevance of the proteins p53 and Azurin

p53, “the guardian of the genome”, is probably the most extensively characterized transcription factor with a tumour-suppressor activity (Toledo and Wahl, 2006). It consists of four main domains which are responsible for its transcriptional activation, DNA-binding and tetramerization functions (Fig. 1.2) (Veprintsev et al., 2006).

Fig. 1.2. Functional domains of the protein p53. TA = trans-activation domain (residues1-50); PR = proline-rich domain (residues 61-94); DB = DNA-binding domain (residues 97-300); T = tetramerization domain (residues 324-352); R = regulatory domain (residues 363-393).

Thanks to its tumour suppressor role, p53 has been intensely investigated to understand the network regulating cell proliferation, also with the intent of optimizing anti-cancer strategies. Indeed, mutations in *TP53* that compromise p53 function occur in 50% of human cancers, and the alteration of regulators of p53 occurs in many of the remainder. For example, the *MDM2* gene, which encodes a ubiquitin ligase, is amplified in at least 7% of all cancers without concomitant *TP53* mutation (Toledo and Wahl, 2006).

When DNA damage is sensed by the cell, the p53 level rises and the protein binds to sequence-specific regulatory sites in the genome, thereby inducing the expression of genes that control the DNA repair and interrupting the cell growth until the damage is repaired; on the other hand, if the damage is too severe, p53 triggers the apoptotic cascade (Vogelstein et al., 2000; Lavin and Gueven, 2006). In other words, after the exposure of cells to DNA-damaging agents such as γ and UV irradiation, heat shock, genotoxic drugs and nutrition deprivation, the repair mechanism is induced by an increase in p53 level (see Fig. 1.4). For example, the presence of well note atmospheric carcinogen pollutants as polycyclic aromatic hydrocarbons or nitric oxide free radical (Hofseth et al., 2002), can lead to an increase in p53 levels in a number of animal or cell systems. More particularly, a close correlation between the DNA damaging mechanism and the p53 induction pattern of a given chemical has been shown (Yang et al., 1998), even evidencing the capability to discriminate between genotoxins and non-genotoxins, as both direct- and indirect-acting genotoxins of environmental interest.

The level of p53 is thought to be mainly down-regulated by post-translational modification mediated by the oncoprotein Mdm2, whose direct association with p53 promotes its ubiquitination and proteolysis (Freedman et al., 1999); although this, potent pollutants can exert a cancerogenic activity in human cells through the inhibition of p53 accumulation which is not associated with down-regulation mediated by Mdm2 (Mukherjee et al., 2006). Hence, p53 has a huge potential as a biological indicator of environmental conditions which threaten human health, although the main challenge for employing such a p53 potential consists in overcoming detection limits of traditional methods such as Western blot and ELISA.

Likewise, in biomedical field, the improvement of p53 detection sensitivity is of special interest to the early oncologic diagnosis, since its tissue and serum level estimation has been associated with the tumour invasiveness and prognosis on patients with various malignant diseases (Shurbaji et al., 1995; Zusman et al., 1996; Shimada et al., 2000; Malviya et al., 2004; Psyrri et al., 2007). Moreover the existence of wild-type p53 in a significant fraction of human tumours has stimulated the search for a new class of agents to selectively activate it. In this last context, recent *in vivo* and *in vitro* studies (Yamada et al., 2002; Yamada et al., 2004) have demonstrated that the blue copper protein Azurin (Az) (Fig. 1.3) is an exogenous vector with the capabilities to bind p53, and inhibit cancer cell proliferation, likely through a post-translational increasing of p53 level.

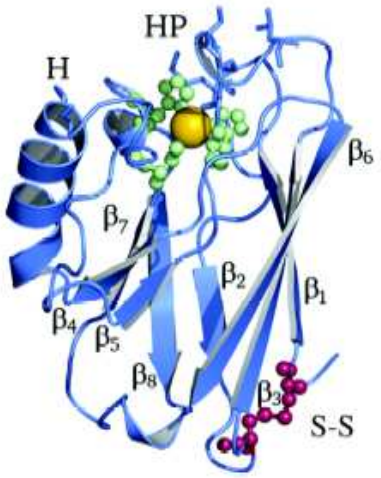

Fig. 1.3. Three-dimensional structure of azurin. The yellow ball represents the copper atom, while the residues coordinating it are depicted as green balls and sticks. At the opposite side the balls and sticks represent Cys3-Cys26 involved in the disulphide bridge (S-S) of the protein.β_1- β_8 = β-strands, H = α-helix, HP = hydrophobic patch.

The specificity and the stability of Az-p53 interaction has been demonstrated by Dynamical Force spectroscopy (DFS) and SPR analysis (Taranta et al., 2008a; Funari et al., 2010; Domenici et al., 2011).

These results suggest that Az can be chosen as a protein probe for bioaffinity-based p53 detection, with several advantages with respect to the use of p53 antibody. Indeed, Az structure exhibits high stability under a wide range of physico-chemical conditions (Adman, 1991), and it has resonance Raman fingerprint bands (Bizzarri et al., 2008) which allow to discriminate its presence (in the wild-type folding) in detection processes.

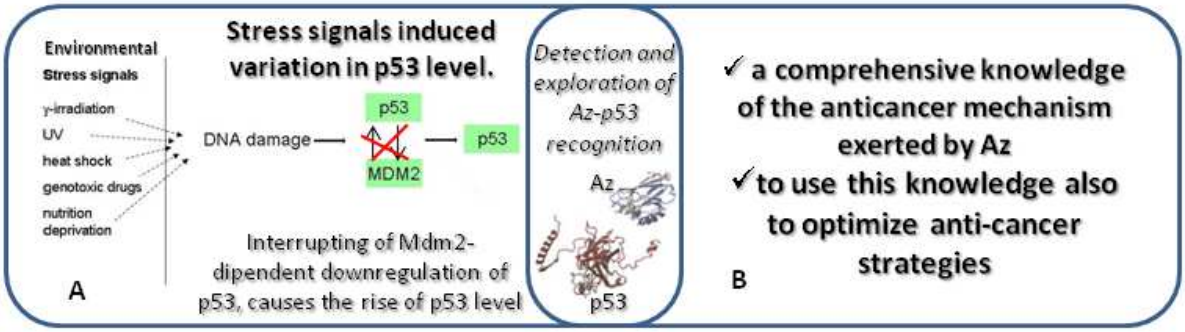

Fig. 1.4. Environmental and biomedical application based on the Az-p53 interaction: detection of p53 in response to genotoxic environmental agents (panel A); investigation of the Az-p53 tumour repression activity (panel B).

1.3 Aim of the research

Signal improving methods based on plasmonics are now entrenching in modern environmental and biomedical fields (Wang et al., 2010), thus opening to the possibility of providing new anticancer strategies. For this reason, particular attention has been devoted to the monitoring and the exploration of the interesting physical and functional interaction between Az and p53 (See Fig. 1.4 panel A and B). Indeed p53 is a sensitive biological indicator of both tumour promoting environmental agents and human pathologies and can be recognized by Az even enhancing its tumor suppressor activity in cancer cells.

Thus, we have explored the analytical potential of both scattering and absorption optical properties of plasmonics, in an attempt to more fully understand the effective improvement they can provide to biosensing techniques that use optical radiation, such as Raman or absorption-based spectroscopies. We have used the SERS methodology also combined to AFM, providing an approach to improve the detection limit of the tumour marker p53 recognized by Az. This proof of concept study lays the foundations for the development of innovative experimental procedures for an ultrasensitive, easy and rapid screening of many different molecules of environmental and biomedical interest.

Moreover, by the innovative SPR technology, we have studied the binding kinetics of the Az-p53 interaction in the attempt to provide new insights about the anticancer action of Az (See Fig. 1.4 panel B), and have also investigated the Az potentiality to interfere with the binding of p53 to Mdm2, the latter playing a key role in lowering the intracellular stability of p53. Our results provide new details useful to design anticancer drugs for the treatment of those tumors in which p53 has retained its wild-type structure and function.

Moreover, the present study provides a further evidence that the nano-bio-sensing strategies may be widely applied in the future, for a more comprehensive risk assessment for the environment and human health.

Chapter 2

Materials, methods and experimental techniques

2.1 Proteins expression and purification

Az was purchased from Sigma-Aldrich (St. Louis, Mo), dissolved in PBS 50 mM buffer (pH 7.2) and used without further purification. A characteristic spectral absorption ratio of 0.48 at 630 nm and 280 nm was found for Az solution, indicating a good degree of purity of the protein corresponding to a stable oxidized form (Guzzi and Sportelli, 1992).

Glutathione S-transferase (GST) fusions of human Mdm2 (kindly provided by A.L. Haas, LSU Health Sciences Center, New Orleans, LA, USA) and human wild-type-p53 (kindly provided by G. D'orazi and S. Di Agostino, National Cancer Institute "Regina Elena", Rome, Italy) were expressed in log phase *Escherichia coli* BL-21 that had been grown overnight at room temperature, diluted 1:20 in fresh Luria-Bertani medium containing 50 μg/ml ampicillin at 37°C with vigorous shaking. Isopropyl-1-thio-β-D-galactoside (IPTG) was added to a final concentration of 0.4 mM when the OD_{600} reached 0.4-0.8 value. Bacteria were harvested 3 hours after addition of IPTG by centrifugation at 5000 rpm for 10 min. Cell pellets were resuspended with NENT buffer (Tris 20 mM at pH 8.0, NaCl 100 mM, EDTA 1 mM and NP40 0.5%), proteases inhibitors, phenylmethylsulfonylfluoride (PMSF) 1 μM and lysozyme and lysed by sonication. The sonicate was clarified by centrifugation at 4°C for 15 min at 5000 rpm and stored at -80°C. Levels of expressed GST fusion proteins were estimated by incubating sonicates with glutathione-Sepharose (GS) beads (Sigma), washing, and quantification by SDS-PAGE followed by staining with Comassie Brilliant Blue R-250. Known amounts of bovine serum albumine (BSA) were used as standards. Cleavage of the GST portion was achieved by digestion with thrombin CleaveClean kit (Sigma) according to the manufacturer's instructions. Yields of the GST-purified proteins were 0.3 mg of GST-p53 and 2.3 mg of GST-Mdm2 per 10 g wet culture. Additional p53 amount was obtained after thrombin cleavage of commercial p53-GST purchased from Millegen (Labège, France).

The GST- and thrombin-purified proteins were separated by SDS-PAGE and analyzed by densitometry (Fig. 2.1). All thrombin-cleaved preparations were of ≥ 95% homogeneity.

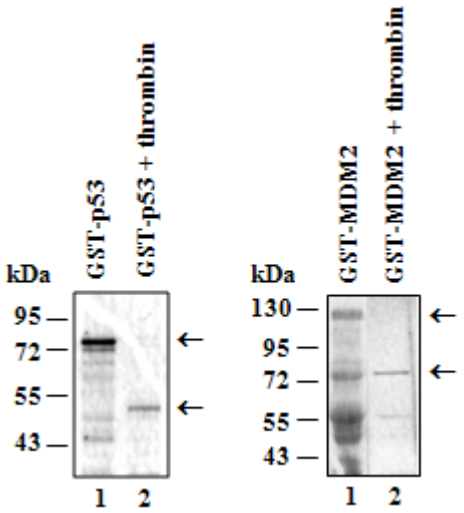

Fig. 2.1. Purity of p53 and Mdm2. Recombinant wild-type glutathione *S*-transferase (GST)-p53 and -MDM2 proteins (10 µg each) purified from lysates with glutathione beads (lane 1) and after purification with thrombin digestion (lane 2) were separated on 10% and 8% SDS-PAGE for p53 and MDM2, respectively, and stained with Comassie brilliant blue. The GST-proteins and the purified ones are highlighted by the arrows along molecular mass markers scale (kDa) in the gel pictures.

The correct conformation of the obtained proteins was assessed by Circular Dichroism (CD) and immunoprecipitation techniques (Funari et al., 2010).

2.1.1 Proteins secondary folding by CD spectroscopy

The folding of the proteins was checked by characterizing their secondary structure through CD studies. CD measurements on p53 and Mdm2 protein solutions were performed using a JASCO J-715 spectropolarimeter, equipped with a 0.1 cm path length and thermal controlled quartz cell. CD spectra were recorded at 25^{o}C in TST buffer at pH 7.2 (50 mM Tris buffer with 150 mM NaCl and 0.1% Triton x 100) and at 0.50 µM proteins concentration obtained by quantitative dilution of the mother solution to prevent protein aggregation contributions.

All spectra were the average of ten repeats obtained by collecting data from 250 nm to 190 nm at 0.5 nm intervals, at a rate of 50 nm/min with a response time of 2 s for each point.

p53 and Mdm2 CD profiles are shown in Figs. 2.2 and 2.3, respectively. The experimental patterns acquired in millidegrees of ellipticity θ, were corrected by solvent subtraction and converted to mean residue ellipticity $[\theta]_{MRW}$. The predicted content of secondary structure was calculated using the CD spectra deconvolution software CDSSTR (Whitmore and Wallace, 2004), with a normalized root mean square deviation value of 0.01. The best fit values of both proteins are summarized in Tab. 2.1.

Secondary structure [%]	p53	Mdm2
α-Helix	16	24
β-Sheet	30	20
Unordered	54	56

Tab. 2.1. Secondary folding of full-length p53 and Mdm2, extracted from CD spectra by CDSSTR software.

The high percentage values of unordered structure indicate the presence of large unfolded regions, as described in the literature for wild-type p53 and Mdm2 (Bothner et al., 2001; Bell et al., 2002; Dawson et al., 2003). p53 and Mdm2 are classified, in fact, as intrinsically unstructured proteins with a percentage greater than 45% of residues predicted to be unfolded (Iakoucheva et al., 2002).

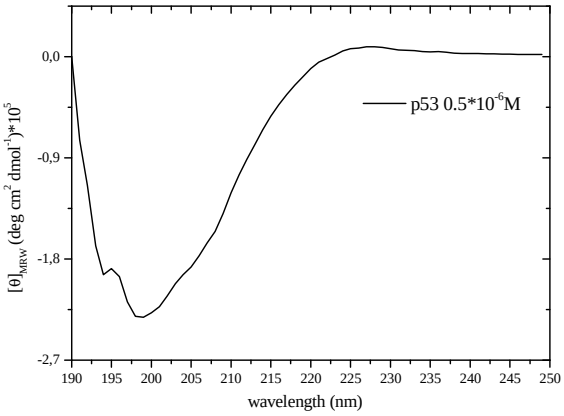

Fig. 2.2. Far-UV CD spectrum of p53 protein (0.5 µM) in TST buffer, as measured by a Jasco J-715 spectropolarimeter. The spectrum was corrected for buffer contribution.

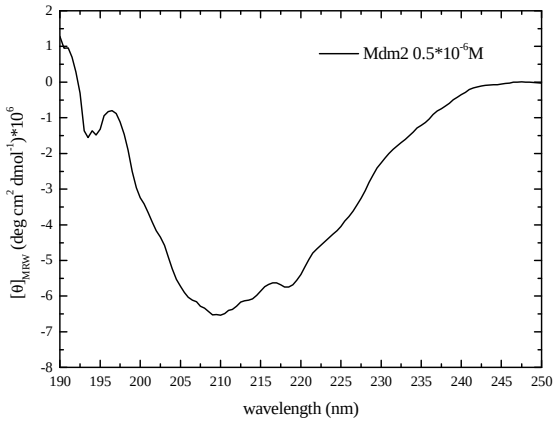

Fig. 2.3. Far-UV CD spectrum of Mdm2 protein (0.5 µM) in TST buffer, as measured by a Jasco J-715 spectropolarimeter. The spectrum was corrected for buffer contribution.

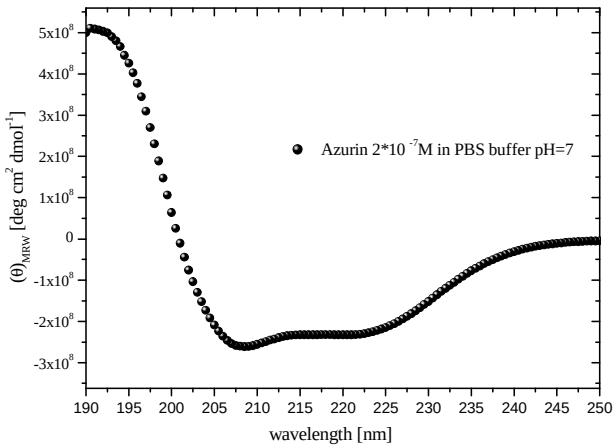

Fig. 2.4. Far-UV CD spectrum of Az protein (0.5 µM) in TST buffer, as measured by a Jasco J-715 spectropolarimeter. The spectrum was corrected for buffer contribution.

The CD spectrum of Az dissolved in PBS (pH 7.2) is shown in Fig. 2.4. According to the literature (Leckner et al., 1997), the data analysis (Alfa-helix = 36% Beta strand = 43% Random coil = 21%) confirms the wild type structure of Azurin.

2.1.2 Immunoprecipitation of p53

The conformation of p53, produced through the GST-method, was studied by immunoprecipitation technique, using two conformation-specific antibodies, as follows. GST-p53 (1 µg) was purified with thrombin cleavage (Sigma), diluted in immunoprecipitation buffer (10 mM Tris-HCl pH 7.6; 140 mM NaCl; 0.5% NP40; plus proteases and phosphatases inhibitors) and immunoprecipitated overnight at 4°C with the conformation-specific monoclonal antibodies PAb1620 (wild-type specific) or PAb240 (mutant specific) (Gannon et al., 1990; Legros et al., 1994), both from Calbiochem, preadsorbed to protein G-agarose (Pierce, IL, USA).

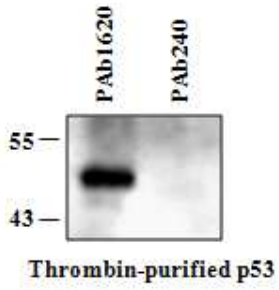

Fig.2.5. Immunoprecipitation of p53 with conformation-specific antibodies. Equal amount of thrombin purified p53 (1 µg) was immunoprecipitated with PAb1620 (for folded, wild-type conformation) and PAb240 (for unfolded, mutant-conformation) and analyzed by Western immunoblotting with FL393 polyclonal anti-p53 antibody. The representative bands of at least two independent experiments are shown.

Immunocomplexes were collected by centrifugation, separated by 10% SDS-PAGE, and blotted onto PVDF membrane. Immunoblotting was performed with rabbit polyclonal anti-p53 (FL393, Santa Cruz Biotechnology) antibody and revealed by enhanced chemiluminescence system (ECL, Amersham, IL, USA) in accordance with the manufacturer's instructions.

As expected, purified p53 was exclusively in wild-type conformation as shown by the reactivity with PAb1620 antibody (Fig. 2.5) and therefore suitable for wt-p53 activity, such as DNA binding.

2.2 SERS-based plasmonic nano-bio-sensing of p53

Gold nanoparticles (NPs) solutions, containing $4.5 \cdot 10^{10}$ particles/ml of 50 nm diameter, were purchased from Ted-Pella (Reading CA). 4-aminothiophenol (4-ATP) was purchased from Sigma-Aldrich (St. Louis, MO). Water used for these experiments was purified by MilliQ Reagent water system (Millipore, Billerica, MA).

According to the green chemistry, protocols have been conceived by using greener solvent alternatives which not only minimize solvent waste but also improve laboratory safety. The steps followed in the preparation of the functionalized gold NPs are divided into two steps (1 and 2), briefly sketched in Fig. 2.6 in accordance with paragraphs 2.2.1 and 2.2.2, respectively.

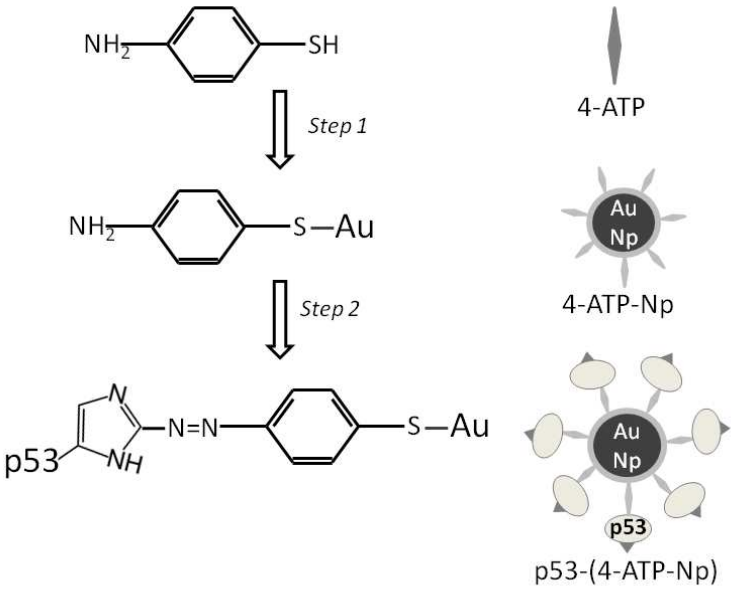

Fig. 2.6. Principal chemical reactions in the preparation of functionalized gold NPs: 4-ATP-Np and p53-(4-ATP-Np).

2.2.1 Self-assembling of gold Nps with the Raman reporter 4-ATP

Gold NPs coated with the bifunctional linker 4-ATP were prepared by the dissolution of 4-ATP in absolute ethanol (0.5 mg/ml) (Jiao et al., 2005), and mixed in a equal volume of the gold NPs mother solution. The obtained solution was incubated at 20^{o}C for 3 hours.

We have checked the quality of the samples and followed step by step the functionalization procedure by UV-Vis absorption and Raman spectroscopies (for details see Chapter 3). The UV-Vis spectra of the 4-ATP linker is shown in Fig. 2.7, panel A and B, whereas those of the gold nanoparticles alone and conjugated with 4-ATP are shown in Fig. 2.7, panel C and D.

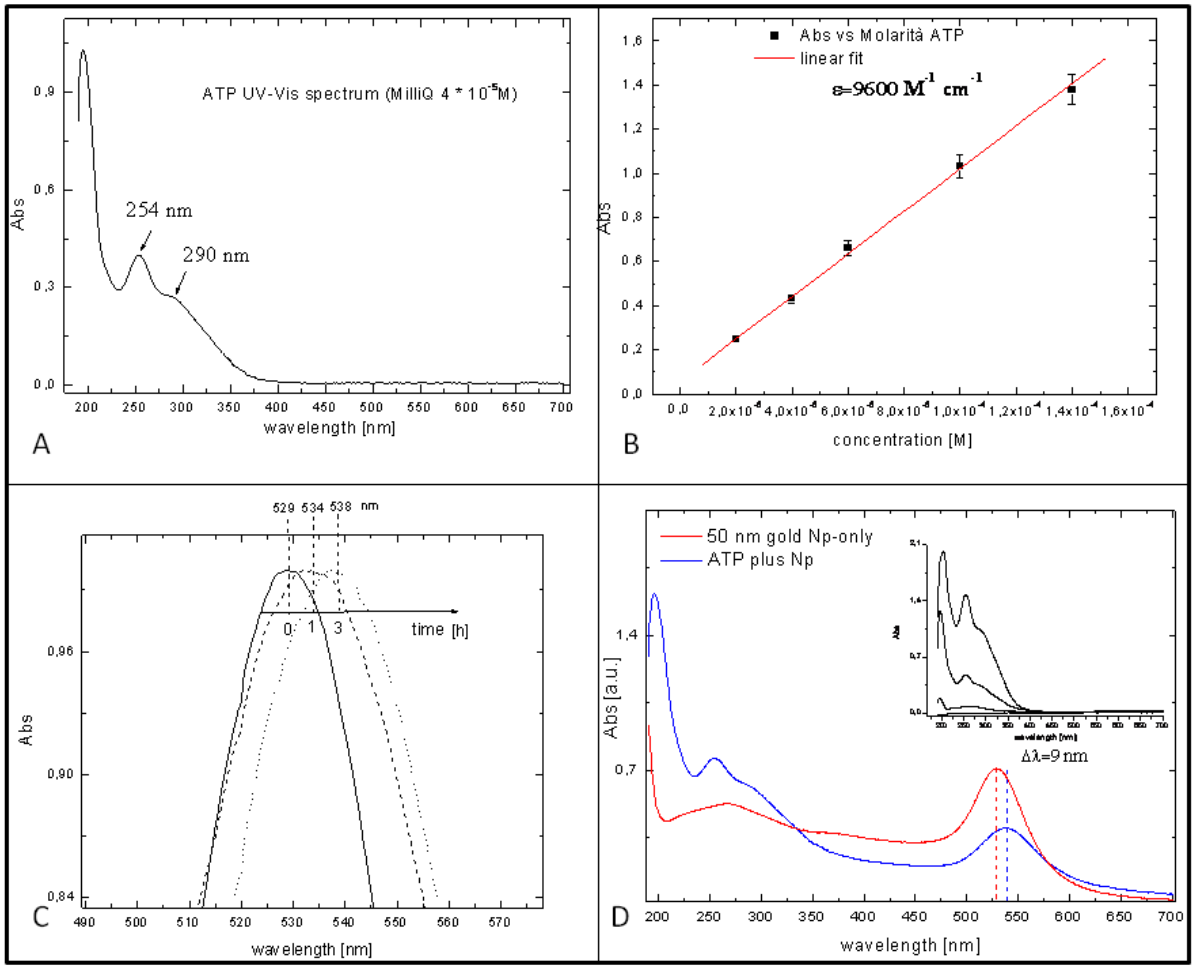

Fig. 2.7. Sample checking by UV-Vis measurements has shown: for 4-ATP the characteristic UV profile characterized by the pecks at 254 and 290 nm (panel A); while the extrapolated molar extinction coefficient of 4-ATP is reported in panel B; SPAB shift of 50 nm gold nanoparticles in function of time of 4-ATP incubation is shown in panel C; In panel D is reported the resulting UV-Vis spectrum of dialyzed water solution of 4-ATP-Np (blue profile) with respect to that of the gold nanoparticle alone (red profile); whereas in the insert of panel D shown is the absorbance decreasing of the excess of 4-ATP coming out during dialysis process.

The spectra are consistent with the previous reports on the quality and the success of the linking strategy.

The kinetic of 4-ATP-Np binding to Nps has been followed until no wavelength shift of the characteristic localized SPR absorption peak of NPs was observed (see Fig. 2.7, panel C). Moreover, in order to both remove the unbound 4-ATP and to promote the ethanol to milliQ water solvent exchange after incubation the solution was dialyzed by means of dialyzer membrane (purchased from SPECTRA/POR$^{(R)}$ irradiated dispdialyzer$^{(R)}$), with Molecular Weigh Cut Off (MWCO) of 100 kD. The presence of 4-ATP in the fluid out-coming from the membrane has been monitored, as reported in the inset of Fig. 2.7 panel D. The influence of pH on the experimental protocol has been checked and the better yield has been obtained at pH 6.0.

2.2.2 p53/4-ATP-Np conjugation

We have employed the diazo coupling chemistry for the covalent linking proteins, such as p53, onto gold nanoparticles exposing the aromatic amino compound 4-ATP.

The process is based on the reaction called *diazotization*, discovered by Peter Griess in 1858, and widely applied as a valid biomolecular immobilization strategy since 1970 (Wu et al., 2006). Diazotization consist of forming diazonium compounds, i.e phenyldiazonium cation (Ph-$N^+\equiv N$:), mainly through the treatment of aromatic amines (such as 4-ATP) with sodium nitrite in the presence of a mineral acid such as HCl, as follows:

$Ph\text{-}NH_2 + NaNO_2 + 2HCl \rightarrow Ph\text{-}N^+\equiv N: Cl^- + 2NaCl + 2H_2O$.

In aqueous solution these salts are unstable at temperatures higher than 5°C; the -$N^+\equiv N$ group tends to be lost as N_2 nitrogen gas, in favour of a carbocationic arrangement (i.e. Sandmeyer reaction). In general, the diazonium salt behaves as an electrophile, but it is a weak electrophile and so the aromatic ring which it attacks must have attached to it an activating group such as -OH or -NH_2. Therefore, according to the Pauly reaction, such a stable intermediate can induce the azo coupling with the solvent exposed hymidazolic ring of histidine and the phenol group of tyrosine residues of proteins (Phillips et al., 1965). The covalent coupling is assured by the formation of -N=N- chromophore, which provides a characteristic red azo-dye.

Although either strong or medium acidic environmental is required for the nitrosating agent formation (Ciapponi et al., 1987) the attempts performed at elevated acidity (pH 1.0) on 4-ATP-Nps have caused the complete dissolution of gold nanoparticles, whereas the diazotization of 4-ATP-Np has been successfully reached at pH 3.0 as follows.

200µl of dialyzed 4-ATP-Nps solution were converted in diazonium-Nps by slow dropping of 200 µl of $NaNO_2$ 0.1 M, previously mixed with HCl until pH 3.0 was reached. The nitrosating agent was formed maintaining the solution in an ice box for 15 minutes. Before reacting with proteins, the solution was dialyzed in d.d. ice-water to remove the excess of electrolytes (see Fig. 2.8). The diazotization of the 4-ATP-Nps was checked by adding phenol molecules and waiting for the formation of a red-dye (Ciapponi et al., 1987).

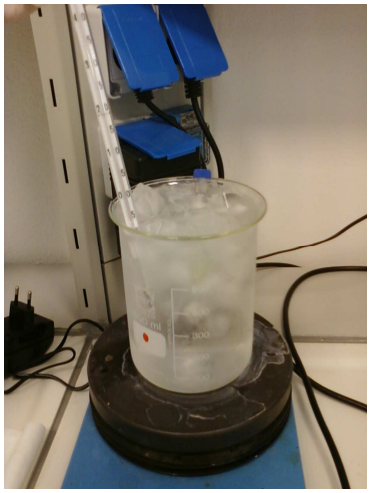

Fig. 2.8. Diazotization and dialysis of 4-ATP-Np solution occurring below 4°C

After having neutralized the diazotated 4-ATP-Nps solution, a p53 solution ranging from 10^{-9} to 10^{-13} M was added to allow diazo-coupling reaction, and kept under gentle stirring for 2 hours at 0-4°C.

As described in the previous step the product was dialyzed to remove any unbound protein, thus obtaining a solution containing only the protein-(4-ATP-Np) conjugated system in PBS buffer (pH 7.2) (see Fig. 2.6). The success of the reaction was witness by Raman and Absorbance spectroscopy (see Chapter 3).

2.2.3 Glass functionalization

The steps followed in the capture substrates preparation are briefly sketched in the left side of Fig. 2.9.

Step A: Either UV or phirana solution (30% H_2O_2/70% H_2SO_4) treatments (Crass et al., 1999; Halliwell et al., 2001) were used to clean substrates and activate their hydroxyls groups. Subsequently, activated surface were incubated for 30 minutes at 20°C with 3-Amino-Propyl-TriEthoxy-Silane (APTES) dissolved in 2-propanol (only at 8% to avoid polymerization between free silanol groups prior to their condensation onto the glass slides) to obtain uniform coatings (Park et al., 1999; Li et al., 2001; Halliwell et al., 2001). After incubation, glass surfaces were thoroughly rinsed with 2-propanol, and beaked at 110°C for 10 minutes to induce the cross-linking of free silanols (see the left side of Fig. 2.9), thus increasing both stability and activity of APTES-modified surfaces (Park et al., 1999).

Step B: Subsequently, these APTES-modified glasses were reacted with a 2% glutaraldehyde solution for 30 minutes at room temperature and washed thoroughly with MilliQ water.

Step C: Substrates were than incubated with a 10^{-5} M Az solution (PBS buffer pH 7.2), over night at 4 ^{o}C.

The same protocol was followed also to adsorb p53 and p53 mixed with Human Serum Albumin (HSA) (from Sigma–Aldrich) onto the glass slides (see Chapter 3).

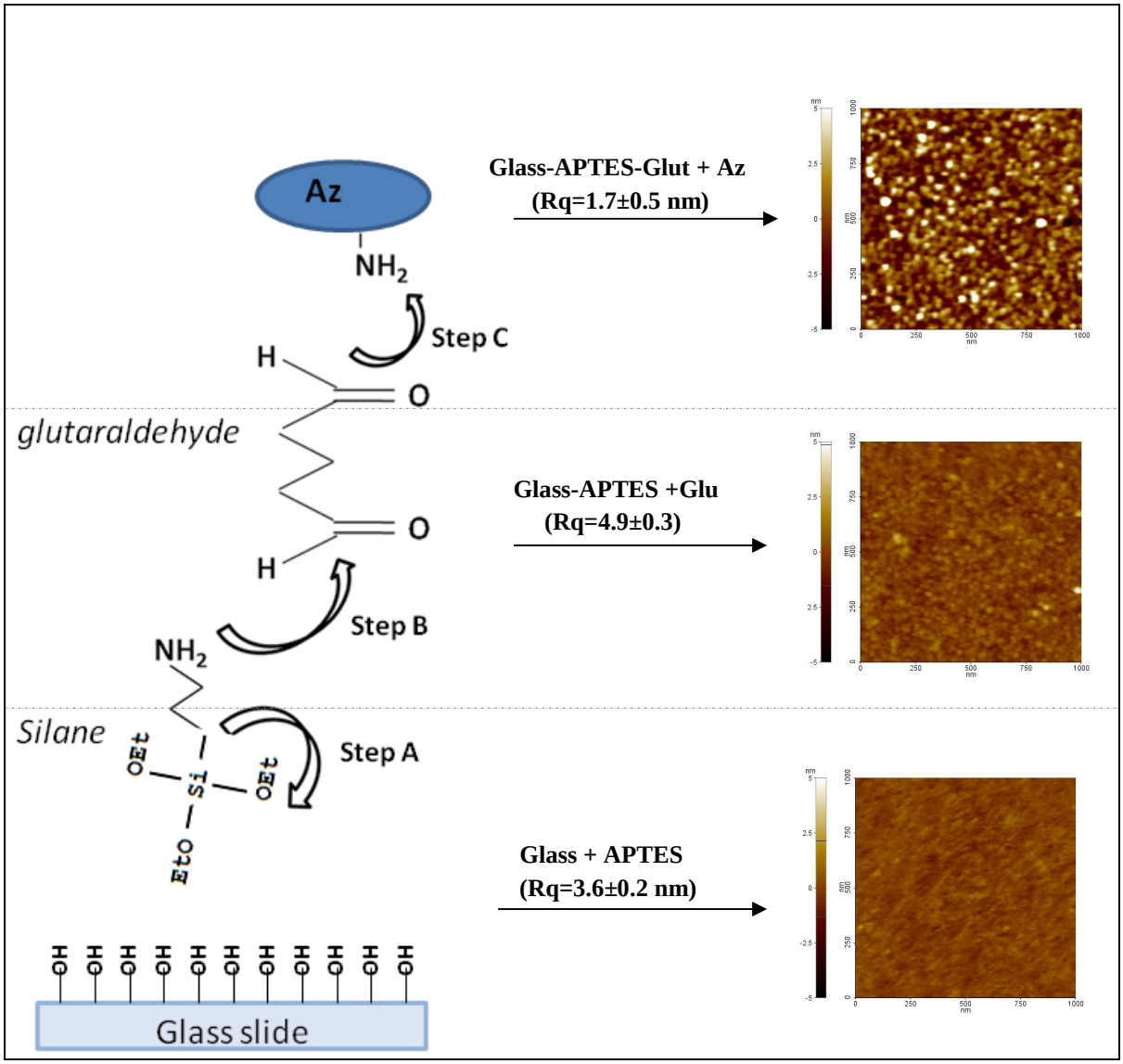

Fig. 2.9. Schematic sketch of the reaction steps of protein-modified glass substrate and the corresponding AFM analysis in fluid condition are shown in the left and in the right side of the picture respectively.

Each step of the glass functionalization was checked by AFM measurements record in tapping-mode in water (cantilever force constant, k = 0.5 N/m) (see the right side of Fig. 2.9)**.**

2.2.4 Protein sensing experiments

The protein-covered substrates were incubated for 3 hours at room temperature with the corresponding protein partner previously conjugated to (4-ATP-Np) in PBS buffer solution (pH 7.2), allowing the Az-p53 interaction. Then the substrates were washed with PBS buffer to remove the unbounded protein-(4-ATP-Np).

Tapping-mode AFM images in air (cantilever force constant, k = 0.5 N/m) were recorded by a Park XE-100 multimode scanning probe microscope by scanning several different areas of the sample. The typical scan rate was 1 Hz.

Raman and SERS spectra were recorded in air at 20^{o}C by Labram confocal setup (Jobin-Yvon) equipped with a Peltier-cooled CCD detector and a single-grating spectrograph (1800 gr/mm) allowing a resolution of 5 cm^{-1} and a 16 bit dynamic range. The microscope objectives were 100x with a numerical aperture of 0.9 producing a laser spot size of about 1µm in diameter. The source was a He-Ne laser (Melles Griot) providing a 632.8 nm radiation with a power emerging from the objective of 6.5±0.5 mW. Preliminary investigation were performed also by using a similar LabRam setup equipped with a green (514 nm) laser source. The irradiation procedure was optimized in order to maximize the signal to noise ratio of the SERS measurements (see Chapter 3).

Optical absorbance and difference absorbance spectra were recorded at room temperature by a double beam Jasco V-550 UV/visible spectrophotometer by using 1-cm path length cuvettes and 0.5 nm bandwidth. The investigated spectral range was 190–800 nm.

Detailed information concerning the instrumental equipment employed are reported in paragraph 2.4.

2.3 SPR detection of specific complexes made up of Az, p53 and Mdm2

2.3.1 p53-covered substrate preparation

The planar gold SPR sensor disks for the protein immobilization were purchased from Xantec Bioanalytics (GmbH Munster, Germany). These gold substrates were immersed in an ethanol solution of cysteamine (0.2 mM, Sigma) for 3 hours at room temperature (RT), then washed with ethanol and dried under a stream of nitrogen. The modified substrates were incubated with 250 µl of 1% glutaraldehyde (Sigma) solution in milliQ water for 10 minutes at RT, rinsed carefully with milliQ water and dried with nitrogen. Then, 250 µl of 1.2 µM p53 protein in TST buffer (pH 7.2) were dropped on the amine-reactive surface and incubated over night at 4°C. Next day the substrate was gently washed with PBS (pH 7.2) and stored in PBS buffer at 4°C. A covalent binding between the glutaraldehyde linker

and the exposed NH_2 groups of p53 leads to the protein immobilization in the required multi-oriented binding configuration, maintaining at the same time some reorientational freedom to facilitate biorecognition and avoiding denaturation due to direct contact of the protein with the gold surface (Fig. 2.10, left side).

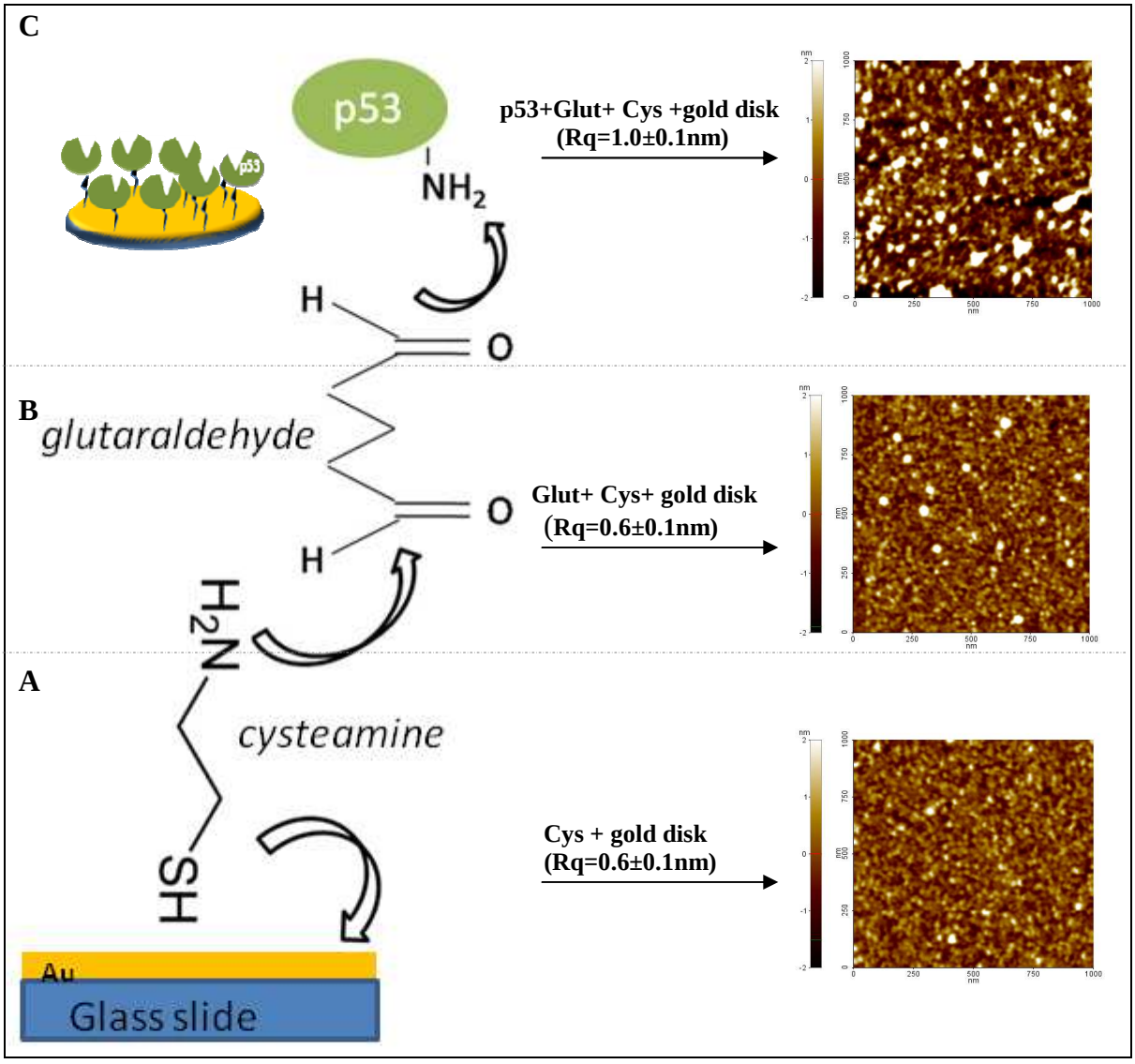

Fig. 2.10. Schematic sketch of the reaction steps of p53-modified SPR substrate and the corresponding AFM analysis are shown in the left and in the right side of the picture respectively.

Tapping-mode Atomic Force Microscopy (AFM) images in fluid (cantilever force constant k = 0.5 N/m) were recorded by means of a Park XE-100 multimode scanning probe microscope during the different steps of the sample preparation and shown in Fig. 2.10, right side.

2.3.2 SPR binding experiment

By following the time varying SPR angle shift due to binding molecular processes occurring at the sensor surface in real time, it is possible to measure the association and dissociation kinetics of the interaction.

In order to confirm the nature of the protein-protein interaction and regenerate the sensor surface after every binding cycle, we evaluated the use of regeneration solutions at different pH and ionic strength (Andersson et al., 1999). Among them, a 0.5 M NaCl solution at pH 5.0 has resulted the most effective for disassembling the Mdm2-p53 interaction, although subsequent massive loss of the p53 substrate binding capacity was observed, likely due to partial p53 denaturation (Ano Bom et al., 2010). Thus SPR binding studies were conducted by injecting the interacting protein on untreated p53 substrate portions and the homogeneity of p53 deposition was checked by AFM (see Fig. 2.10). Further control experiments and reference subtraction were performed to exclude any possible unspecific binding contribution.

Regarding the experiments on the ternary complex, 2 µM Az in PBS solution (pH 7.2) or 2 µM Mdm2 in TST solution (pH 7.2), was incubated on the overall p53-covered substrate for 3 hours at 25^{o}C, and saturation of the p53 binding site was checked on each investigated area by SPR measurements. To check that the saturation condition is maintained also during the sensorgrams acquisition, further SPR control experiments have been performed, by mixing the protein injected with that used to saturate the p53-modified sensor disk (2 µM of Az or Mdm2) (Domenici et al., 2011).

SPR sensorgrams ere pointed out using a SPR Kretschmann type spectrometer Autolab Esprit (Eco Chemie, Utrecht, The Netherlands). Further instrumental details are reported in paragraph 2.4.

2.3.3 Kinetic analysis of the SPR sensorgrams

A series of response curves collected with different protein concentrations injected over the same binding surface may be fitted simultaneously using the global analysis approach. Indeed, by fitting all data at the same time, information arising from each sensorgram are combined. As a result, global analysis provides a better test of the model and improves the statistical behaviour of the parameter estimates. Global analysis (Morton and Myszka, 1998) of the SPR sensorgrams was performed by using simultaneous nonlinear regression fit procedure derived from a reversible bimolecular interaction model (see also Chapter 1, paragraph 1.1.2):

$$A + B \underset{koff}{\overset{kon}{\rightleftharpoons}} AB$$

where A is the receptor injected in the flow chamber, B is the ligand immobilized on the surface of the SPR sensor disk and AB is the product of the specific interaction.

From this model, the following differential rate equations can be derived to determine the association (k_{on}, M^{-1} s^{-1}) and dissociation (k_{off}, s^{-1}) rate constants for protein-protein binding interaction:

association: $$\frac{d[AB]}{dt} = k_{on}[A][B] - k_{off}[AB] \quad (2.1)$$

dissociation: $$-\frac{d[AB]}{dt} = k_{off}[AB] \quad (2.2)$$

Because the reaction rates in the flow chamber may be limited by the rate of protein diffusion from bulk solution to the sensor surface, the fitting procedure also takes into account the mass-transport limit effects (k_t, M^{-1} s^{-1}) (Myszka et al., 1997):

$$A_o \overset{k_t}{\longleftrightarrow} A + B \quad (2.3)$$

Thus, the following system of differential rate equations were used to describe this reaction across the sensor surface:

$$\frac{d[A_o]}{dt} = 0 \quad (2.4)$$

$$\frac{d[A]}{dt} = k_t([A_o] - [A]) - k_{on}[A][B] + k_{off}[AB] \quad (2.5)$$

$$\frac{d[AB]}{dt} = k_{on}[A][B] - k_{off}[AB] \quad (2.6)$$

In such model, the concentration of analyte in bulk flow ($[A_o]$) is assumed to be constant during the association phase and zero during the dissociation phase. The concentration of analyte at the sensor surface ([A]) is zero at the start of the reaction. The kinetic analysis was performed by Clamp biosensor software (Morton and Myszka, 1998). Clamp combines numerical integration and non linear curve-fitting routines. It is designed to interpret complex interactions recorded on biosensors by simultaneously analyzing association and dissociation phase data measured on different surfaces or in different experiments. The flow chart in Fig. 2.11 demonstrates how the program works. To begin

an analysis, the user inputs data, loads a reaction model, and enters reasonable starting values for the unknown parameters. The program will automatically generate a series of differential rate equations based on the model and will integrate them numerically to simulate a set of response curves using a semi-implicit extrapolation method. This method is capable of handling stiff sets of differential rate equations. These occur when two reactions take place with very different rates and, when not treated properly, may cause instability in the integration. After simulated data are generated, they are subtracted from experimental data in order to calculate the χ^2. The initial estimates for the rate constants are then adjusted to minimize the χ^2 using a Levenburg-Marquardt nonlinear minimization algorithm. If the new estimates do not reduce the χ^2, they are discarded, the fit progress is decreased, and another set of parameter estimates is chosen. Estimates that decrease the χ^2 are kept and the fit progress is increased. The simulation and minimization process is repeated until the change in the χ^2 is less than 0.1%. The parameter values, along with their linear approximation standard deviations and correlation coefficients, are output in a results table.

Thus, the quality of the fits shown in Chapter 4 was judged by the residuals and the normalized chi square (χ^2) of the fitting model. In addition, the validity of the obtained rate constants was assessed by simulating data with identical ratio values of the rate constants and varying k_{off} and k_{on} values.

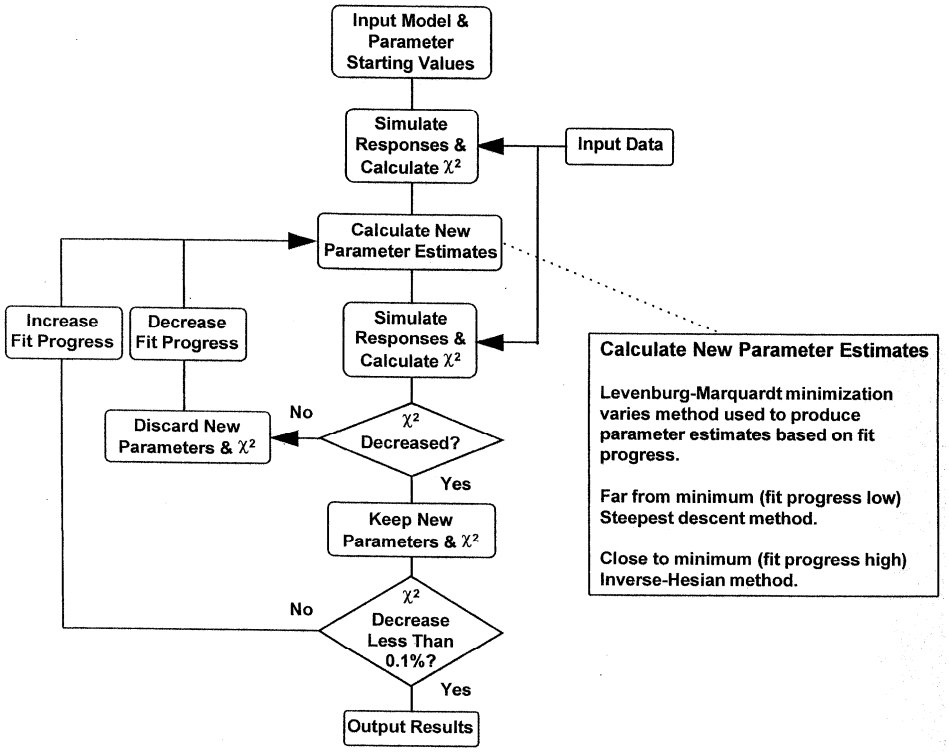

Fig. 2.11. Flow chart outlining the computational procedures used in Clamp.

As shown in chapter 1, paragraph 1.1.2, the equilibrium dissociation constant (K_d, M), can be derived from the ratio of the measured kinetic parameters: (k_{off}/k_{on}).

2.3.4 CD measurements of Az-p53

CD measurements were performed on bare p53, and on p53 previously incubated with Az at 1:1 molar ratio (this corresponds to a 4:1 molar ratio when we consider that p53 is a tetrameric molecule) for 3 hours at 25°C using a JASCO J-715 spectropolarimeter, equipped with a 0.1 cm path length and thermally controlled quartz cell. CD spectra were recorded at 25°C in TST buffer at pH of 7.2 (50 mM Tris buffer with 150 mM NaCl and 0.1% Triton x 100) and at 0.50 μM proteins concentration obtained by quantitative dilution of the mother solution to prevent spectral contribution from protein aggregation.

All spectra were the average of ten repeats obtained by collecting data from 250 nm to 190 nm at 0.5 nm intervals, at a rate of 50 nm/min with a response time of 2 s for each point.

The experimental patterns acquired in millidegrees of ellipticity θ were corrected by solvent subtraction and converted to mean residue ellipticity $[\theta]_{MRW}$. The predicted content of secondary structure was calculated using the CD spectra deconvolution software CDSSTR (Whitmore and Wallance, 2004) with a normalized root mean square deviation value of 0.01.

2.4 Instrumental description

2.4.1 MicroRaman spectroscope

It is well known that Raman spectroscopy is used to identify different molecules and even functional groups within larger molecules. The bonds formed between atoms have specific vibrational frequencies that correspond to the atom masses and the strength of the bond between them. Complex molecules therefore exhibit many peaks and can be readily identified by the pattern or "fingerprint" created by those peaks (see also paragraph A.2.1). As such, there are many uses for micro-Raman spectrometers, including SERS investigation, as they can non-destructively identify microscopic samples or microscopic areas of larger samples.

Raman and SERS spectra were recorded by Labram confocal setup (Jobin-Yvon, Longjumeau, Cedex, France) equipped with a charge-coupled device Peltier-cooled detector and a single grating spectrograph with an 1800-g/mm grating allowing a resolution of 5 cm-1. The most powerful lens of the microscope was a 100x objective with a numerical aperture of 0.9, producing a laser spot size of about 1 μm in diameter. The

source was a HeNe ion laser (MellesGriot, Carlsbad, CA) providing a 632.8-nm radiation, with power of about 6 mW. The internal He-Ne laser is polarized vertically.

The laser beam is directed by two mirrors through the interferential filter 633 (an interferential pass-band filter is used to filter out the plasma lines of the laser).

The laser beam is focused on a system called LIRS (Laser Injection rejection system) composed of a mirror and the holographic notch filter. This system allows the change of the notch angle by means of a spacer. So with an appropriate angle, the beam is completely reflected toward the sample. Thus, a lens produces a parallel beam that is focused on the sample by the infinite optics microscope objective.

The Raman signal collected by the microscope objective in back scattering configuration follows the same way back. The reflection on the sample of the laser line (Rayleigh) is reflected again by the notch filter while the Raman beam passes through the notch. A further lens provides the image of the Raman beam onto the confocal hole, see the fig. 2.12 for a representative microRaman sketch.

Before the confocal hole, there is a place where you can put some polarizer filters or a second notch for working in lower frequencies (50 cm^{-1}).

The magnification between the sample and the confocal hole depends on the microscope objective magnification, multiplied by a factor 1.4. For example, if you use a 100x objective, the size of the image is multiplied by 1.4*100. The factor 1.4 arises because the tube length for Olympus objectives is 180 mm while the lens that form the image has a focal length slightly higher of 250 mm. So the magnification is 250/180 = 1.4. The subsequent lenses project the beam from the confocal hole onto an adjustable spectrograph entrance slit which adapts the aperture of the beam to the spectrometer's one. The image of the hole is reduced by a factor of 5. In the optical beam coming from the microscope, two beam splitters 50/50 is introduced for sample observation on the TV camera. The first one takes the light of the fiber optic illuminator and send it on the sample. The second one sends an image of the sample to a TV camera.

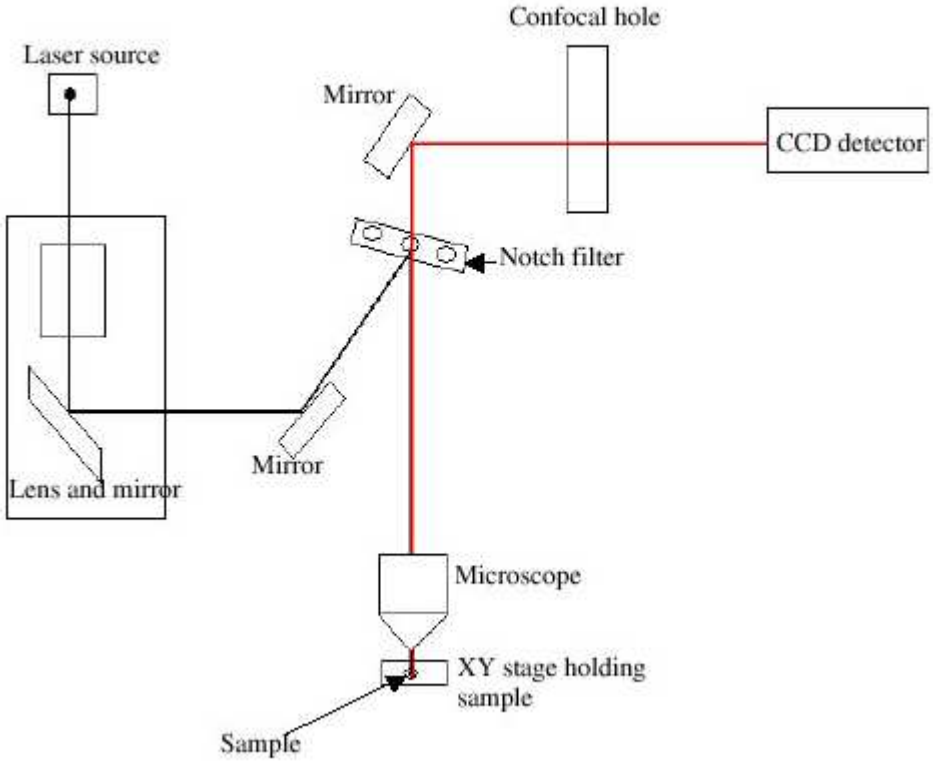

Fig. 2.12. Schematic sketch of micro-Raman equipment (LAbRam)

2.4.2 UV-Vis spectroscope

Optical absorbance and difference absorbance spectra were recorded at room temperature by a double beam Jasco V-550 UV/visible spectrophotometer by using 1-cm path length cuvettes and 0.5 nm bandwidth. The investigated spectral range was 190–800 nm.

The light source consists in a discharge tube of deuterium in the UV region (190-350 nm) and a tungsten iodine lamp in the region between 330-800 nm. The detector consists of a photomultiplier tube. The working scheme is shown in Fig. 2.13.

The light from the source is directed into a monochromator and subsequently towards on ad-hoc mirror. Here is appropriately divided into two beams, one incident on the sample where optical properties shall be derived, the other one on the sample reference, which represents the end of the spectrum measured, and which must therefore be eliminated from the spectrum to be processed. The light, after passed through the sample to be measured or reference, affects the detector and thus converted into an electrical signal and digitized by a data processing software.

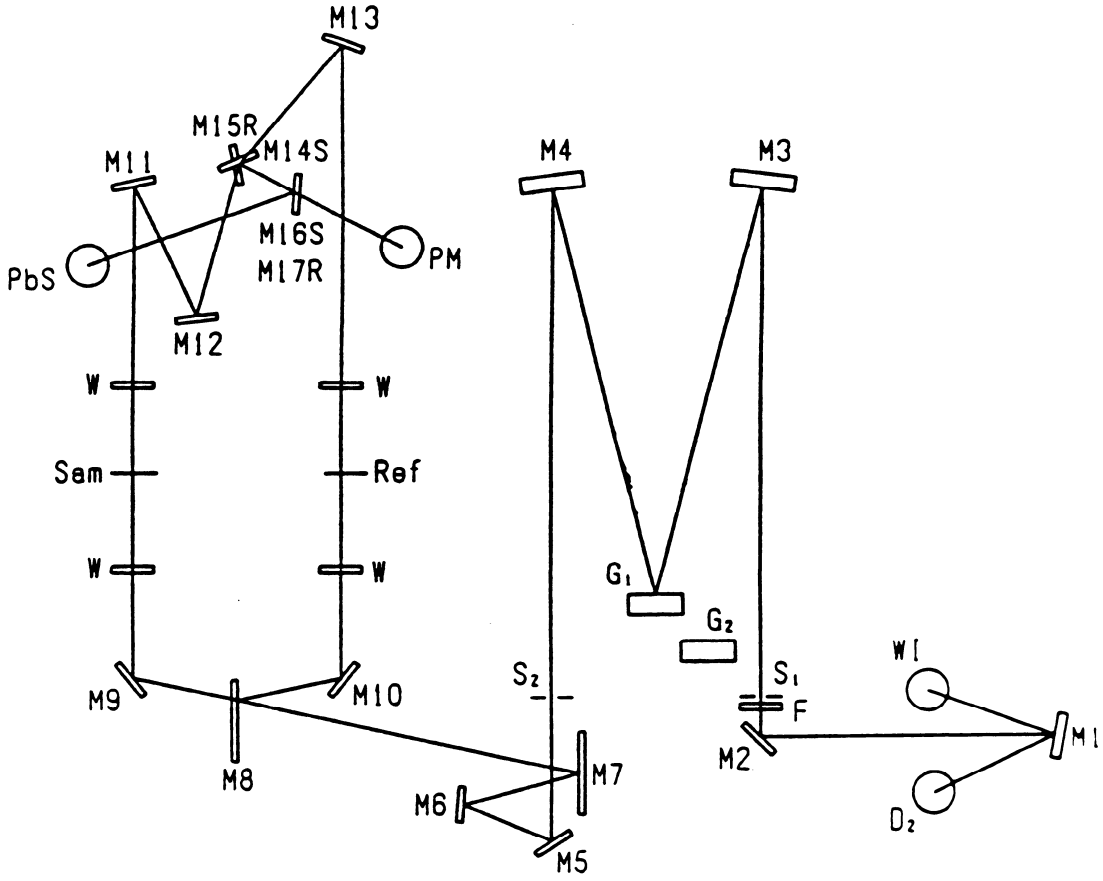

Fig. 2.13. Schematic sketch of UV-Vis Setup. D_2 and WI (light sources); S (slits); G (monochromator); PM (detector); PbS (optional detector for near infrared region); Sam (sample); Ref (reference signal); M (mirror); F (filter); M14S and M16S (beam splitters).

2.4.3 AFM apparatus

Atomic Force Microscopy (AFM) images were record using a Park XE-100 multimode scanning probe microscope (see also Appendix B).

AFM uses a micro-machined cantilever with a sharp tip to measure a sample surface. Depending on the distance between the atoms at the tip of the cantilever and those at the sample surface, there exists either an attractive or repulsive force/interaction that may be utilized to measure the sample surface. Fig. 2.14 displays the basic configuration for the most common AFM. This scanning AFM is typically used to measure a wide variety of samples, which have relatively small roughness. The force between atoms at the sample surface and those at the cantilever tip can be detected by how much the cantilever deflects. This deflection of the cantilever can be quantified by the measurement of a laser beam that is reflected off the backside of the cantilever and onto the Position Sensitive Photo Detector (PSPD).

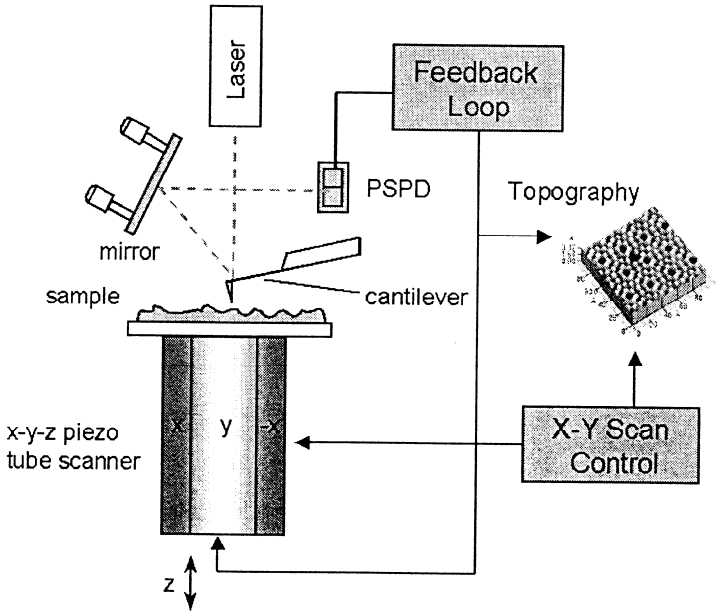

Fig. 2.14. Schematic sketch of AFM setup.

The tube-shaped scanner located under the sample move a sample in the horizontal direction (X-Y) an in the vertical direction (Z). It repetitively scans the sample line by line, while the PSPD signal used to establish a feedback loop which controls the vertical movement of the scanner as the cantilever moves across the sample surface.

An optical microscope (with 10x and 20x objective lens) is used to focus the laser beam onto the cantilever and to locate the cantilever to interesting region on the sample surface that is to be measured. Since the optical microscope is located parallel to the Z-scanner, it is possible to have a direct on-axis view of the cantilever in conjunction with the sample area that is to be scanned.

2.4.4 SPR apparatus

SPR measurements were performed by means of a SPR Kretschmann type spectrometer Autolab Esprit (Eco Chemie, Utrecht, The Netherlands), equipped with a LED light source emitting at 670 nm and a prism with 1.52 refraction index was used to measure the intensity of the reflected light at the corresponding resonance angle. This angle can be measured over a range of 4^o after focusing by a lens into a photodiode detector. The incident angle was varied by using a vibrating mirror (rotating over an angle of 5^o at 77 Hz) with a resolution of 1 millidegree. The glass supported SPR substrates were clamped against a Teflon cuvette with O-rings, providing liquid-tight seals. An autosampler (Eco Chemie) with controllable aspirating–dispensing–mixing pipette was used to add samples

into the cuvette and provide constant mixture by aspiration and dispensing during measurements. This experimental arrangement assures a homogeneous solution and reproducible hydrodynamic conditions. The temperature of the cuvette was kept at 25±1°C. A schematic sketch of SPR equipment is shown in Fig. 2.15.

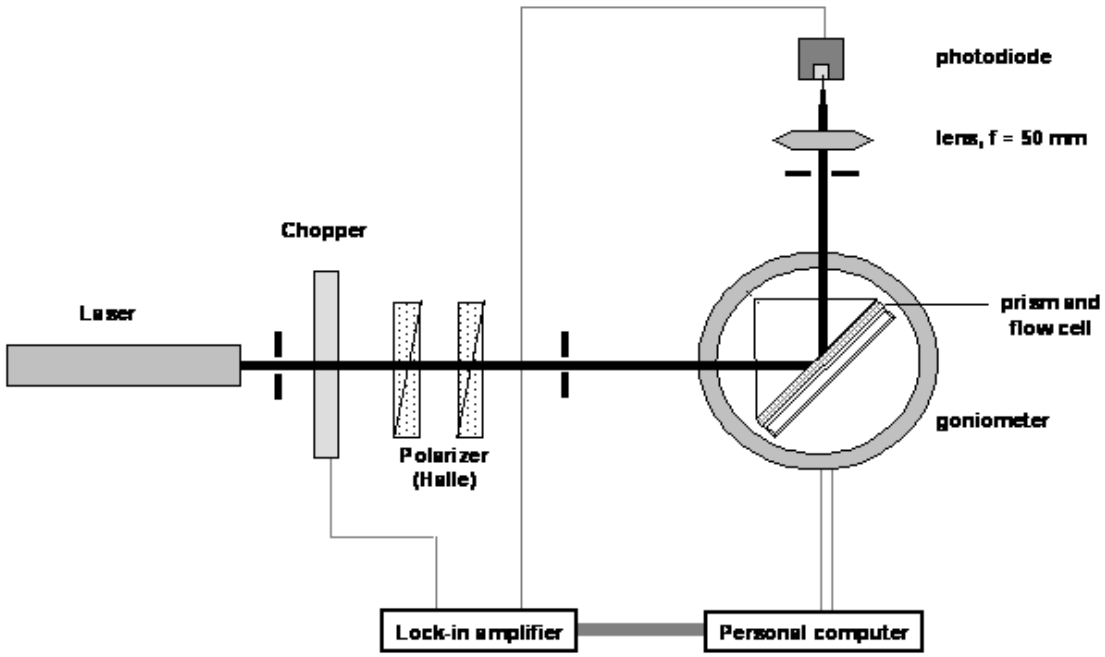

Fig. 2.15. Schematic sketch of SPR equipment.

2.4.5 CD spectroscope

The phenomenon of circular dichroism is very sensitive to the secondary structure of polypeptides and proteins. Circular dichroism (CD) spectroscopy is a form of light absorption spectroscopy that measures the difference in absorbance of right- and left-circularly polarized light (rather than the commonly used absorbance of isotropic light) by a substance. It has been shown that CD spectra between 260 and approximately 180 nm can be analyzed for the different secondary structural types: alpha helix, parallel and antiparallel beta sheet, turn, and other. A number of excellent review articles are available describing the technique and its application (Sreerama and woody, 1994).

The optical system diagram of the CD spectropolarimeter is shown in Fig. 2.16.

As light source a xenon lamp is used. The light emitted from the lamp is then made to converge by the mirror M1 towards the slit S1. The optical system between the entrance S1 and intermediate S2 slits refers to the first monochromator, while the optical system that is located between the S2 and exit S3 slits, refers to the second monochromator. Each optical system, between two monochromators, is known as a double monochromator. The ability

of a double monochromator to reduce the stray light is essential to make measurements of circular dichroism. This device uses glass prisms (P1 and P2) with different axial orientations, so that the light passing through the monochromator is not only monochromatized but also linearly polarized, and oscillates in the horizontal direction. The linearly polarized light is then modulated into two beams of circularly polarized light to the right and left. The effect of modulation on the light is produced by the modulator, (which is able to induce a *piezo* effect on a quartz crystal).

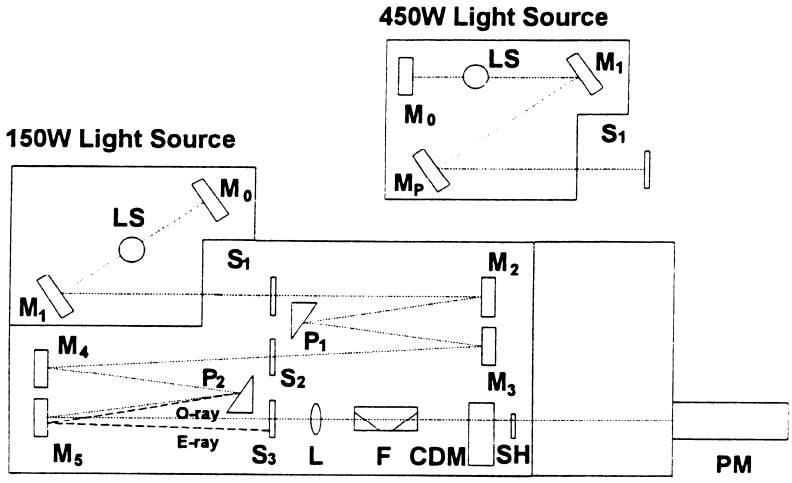

Fig. 2.16. Schematic sketch of circular dichroism optical setup.

Chapter 3

SERS-based nano-bio-sensing for ultrasensitive detection of the tumour suppressor p53

3.1 Introduction

Tumour markers play an important role in cancer diagnosis and many efforts are currently devoted to the development of ultrasensitive and rapid analytical approaches to identify them (Soper et al., 2006; Stefanek et al., 2009).

As already reported in paragraph 1.2 the human tumour suppressor p53 is considered an indicator of special interest since its tissue and/or serum level has been associated to the tumour invasiveness and prognosis on patients with various malignant diseases (Shurbaji et al., 1995; Zusman et al., 1996; Shimada et al., 2000; Malviya et al., 2004; Psyrri et al., 2007). For this reason several different p53 detection procedures have been developed (Thomas et al., 1997; Levesque et al., 1998; Benini et al., 1998; Portefaix et al., 2002; Guihong et al., 2004; Chung et al., 2005; Cloarec et al., 2008; Chen et al., 2009; Yeo et al., 2009). Undoubtedly, among these procedures, the most common ones are the traditional fluorescence-labelled immunological methods such as the Enzyme-Linked Immuno-Sorbent Assay (ELISA) (Thomas et al., 1997; Benini et al., 1998; Levesque et al., 1998; Portefaix et al., 2002). However, these methods require multiple steps, long incubation periods and provide only a semi-quantitative analysis (Guihong et al., 2004). Beside such more traditional methods, novel label-free detection techniques have paved the way for the realization of protein chip-based immunoassays with enhanced sensitivity and specificity (Chung et al., 2005; Cloarec et al., 2008; Chen et al., 2009; Yeo et al., 2009).

In the last few years, nanoparticle research has received much attention in clinical diagnosis (El-Sayed et al., 2005; Chen et al., 2009; Boisselier and Astruc, 2009). Gold nanocolloids have been widely used to design immunoassay tests for tumour markers, based on their peculiar properties such as a high surface-to-volume ratio, the possibility of suitable biomolecular conjugation, the rewarding chemical stability, and the collective electronic behaviour at their surface. In particular, the huge optical and electrochemical signal enhancement, combined to the formation of metal nanoparticle-biomolecule assemblies (Soper et al., 2006; Chen et al., 2009), provides the basis for ultrasensitive and molecular specific detection.

Within this context, the use of Surface-Enhanced Raman Scattering (SERS) methodology (Kneipp et al., 1997; Nie and Emory, 1997; Campion and Kambhampati, 1998; Wei et al., 2001) offers great promise for simplified detection of biomolecular interactions and several advantages in early diagnostic over the previously mentioned assay methodologies (Bizzarri and Cannistraro, 2007a; Bizzarri and Cannistraro, 2009; Wang et al., 2010). SERS is based on the huge enhancement of the Raman cross section of molecules when they are placed in the proximity of a nanostructured metal surface (Jackson and Halas, 2004) as due to the contribution of an electromagnetic (EM) and chemical effect. Depending on both the chemical nature of the adsorbed molecules and the metal surface features, SERS may reach a 10^{10} fold increase of conventional Raman detection sensitivity (for theoretical details see also paragraph A.2).

As reported in paragraph A.2.2, previous works have demonstrated the remarkable potential of this approach in the detection of single molecules and in nano-bio-diagnostic (Bizzarri and Cannistraro, 2005; Bizzarri and Cannistraro, 2007a; Bizzarri and Cannistraro, 2007b; Bizzarri and Cannistraro, 2009).

Proceeding from these studies, here we report a novel SERS-based detection method, arising from the synergic combination of SERS methodology and bioaffinity assays, by which it has been possible to considerably lower the current threshold sensitivity in the detection of p53. In particular, we have exploited the specific interaction of p53 with the bacterial blue-copper protein Az. Indeed, cellular (Yamada et al., 2002; Yamada et al., 2004) and molecular studies (Punj et al., 2003; De Grandis et al., 2007; Taranta et al., 2008a; Domenici et al., 2011) have demonstrated that Az is an exogenous vector able to preferentially enter cancer cells and form a specific and stable complex with the human p53, increasing its tumour suppressor activity. It is believed that their interaction involves a portion of the hydrophobic patch surrounding the copper atom of Az, and the DNA Binding Domain of p53 (Yamada et al., 2002; De Grandis et al., 2007), in which the majority of p53 tumour-derived mutations reside. In our laboratory, the binding and kinetic features of the Az-p53 complex have been recently investigated by single molecule Atomic Force Spectroscopy and by Surface Plasmon Resonance (SPR) (Taranta et al., 2008a; Domenici et al., 2011). These studies also reported in Chapter 4 have demonstrated that this complex is significantly stable and not affected neither by the immobilization strategies used nor by the binding to p53 of the Mdm2 protein, with the latter playing a key role in lowering the intracellular stability of p53 (Domenici et al., 2011).

The choice of Az as a biorecognition partner for the detection of p53 provides some advantages connected with its stable structure within a wide range of physico-chemical conditions (Adman, 1991), and its peculiar resonance Raman bands (Bizzarri et al., 2008), which constitute a suitable optical fingerprint to disclose its presence in the detection process.

In this work we have used the 4-ATP linker, having on one side a thiol group able to bind to a gold Np, and on the other side a diazonium moiety capable of reacting with the electron-rich aromatic lateral chains of p53. p53 conjugated to a gold Np has been transferred on a capture substrate composed of an Az monolayer, and the strong intense SERS bands, characteristic of the p53-(4-ATP-Np) system, have been followed to identify the p53 molecules recognized by the Az partner molecules.

3.2 Experimental setup optimization

One of the major points in the application of SERS microspectroscopy for analytes detection, is the preparation of metallic surfaces or media, called 'SERS-active substrates' that have an easily controlled protrusion size and reproducible structures on the sub-µm scale.

We have explored commercial pattern surface of Klarite SERS substrates (Mesophotonic Ltd.) (Szeghalmi et al., 2007) (see fig. 3.1) and home-made nanostructures.

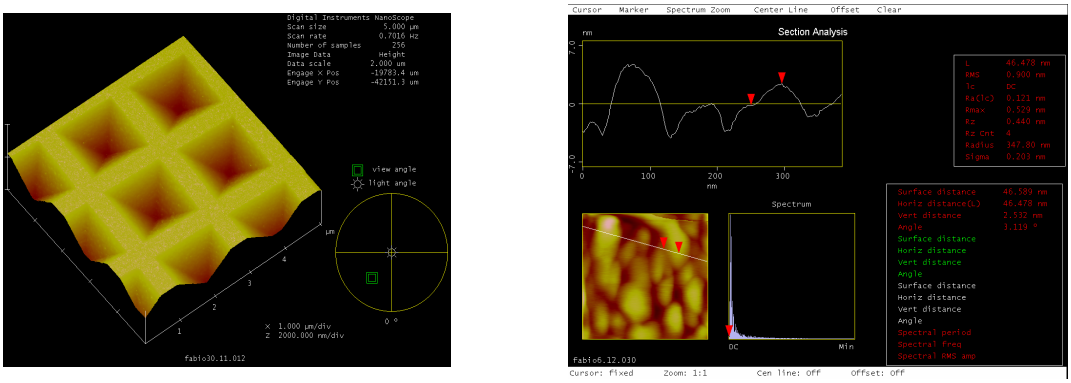

Fig. 3.1. AFM imaging of both the pyramidal with squared base shape (left side) and a detail of the rough gold coating (right side) of the Klarite SERS substrate is shown.
The measurements were performed in air environment with a Nanoscope IIIa/ Multimode atomic force microscopy (AFM; Digital instruments, Santa Barbara, CA), in contact mode, with a cantilever force constant, k, of 0.5 N/m; scan rate of 1Hz.

In particular, 50 nm gold nanoparticles have resulted to better satisfy experimental requirements in term of the reproducibility, optical enhancement and selectivity.

Moreover we have optimized the sample irradiation method in order to both increase the signal to noise ratio for integration time unit, and reduce the molecular bleaching phenomenon which causes a gradual decrease in the intensity of the Raman signal due to the molecular destruction (see Fig. 3.2). Thanks to this acquisition mode, we have gained an additional increase of the Raman signal to noise ratio of about two orders of magnitude.

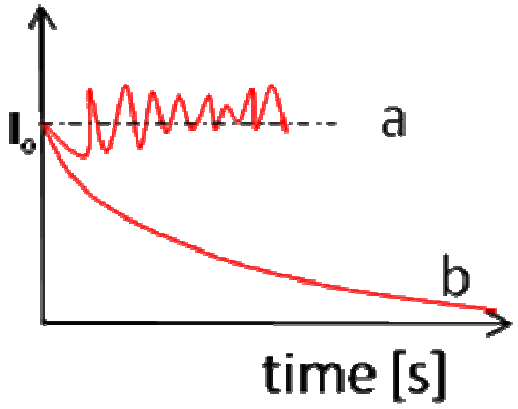

Fig. 3.2. SERS intensities profile representative of a sample irradiation by scanning registered different sample areas (under moving the sample holder) (a) or alternatively registered on a fixed sample area (b) for time unit were shown.

Another peculiar point of this optical approach is the use of SERS labels, characterized by strong Raman bands, which are suitable to identify analytes at very low concentration. Therefore, a reproducible labelling protocol has been optimized to obtain a SERS marker of biological and organic agents (for protocol details see also Chapter 2).

3.3 Results and discussion

The approach developed for SERS detection of p53 at very low concentration is explained in paragraph 2.2. The 4-ATP molecules are linked to gold Nps by means of a covalent S-Au bond, and the resulting 4-ATP-Np system is successively conjugated to p53 molecules via a diazo-coupling reaction to form p53-(4-ATP-Np). Glass slides are instead treated in sequence with silane and glutaraldehyde and then reacted with Az to form the capture substrate. The p53-(4-ATP-Np) system is then incubated with the Az platform to allow p53 recognition.

3.3.1 Optical characterization of the p53-(4-ATP-Np) system

Each step of the assembling of the p53-(4-ATP-Np) system has been investigated by Raman spectroscopy and the resulting spectra are shown in Fig. 3.3. The bands found in the selected wavenumber region, where the main spectral changes occur, are reported in Tab. 3.1, together with the literature-based assignments (Zhu et al., 2004; Osawa et al., 2004; Jiao et al., 2005; Baia et al., 2006).

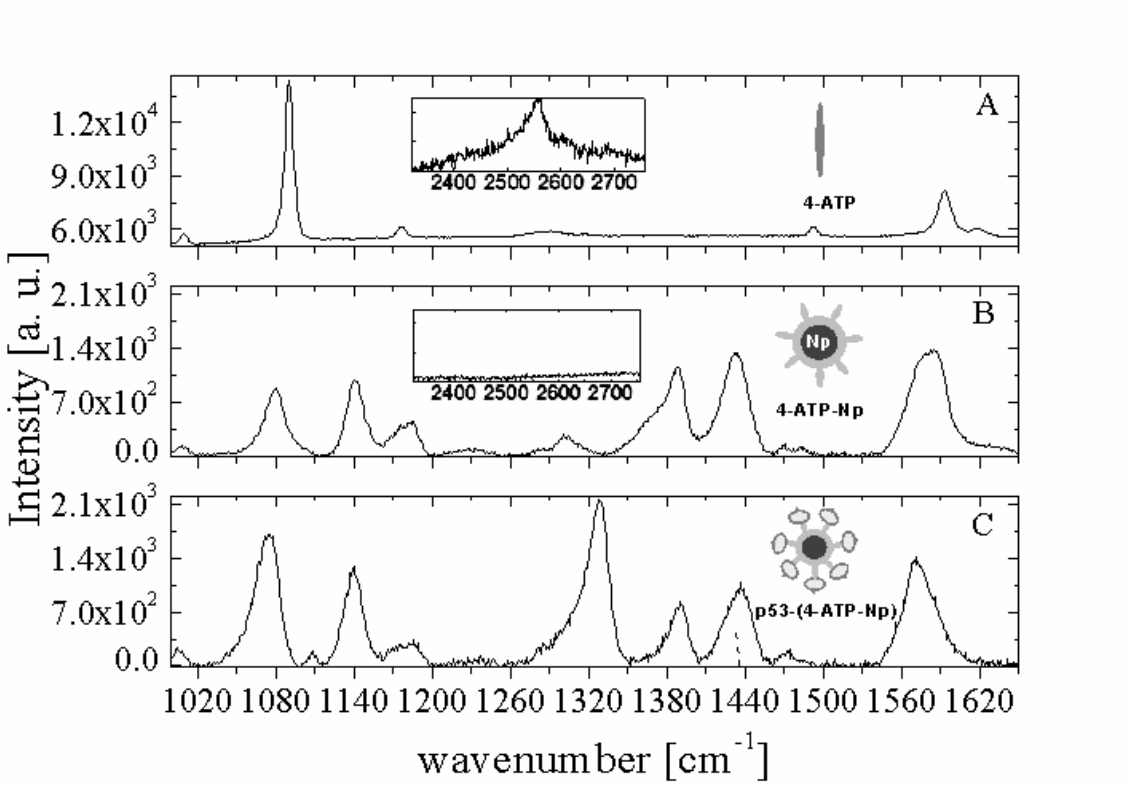

Fig. 3.3. Raman spectrum of solid 4-ATP (A); SERS spectra of solid 4-ATP self-assembled on 50 nm gold Nps (B) and solid p53 (about 1 ng) assembled by diazotization over 4-ATP-functionalized gold nanoparticles (C). The spectral range corresponding to the S-H stretching mode is shown in the inserts.
The measurements were performed by a 633 nm laser line, Obj 100x and 50x (no smoothed spectra).

Vibrational Assignment	**4-ATP Raman** [cm^{-1}]	**4-ATP-Np SERS** [cm^{-1}]	**p53-(4-ATP-Np) SERS** [cm^{-1}]
SC str + NH_2 rock	1089s*	1079s	1076s
CH bend	1176w*	1141m*	1140w
CN bend	1211vw*	1190w	1182w
NN str			1328s
CC str+CH rock+NH_2 rock		1388m	1390m
CC str+NH_2 rock		1433m	1436m
CC str+CH bend	1492w	1470;1483w	1470;1483w
CC str+NH_2 bend	1593s	1580s	1572s
SH str	2555w		

*Intensitity: s (strong); m (medium); w (weak); vw (very weak);

Tab. 3.1. Selected Raman and SERS bands of 4-ATP, 4-ATP-Np and p53-4-ATP-Np with their vibrational assignments.

We can note striking differences between the spectra of 4-ATP linker before (Fig. 3.3 A) and after (Fig. 3.3 B) conjugation with gold Nps. As shown in the inserts of Fig. 3.3 A and B, the disappearance of the band centred at 2550 cm^{-1}, inherent in the SH stretching vibration of 4-ATP, reflects the formation of a covalent S-Au bond between 4-ATP and Np. Moreover, most of the peaks in the 1000-1700 cm^{-1} region of 4-ATP show an appreciable red-shift in frequency and a strong increasing in intensity when the molecule is bound to the Nps. The apparent enhancement of the bands around 1141, 1390 and 1435 cm^{-1} in Fig. 3.3 B, which are closely related to the thiol group vibrations, has been ascribed to the charge transfer of the metal to the adsorbed molecules (Baia et al., 2006). It is worth noting that such a process is one of the mechanisms responsible for the enhancement of the Raman cross section (SERS effect) (Osawa et al., 2004; Zhu et al., 2004; Jiao et al., 2005; Baia et al., 2006), for molecules bond to a metal surface. The other bands reported in Tab. 3.1 for 4-ATP-Np are thought to be selectively enhanced by SERS effect mainly via EM mechanisms. In particular, given the high signal to noise ratio of the C-S stretching mode (around 1089 cm^{-1} and 1078 cm^{-1} for solid 4-ATP and 4-ATP-Np system, respectively), we have used the corresponding bands intensity on unit mass to estimate the EM enhancement contribution in SERS effect which resulted to be of seven orders of magnitude.

After the diazotization reaction, which involves the conjugation of p53 through its exposed histidine and/or tyrosine residues, the SERS spectrum of the whole p53-(4-ATP-Np) system displays an additional band centred at around 1328 cm^{-1} (Fig. 3.3 C). The new band is assigned to the stretching vibration modes of the diazo bond (-N=N-) which tightly keeps linked the protein to the 4-ATP-Np system (Jiao et al., 2005; Wu et al., 2006; Andrikopoulos et al., 2006). The intensity of this band increases with the p53 concentration used for the diazotization reaction (not shown), indicating that each 4-ATP-Np is able to conjugate a higher number of p53 molecules when their concentration is increased. Indeed, we have estimated that up to about 250 p53 molecules can be effectively bound on a single 50 nm 4-ATP-Np (Bizzarri and Cannistraro, 2007a).

It emerges that the SERS bands characteristic of the 4-ATP-Np system, together with the band around 1328 cm^{-1}, appearing with the covalent conjugation of p53 to 4-ATP-Np, represent the spectroscopic fingerprint of our p53-(4-ATP-Np) system, and consequently they constitute the Raman marker we have followed for the detection of p53 when it is captured by its recognition element.

It is worth noting that by considering these characteristic SERS peaks associated to the presence of the solid p53-(4-ATP-Np) system, we have estimated a minimum detectable

p53 mass of about 1 picogram which is consistent with the mass sensitivity of modern SPR-based bio-sensing tools.

The stepwise molecular assembly of p53-(4-ATP-Np) has been investigated also by an UV-Vis spectrometer, by monitoring the resonant absorption bands due to the collective oscillations of conductive electrons of gold Nps, called Localized Surface Plasmons (LSP). Fig. 3.4 shows that the bare Nps are characterized by an absorption band centred around 530 nm (solid profile). After binding of 4-ATP to Nps, we have observed a significant shift of the plasmonic resonance band from 530 nm up to a maximum of 541 nm (Fig. 3.4, dotted profile). Since the intensity of the red-shift is closely related to the number of molecules adsorbed on gold Nps (Nie and Emory, 1997; Campion and Kambhampati, 1998; Sarah et al., 1999; Wei et al., 2001), we can reasonably assume that at the maximum shift the Nps surface is fully covered by 4-ATP.

Upon p53 assembling, we have noticed a further wavelength shift from 541 up to a maximum of 555 nm (Fig. 3.4, dashed profile) that, for the same reason, probably represents the moment in which p53 molecules fully cover each 4-ATP-Np. Interestingly, in this latter case the absorption peak is also characterized by a shoulder (Fig. 3.4, dashed profile). The Gaussian analysis reveals that this asymmetry may represent the contribution of a further plasmonic band centred at 630 nm (Fig. 3.4, full circles).

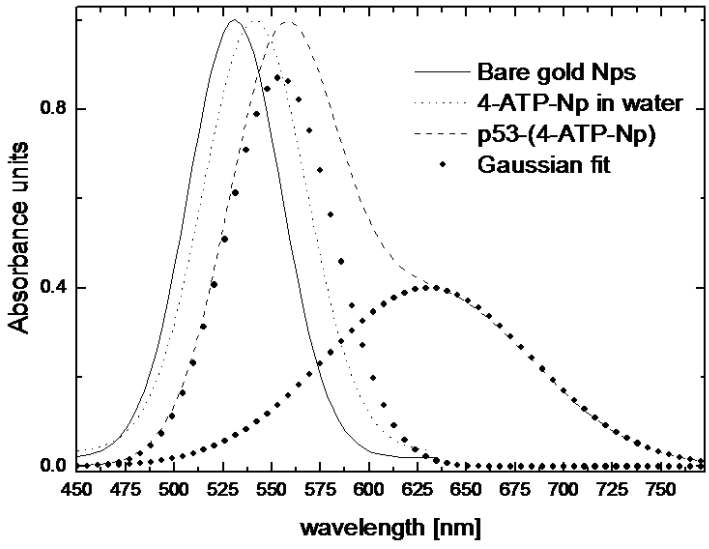

Fig. 3.4. LSPR absorption peaks centred around 530±0.5 nm, 541±0.5 nm and 558±0.5 nm for bare 50 nm gold Nps, ATP-Np, and p53-ATP-Np dissolved in MilliQ water. In particular, the LSPR absorption profile registered for p53-(4ATP-Np) is characterized by two sub-components centred at 555±0.5 nm and 630±0.5 nm (full circles).

In the literature, plasmonic modes centred around 630 nm are often ascribed to additional interparticle coupling effects (Zhu et al., 2004). We can hypothesize that, during the diazo-copuling reaction, p53 molecules form multiple bonds with different azotated 4-ATP-Nps, thus promoting interparticles modulation of the common localized plasmonic bands. Notably, by using this SPR absorption bands we have detected the p53 protein tightly bound to Nps via the bifunctional 4-ATP linker at 10^{-9} M, which is about three orders of magnitude below the value of the absorbance sensitivity of traditional UV-Vis spectroscopy.

Moreover, we may infer that the existence of a broad and asymmetric absorption peak in the visible spectral range (Fig. 3.4, dashed profile) ensures that a resonant Raman contribution is involved in the overall SERS enhancement of the p53-(4-ATP-Np) system, when a green and red laser excitation are employed.

However, by using a green laser (centred at 514 nm) we have observed a strong fluorescence background and bleaching phenomena which caused a dramatic intensity reduction of the SERS bands. For this reason, the experimental set up described in material and methods has been optimized using the 633 nm light source.

3.3.2 Az-assisted capture of p53 as revealed by SERS

We have noted that the p53-(4-ATP-Np) system exhibits a tremendous enhancement of the Raman signal, with vibrational features well distinguishable and stable in time.

As already mentioned, for the detection of p53 we have flowed the p53-(4-ATP-Np) solution onto a capture platform made up of an Az monolayer, that successively has been rinsed several times to remove the unbound p53-(4-ATP-Np).

Fig. 3.5 shows SERS spectra of such an Az substrate, before (Fig. 3.5 A) and after the treatment with decreasing concentrations of p53 (Fig. 3.5 B, C and D). In a control experiment we have dropped, on the Az-modified platform, 4-ATP-Np molecules (1 pM of gold Nps) without p53. The obtained spectrum resembled that of Fig. 3.5 A, thus revealing no recognition events. The characteristic fingerprint of our Raman marker can be instead clearly observed in Fig. 3.5 B, C and D, confirming the presence of p53 bound to Az.

We can note that the signal to noise ratio (S/N) is reduced with the decreasing of p53 concentration. In particular, below $5 \cdot 10^{-13}$ M (Fig. 3.5 D), S/N becomes too low (< 3) and therefore we have assumed such a concentration as the detection limit for p53 by our method.

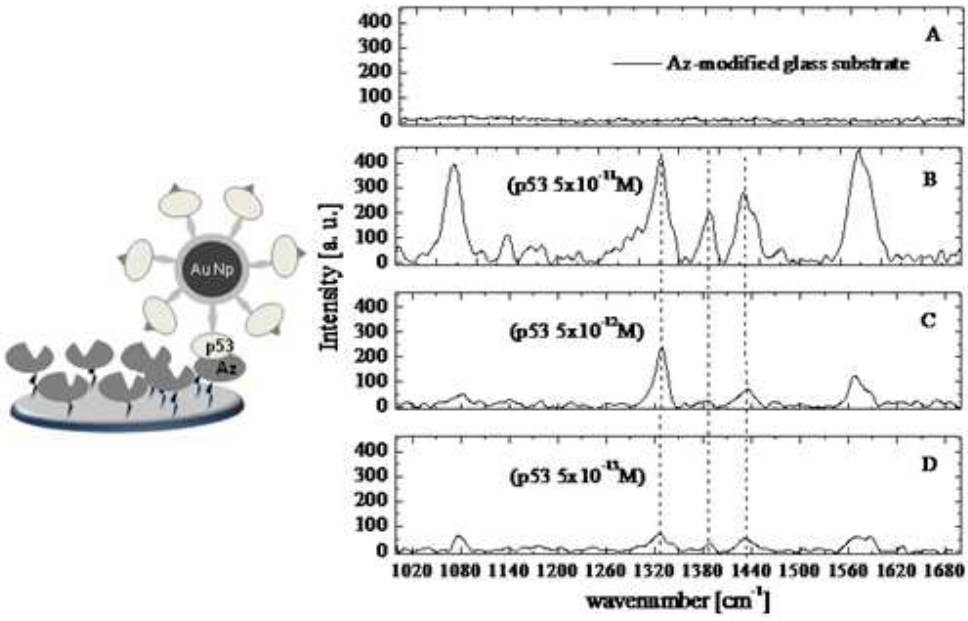

Fig. 3.5. Sketch of a p53-Az recognition event (left) and SERS spectra (right) of an Az substrate before (A) and after the incubation with the system p53-(4-ATP-Np), at different concentrations of p53: $5 \cdot 10^{-11}$ M (B), $5 \cdot 10^{-12}$ M (C), and $5 \cdot 10^{-13}$ M (D). Spectra were collected by an Obj 100x immersed in PBS.

We have observed SERS signals for a wide range of p53 concentrations (from low picomolar to nanomolar), which amply satisfy the requirements for detecting this protein within cellular lysates (Yeo et al., 2009; Wang et al., 2009).

Recent works report novel bioaffinity-based methods, employing consensus DNA sequences and monoclonal antibodies adsorbed on SPR sensor disks, gold electrodes and metal nanostructures, able to improve the tumour markers detection limits of the classic sandwich ELISA. These new techniques can reveal p53 in the order of picomolar concentrations (Wang et al., 2009; Jia et al., 2009), meaning that our detection value is comparable with the best results obtained by these biosensors (Jia et al., 2009). Nevertheless, our method has the advantages that low concentrations are easy to detect, the assay time is relatively fast, and it does not require multiple steps as the classical "sandwich enzyme immunoassay". In this respect, we would stress that the total assay time for a p53 quantitative revelation via ELISA is usually of about 2 days, with respect to about 6 hours may be estimated using the Az-assisted SERS procedure.

With regard to sub-picomolar concentrations of p53, when the SERS bands become hard to distinguish over the noise, Az-p53-(4-ATP-Np) biorecognition events may be more effectively ascertained by a topological investigation. To this aim, we have supported SERS detection by AFM imaging, since as explained in Appendix B it is able to reveal

single Az-p53 complex formation over the substrate. More specifically, by non contact AFM (NC-AFM), we have collected images in several different areas of the Az modified substrates, before (Fig 3.6 A) and after incubation with the p53-(4-ATP-Np) system corresponding to 0.5 pM p53 (Fig. 3.6 B).

We can note that the vertical profile of Fig. 3.6 A reveals the presence of an isotropic package with a mean height value of about 3.1±0.5 nm, and roughness R_q=1.7±0.5 nm, which are consistent with an Az monolayer (Andolfi et al., 2006). Otherwise, from Fig. 3.6 B we realize that after the incubation with the p53-modified Nps, large and rather regular spots appear on the substrate, having a mean height of 55±8 nm, which is in agreement with the nominal size of our gold Nps (50 nm). Since we have not detected these spots on Az substrates treated with 4-ATP-Np lacking p53 (data not shown), we can deduce that they are the result of p53-Az complexes formation.

We have estimated that these binding events are about the 20% of the total p53-(4-ATP-Np) incubated with Az, indicating that only a small fraction of functionalized Nps gives rise to successful interactions with the substrate.

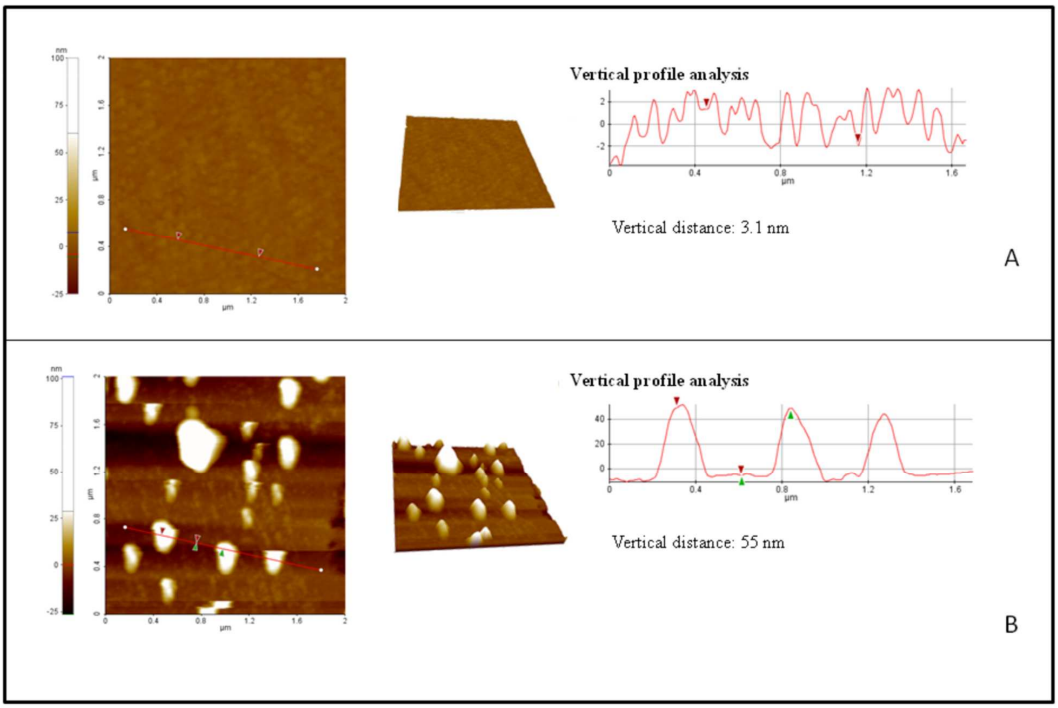

Fig. 3.6. NC-AFM images and vertical section analysis of the Az-functionalized substrate before (A) and after the incubation with a solution 0.5 10^{-12} M of p53 linked to 50 nm gold nanoparticles (B). The vertical profile analysis of panel B indicates the presence of a single p53 functionalized Np (z size 55±8 nm) recognized by Az.

Probably, the p53-Az binding capacity is affected by the scattered orientation of both Az (which is anchored to the substrate through its exposed lysine residues) and p53 (which is

anchored to the 4-ATP-Np system through its exposed histidine and tyrosine residues). We suppose that a different Az linking strategy, designed to favorite Az orientation in binding p53, may result in a higher binding frequency and consequently provide a further lowering of the p53 threshold sensitivity.

3.3.3 Selective Az-p53 recognition in a human Serum-like environment

In this section we focus on the selectivity of our proposed method, which is another crucial point for the specific detection of analytes.

As mentioned, an accumulation of p53 in the nuclei of several tumor cells has been detected. In this critical conditions, concomitant alterations of cell-free p53 levels within blood plasma may be expected to be found together with its immune response mediated antibodies as reported by an ever growing number of publications (Askari et al., 2001; Malviya et al., 2004; Rossner et al., 2004; Jia et al., 2009).

Therefore, an accurate monitoring of p53 in the plasma may be helpful as a bioindicator of prognosis and response to chemo- and radio-therapies in various malignant diseases (Shurbaji et al., 1995; Zusman et al., 1996; Shimada et al., 2000; Malviya et al., 2004; Psyrri et al., 2007) and even to relate their insurgence to genotoxic environmental carcinogens exposure (Li, 1997; Benini et al., 1998; Yang and Duerksen-Hughes, 1998; Hofseth et al., 2002; Rossner et al., 2004).

To understand if we were able to specifically reveal the tumour marker p53 among other proteins, we have analyzed different samples containing p53 at low concentration and a 10, 100 and 1000-folds molar excess of the Human Serum Albumin (HSA). The latter is in fact the most abundant protein in the human blood plasma.

To do this, we have used an alternative configuration in which Az has been conjugated with 4-ATP-Np by diazotization, and used as the SERS-probe to screen the various samples. The linking of Az to the Raman marker, if compared to the previous configuration, results in a very intense SERS signal due to the contribute of a higher number of molecules surrounding each Np (about 980 Az against 250 p53) (Delfino and Cannistraro, 2009), which provide a more rigorous correlation between number of the binding events (proportional to the intensity of the SERS signal) and the quantification of the p53 molecule probed onto the substrate. Moreover, Az has a strong and stable structure (Fuentes et al., 2004) which can undergo diazocoupling reaction, thus avoiding pretreatments and potential unfolding of the analyte p53.

Az structure is furthermore characterized by a peculiar Raman resonance spectrum, whose main bands, attributed to the Cu–S (Cys) and Cu–N (His) stretching modes (Bizzarri et al., 2008), are reported in Fig. 3.7. These fingerprint Raman bands of Az can be used to ascertain the success of the diazo-coupling reaction and, at the same time, exploited in Raman detection.

The spectrum shown as a dashed profile of Fig. 3.7 arises from 10 µg of Az deposited on a glass slide, whereas the spectrum shown as a solid line has been obtained with 10 ng of Az coupled to 4-ATP-Np and deposited on a glass slide. After the diazotization (solid profile), the fingerprint bands characteristic of Az are still clearly visible, indicating the success of the reaction. By comparing the two spectra of Fig. 3.7, we can note that the intensities of the bands are similar, even if the Az amount that provided the solid profile was 1000-fold lower than the Az that gave rise to the dashed one. It suggests that the coupling of Az to 4-ATP-Np provides an enhancement of the signal due to the SERS effect. These two characteristic bands have been clearly observed for Az conjugated to 4-ATP-Np down to 1 ng. Below this amount, S/N was drastically reduced and the overall SERS spectrum appeared similar to that of the Raman marker shown in Fig. 3.3 C.

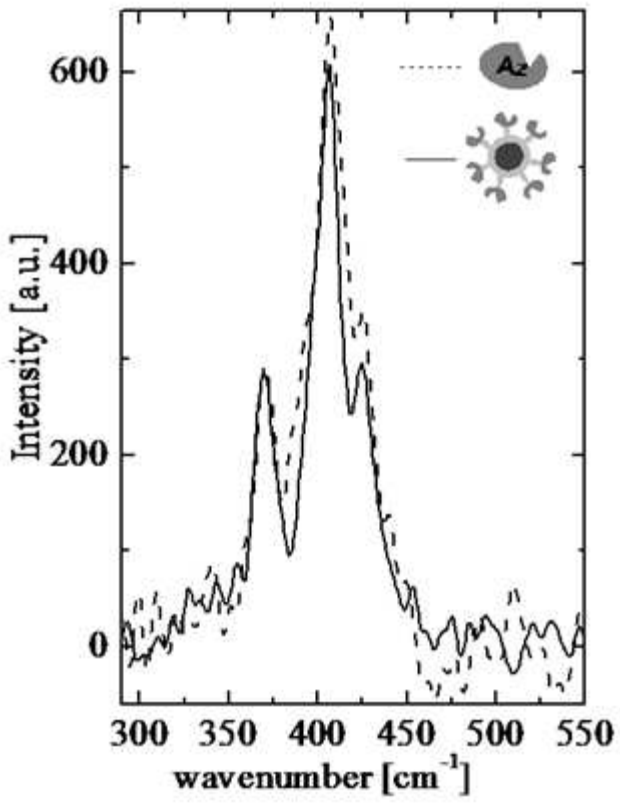

Fig. 3.7. Resonant Raman spectrum of solid AZ (10 µg) is shown as dashed line; SERS spectrum of solid Az-(4-ATP)-Np (10 ng Az) is shown as solid line. Spectra are recorded at 633 nm, in air (Obj 100x).

Our estimated SERS gain factor of the Az fingerprint bands has resulted too low to be effectively exploited in support of the ultrasensitive revelation of p53, which can instead be more suitably detected via the strong intense Raman marker of the Az-(4-ATP-Np) system. In spite of this we believe the here enlightened Raman amplification of Az may deserve more focused attention and planning leading to intriguing and promising SERS-based detection applications.

To investigate the selectivity of this system, we have incubated different samples, containing p53 and the protein HSA at various concentrations, on glass slides bearing aldehyde moieties on their surface, to allow the self-assembling of proteins (Domenici et al., 2011). Successively, after abundant rinsing, we have screened these substrates with the Az-(4-ATP-Np) probe.

Fig. 3.8 shows representative SERS spectra of samples with HSA/p53 molar ratio equal to 0, 10, 100 and 1000, and sample with only HSA, as probed by our Az-modified Nps. It is worth noting that the intensity of the SERS bands characteristic of the Az-(4-ATP-Np) system undergoes a sensitive decrease with the increasing of the HSA/p53 molar ratio (Fig. 3.8 A, B, C and D). These bands are instead completely absent on the substrate containing only HSA (Fig. 3.8 E). We can deduce that the SERS intensity of these spectra is related to the amount of p53 adsorbed onto the substrate, demonstrating that this method is potentially able to specifically identify p53 among other proteins.

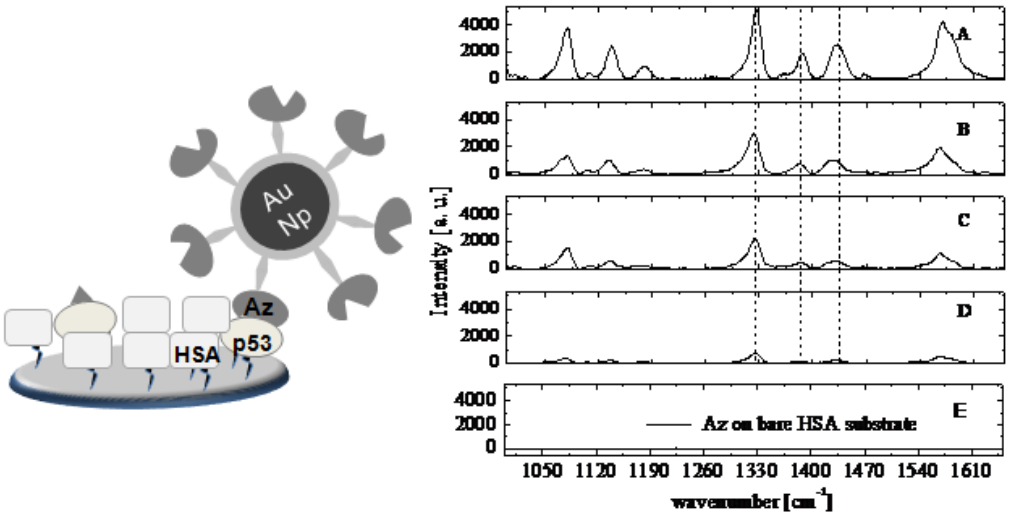

Fig. 3.8. Sketch of an Az-p53 recognition event in presence of an excess of HSA (left). SERS spectra (right) of the capture substrates made up of bare p53 (A) and of HSA/p53 at molar ratios equal to 10 (B), 100 (C), 1000 (D), and of bare HSA (E), after the incubation with the Az-(4-ATP-Np) system ($5 \cdot 10^{-9}$ M Az). SERS spectra were acquired with a laser source at 633 nm in air by a 100x obj.

Taken together, all the results of this study suggest that our Az-assisted SERS approach for the detection of p53 may provide the basis to design novel protocols for the early clinical screening of human and environmental pathologies. This strategy, in fact, can be extended to the detection of multiple specific analytes, thus providing a multiplex assay for an ultrasensitive and targeted screening.

3.4 Conclusions

The covalent binding of proteins to 4-ATP functionalized Nps via diazocoupling reaction has been here investigated, showing a strong enhancement of Raman signal with vibrational features well distinguishable and stable in time.

Accordingly, it appears to be a suitable Raman probe to be used to reveal the occurrence of biorecognition events between markers and receptors. Using p53 as a biological marker and Azurin as a receptor, we have identified p53 initially present in a solution at $5 \cdot 10^{-13}$ M. This approach points out the possibility of realizing an easy and rapid strategy to detect p53 under picomolar concentrations using Az. Because of the non-specific linking strategy it can be easily extended to the detection of other specific markers and implemented into a multiplex assay.

Moreover, the integration of SERS analysis with AFM imaging allows the detection of Az-p53 binding events even at a lower concentration of p53, thus opening new perspective for high-throughput screening of biomolecules with very high sensitivity.

Chapter 4

SPR detection of specific complexes made up of Az, p53 and Mdm2

4.1 Introduction

As already explained in Chapter 1, not only plasmonic-based methods to nano-bio-sensing can be effectively helpful in early screening of environmental and human pathologies, but they can also be considered as important tools in order to understand molecular mechanisms of important biological processes of biomedical relevance.

In this last aspect, a great deal of the scientific efforts, made toward the comprehension of the network controlling cell proliferation, is focused on the tumour suppressor role played by the transcriptional p53 protein (Toledo and Wahl, 2006). As mentioned in paragraph 1.2, human p53 consists of four main domains which are responsible for its transcriptional activation, DNA-binding and tetramerization functions (Lavin and Gueven, 2006; Veprintsev et al., 2006). When DNA damage is sensed, the p53 level rises and the protein binds to sequence-specific regulatory sites in the genome, thereby inducing the expression of genes that control the DNA repair and interrupting the cell growth until the damage is repaired; on the other hand, if the damage is too severe, p53 triggers the apoptotic cascade (Vogelstein et al., 2000; Lavin and Gueven, 2006).

p53 is mainly down-regulated by the oncoprotein Mdm2 which inhibits its transcriptional activity (Momand et al., 1992), shuttles p53 toward the cytoplasmic proteasome and promotes its ubiquitindependent degradation (Honda et al., 1997; Roth et al., 1998; Freedman et al., 1999).

Such a regulative action of Mdm2 has been demonstrated to be coupled to the formation of a complex with p53 (Momand et al., 1992; Moll and Petrenko, 2003), in which the N-terminal regions of both proteins come into close contact (Kussie, 1996; Schon et al., 2002). Detailed information on the overall structure of the corresponding complex is however missing to date, mainly due to the lack of the crystallographic pictures of both full-length proteins undergoing the interaction. Most of the structural and kinetic information currently available is derived from studies performed only on partial domains of both p53 and Mdm2 (Kussie, 1996; Lai et al., 2000; Schon et al., 2002; Chi et al., 2005). A binding study of the complex involving the two full-length, native proteins has been conducted by Atomic Force Spectroscopy (AFS), a new nanotechnological tool able to

investigate even a single couple of interacting partners (see paragraph B.6) to complement biochemical information on biorecognition processes (Bizzarri and Cannistraro, 2010). AFS put into evidence the occurrence of a specific complex between p53 and Mdm2 characterized by a dissociation rate constant (k_{off}) of about 1.5 s^{-1} (Funari et al., 2009).

The importance of investigating this interaction is not limited to structural or kinetic aspects; indeed stabilizing and enhancing p53 tumour-suppression function in cancer cells, even by inhibiting its physical interaction with Mdm2, is the main focus of anticancer drug discovery (Klein and Vassilev, 2004; Bossi and Sacchi, 2007).

In this context, we have shown in the paragraph 1.2 that the purified bacterial copper-containing protein Azurin (Az) plays a prominent anticancer role. Several *in vitro* and *in vivo* studies have shown that the protein can preferentially enter cancer cells and induce their apoptotic death (Yamada et al., 2002; Yamada et al., 2004; Punj et al., 2004; Yamada et al., 2005). Interestingly, it has been demonstrated that this proapoptotic action of Az is concomitant with the formation of a complex with p53, thereby leading to both its stabilization and intracellular level increase (Yamada et al., 2002). The Az-p53 binding process has been therefore investigated by means of different experimental methodologies.

Site direct mutagenesis has shown that Az interacts through two methionine residues, located within its hydrophobic patch surrounding the copper atom, with a not univocally established region of p53 (Yamada et al., 2002). A number of experimental and computational studies have hypothesized the occurrence of either a direct interaction of Az with the p53 N-terminal domain (aa 1-93) (Apiyo and Wittung-Stafshede, 2005; Taranta et al., 2008b) or, alternatively, with the DNA-binding domain (DBD) (aa 94-292) of p53 (De Grandis et al., 2007; Yamada et al., 2009). The specificity of the Az-p53 interaction has been demonstrated also by AFS (Taranta et al., 2008a) and the corresponding k_{off} value has been measured ($9 \cdot 10^{-2}$ s^{-1}), while the association rate constant (k_{on}) and the dissociation constant (K_d) of the complex, involving the two full-length proteins, have been only estimated.

Despite the fact that the molecular mechanism involved in the Az anticancer action it is not fully understood it is clear that this protein is able to stabilize p53, apparently acting as an antagonist of Mdm2. An appealing hypothesis to this end could be that binding Az to p53 might prevent Mdm2 and p53 from association and, thus, p53 from degradation. In that context, our group has conceived unbinding experiments by AFS (Funari et al., 2009) that ruled out a direct binding competition between Az and Mdm2 with respect to p53, and have suggested the possible formation of a ternary interaction among Az, Mdm2 and p53.

Since such a ternary interaction could contribute to open a new scenario on the anticancer action of Az, we have then performed a detailed kinetic study of the binding among Az, Mdm2 and p53, by means of Surface Plasmon Resonance (SPR) analysis. Indeed, as mentioned in paragraph 1.1.1, SPR represents a strategic tool in protein-binding studies, especially suited for sensitive kinetic process investigations, in real time and without labeling procedures (Cooper, 2003).

4.2 Results and discussion

4.2.1 Binding kinetic of the Mdm2-p53 complex

In a typical SPR experiment a protein-protein binding process can be followed in real time by registering the time varying shift of the optical SPR angle which characterizes the region very close to a sensor surface, where the reaction occurs.

By this methodology we have detected the specific interaction between the entire Mdm2 and p53 proteins and the resulting sensorgrams are shown in Fig. 4.1.

Before proceeding with the experiments, we have checked the purity, folding and functionality of p53 and Mdm2 samples as described in paragraph 2.1; we have then monitored the preparation of the p53 modified sensor disks by the AFM analysis shown in paragraph 2.3.1. We have observed that after the incubation of a gold-disk with the p53 solution, the roughness (Rq), measured in an area of 1.0x1.0 μm^2 over the sample surface, was changed from 0.5±0.1 to 1.0±0.1 nm, indicating the successful deposition of p53 proteins strongly adhering to the substrate (Domenici et al., 2011).

In order to obtain accurate and reproducible kinetic data, we have repeatedly collected SPR sensorgrams obtained from the injection of Mdm2 protein solutions, at six different concentrations (ranging from 0.1 to 2 µM), on the sensor disks covered by p53. The SPR signal as a function of time provides the binding kinetic characterization of the complex. Upon Mdm2 injection (at an assigned concentration), the observed time-dependent signal increased up to a plateau as due to the Mdm2-p53 association (equation 2.1); after removal of the Mdm2 solution and subsequent buffer injection, the observed decreasing profile characterizes the kinetics of the Mdm2-p53 dissociation (equation 2.2). The kinetic rate constants and equilibrium dissociation values, obtained from the best fits of the SPR signals, as described in paragraph 2.3.3, shown in Fig. 4.1, are summarized in Tab. 4.1 (first row). They are consistent with the typical values of ligand-receptor pairs undergoing a dynamic, transient interaction (Nooren and Thornton, 2003).

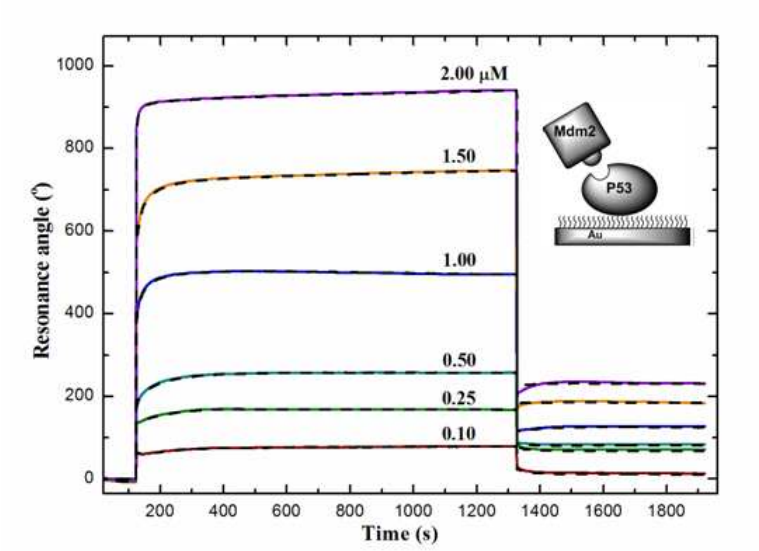

Fig. 4.1. Surface Plasmon Resonance sensorgrams for the binding-unbinding screen of Mdm2 on p53-modified sensor disk, with a cartoon of the interaction geometry. The SPR angle shift as function of time after injection and removal of the Mdm2 solutions (TST buffer, pH 7.2) at six concentrations is shown (solid profiles). The Mdm2-p53 association phases were registered over 20 min at flow rate of 50 μl min^{-1} and T=25°C. Best fits (dashed black profiles) were performed by using simultaneous nonlinear regression analysis to a reversible bimolecular interaction model (see experimental procedures section).

The k_{off} value is very close to that obtained by AFS (1.5 s^{-1}) for the Mdm2-p53 complex, always formed by full-length partners (Funari et al., 2010) and the K_d value is also consistent with the dissociation constant (K_d = 0.2 μM) measured in a stopped-flow fluorimetric study (Schon et al., 2002) on the interaction between the N-terminal polypeptide of both Mdm2 and p53. This indicates that, even if the main Mdm2 binding site presumably involves a short helix formed by residues 18-26 of p53 (Kussie, 1996; Schon et al., 2002), the two cognate binding sites of the complex undergo a biorecognition process without significant steric hindrance as due to the presence of the entire milieu of the proteins.

It has been recently suggested that the Mdm2-p53 association may also be triggered by initial molecular collisions and multiple approach orientations involving the entire polypeptide chain (which is quite extended and almost completely unfolded) of the p53 N-terminal portion (Dawson et al., 2003; Chi et. al., 2005; Toledo and Wahl, 2006). Therefore, the previous Mdm2-p53 complex studies, mostly performed only on their partial domains, provide dissociation constant values ranging from nano- to micro-Molar, according to the different peptide length considered (Lai et al., 2000; Ma et al., 2006; Ferreon et al., 2009). A ten-fold stronger dissociation constant (K_d = 0.3 μM) has been found when, at least, the entire p53 was used (Dawson et al., 2003). Such a value shows a

better agreement with the present SPR results and significantly points out that a study involving the two full-length proteins would be better suited for a more realistic and comprehensive knowledge of the p53-Mdm2 interaction.

4.2.2 Binding kinetics and secondary folding of the Az-p53 complex

Before considering the effect of Az on the formation of the Mdm2-p53 complex, we have performed the binding kinetics measurements also on the binary complex formed by the two entire Az and p53 proteins. The SPR sensorgrams, shown in Fig. 4.2, have been obtained by injecting Az at seven different concentrations, ranging from 0.25 to 4 μM, onto the p53-functionalized substrate.

The obtained binding parameters, shown in Tab. 4.1, are consistent with the occurrence of a specific Az-p53 complex. While the k_{off} value is in good agreement with that obtained by AFS on the same complex at the single molecule level (Taranta et al., 2008a), the corresponding k_{on} and K_d values are instead measured here for the first time.

Quite interestingly, the dissociation constant of the Az-p53 complex results to be only three-fold lower than that of the Mdm2-p53 complex, although both the k_{off} and k_{on} values are found much lower than those relevant to this complex (compare the first to the second row of Tab. 4.1). Indeed, two interaction processes with similar affinity may display widely different association and/or dissociation timescale, according to the biochemical mechanism underlying the functional interaction (Robert et al., 2007).

In particular, regulative functions requiring rapid transient interactions, could plausibly be characterized from short lifetime (the inverse of k_{off} provides the lifetime of the corresponding complex). In this respect, the Az-p53 complex which displays a higher lifetime is thereby characterized by a more stable interaction than that corresponding to the Mdm2-p53 complex.

On the other hand, the k_{on} value characterizes the inverse of association time at unit concentration of the components and molecular recognition may be driven by binding-induced conformational changes, which could rise the binding association time (lower k_{on}) reasonably to lead the complex to a more stable final state (with lower k_{off}) (Boehr et al., 2009; Robert et al., 2009).

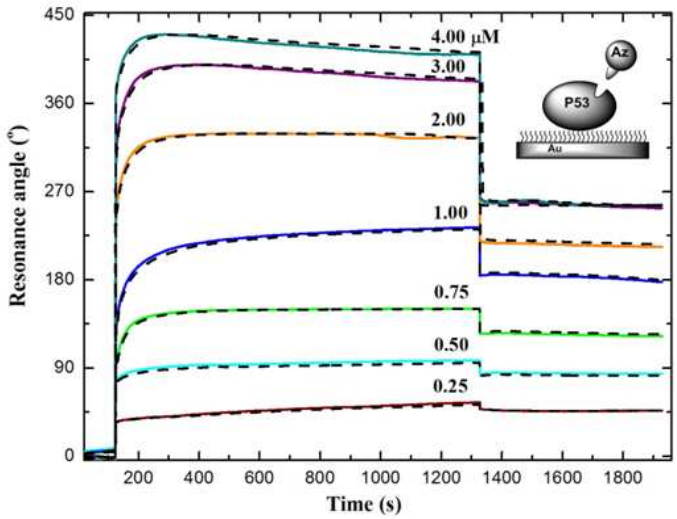

Fig. 4.2. Surface Plasmon Resonance sensorgrams for the binding-unbinding screen of Az on p53-modified sensor disk, with a cartoon of the interaction geometry. The SPR angle shift as function of time after injection and removal of the Az solutions (PBS buffer, pH 7.2) at seven concentrations is shown (solid profiles). The Az-p53 association phases were registered over 20 min at flow rate of 50 μl min^{-1} and T=25°C. Best fits (dashed black profiles) were performed by using simultaneous nonlinear regression analysis to a reversible bimolecular interaction model (see experimental procedures section).

Since similar binding-induced structural changes have been observed also in many protein-protein interactions involving natively unfolded proteins, such as p53 (Pontius, 1993; Dahlman-Wright, 1995; Uversky, 2002; Dyson and Wright, 2002; Kumar and Thompson, 2003) we have conceived a far-UV CD experiment in order to investigate the effect of Az binding on the p53 folding (see also paragraph 2.3.4).

The CD spectrum recorded from the Az/p53 complex at 1:1 molar ratio shows significant differences with respect to that from wild-type p53 (see Fig. 4.3).

In particular, the appearance of both a deep minimum centred at around 206 nm and a shoulder at 220 nm, points out the formation of an alpha-helix motif. Since Az displays a rigid folding (Adman, 1991), the observed changes can be attributed to an Az-induced folding in p53.

The data analysis has quantified that the Az-induced secondary structure of p53, from unfolded state to alpha-helix, is of about 10%. Such a conformational change could involve intrinsically unfolded regions within the p53 N-terminal domain (Apiyo and Wittung-Stafshede, 2005) where the Mdm2 binding site is supposed to be located (Kussie, 1996; Dawson et al., 2003; Apiyo and Wittung-Stafshede, 2005; Vise et al., 2005).

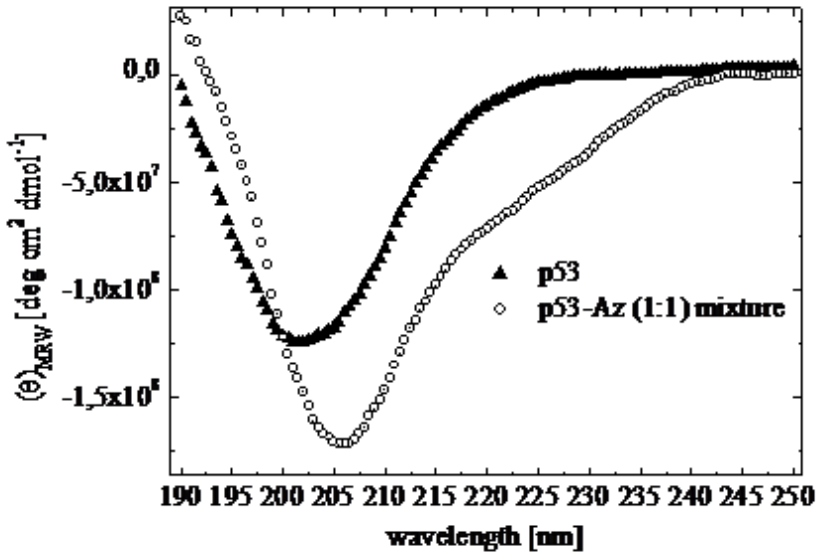

Fig. 4.3. Far-UV CD spectra of p53 alone (black triangles); and in the presence of Az (circles) (1:1 molar ratio) acquired at 25°C in TST buffer solution (pH 7.2). Buffer signals was subtracted for p53 alone. The spectrum of Az-p53 solution was corrected for Az and buffer contributions.

4.2.3 Binding kinetics of the Az-p53-Mdm2 complex

In this section, we report on the SPR analysis of the Az-p53-Mdm2 ternary interaction as hypothesized by AFS in ref. (Funari et al., 2010). We aim at both extracting the relevant kinetic parameters and ascertaining if the observed Az-p53 specific interaction can interfere with the binding kinetics of the Mdm2-p53 complex. To this end, we need to consider both the binding kinetics of Az with the Mdm2-p53 complex and the binding kinetics of Mdm2 with the Az-p53 complex.

According to previous SPR investigations performed on a ternary complex interaction (Banaszynski et al., 2005), for the first binding configuration, we have treated p53, immobilized on the SPR substrate, with an excess of Mdm2 solution until its binding capacity for Mdm2 has resulted totally reduced as checked by SPR sensorgram, and then we have injected the Az solution on the Mdm2-p53 complex immobilized on SPR sensor disk to analyze the interaction kinetics. Experiments have been performed also by injecting Az mixed with Mdm2 to avoid equilibrium perturbation on the Mdm2-p53 interaction and to ascertain that the SPR response was really due to the specific binding of Az to p53, in turn associated with Mdm2 (see also experimental procedures section).

The sensorgrams obtained at six different concentration of Az are shown in Fig. 4.4.

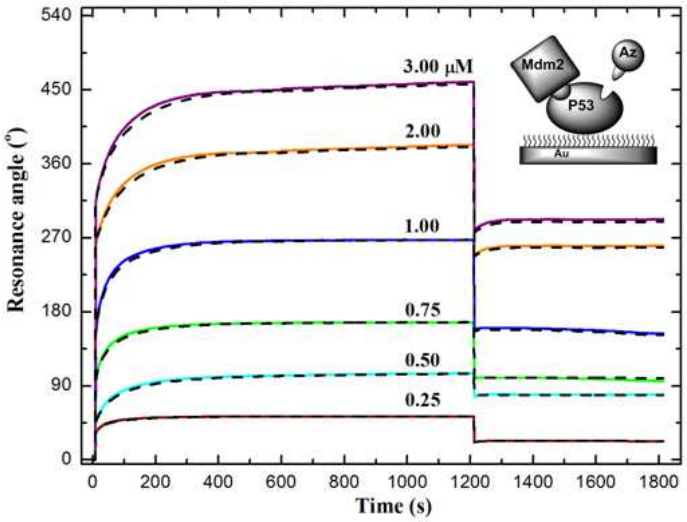

Fig. 4.4. Surface Plasmon Resonance sensorgrams for the binding process of Az with Mdm2-p53 complex, with a cartoon of the interaction geometry. The SPR angle shift as function of time after injection and removal of the Az solutions (PBS buffer, pH 7.2) at six concentrations is shown (solid profiles). Best fits (dashed black profiles) were obtained by using simultaneous nonlinear regression analysis to a reversible bimolecular interaction model (see details in the experimental procedures section).

The corresponding kinetic rate constants and equilibrium dissociation values, which have been reported in Tab. 4.1 (third row), are found almost equivalent to those obtained for the Az-p53 binary complex (compare the second to the third row of Tab. 4.1).

This result confirms that Az and Mdm2 do not compete for the same binding site within p53, but they are involved a ternary interaction (Az-p53-Mdm2), as already hypothesized (Funari et al., 2010).

We have then studied the interaction of Mdm2 with the Az-p53 complex as follows. After having treated the p53 immobilized on the substrate with an excess of Az solution to saturate its Az binding sites, we have injected the Mdm2 solution at the same six concentrations used for the previous experiment on the Mdm2-p53 binary complex. Experiments have been performed also by injecting Mdm2 mixed with Az to avoid equilibrium perturbation on the Az-p53 interaction and to ascertain that the SPR response was due to the specific binding of Mdm2 to p53 associated with Az. The obtained SPR sensorgrams are shown in Fig. 4.5 and the extracted kinetic parameters are summarized in Tab. 4.1 (fourth row).

Very interestingly, a comparison of the latter SPR analysis with that of the Mdm2-p53 binary interaction indicates that Az affects the interaction of Mdm2 with p53 by reducing of more than four times the corresponding association rate constant (k_{on} goes from = $2.1 \cdot 10^6$ to $5.0 \cdot 10^5$ M^{-1} s^{-1}, in the absence and in the presence of Az, respectively); whereas

the corresponding k_{off} values resulted to be unchanged and consequently the corresponding equilibrium dissociation constant resulted to be increased (compare fourth to the first row of Tab. 4.1).

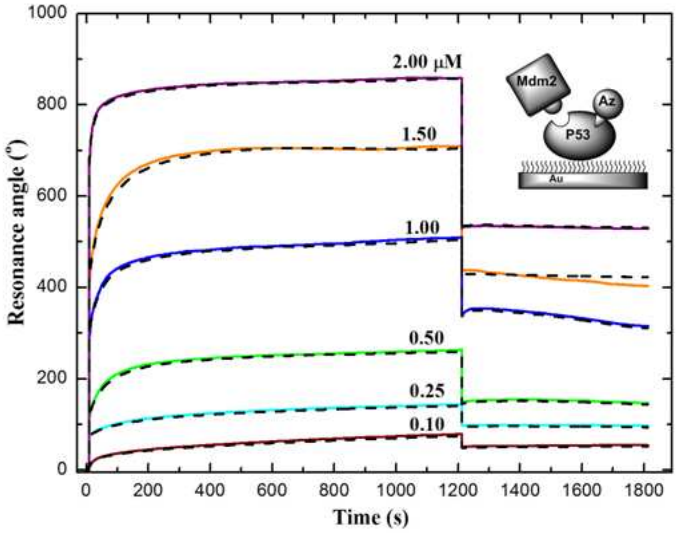

Fig. 4.5. Surface Plasmon Resonance sensorgrams for the binding process of Mdm2 with Az-p53 complex, with a cartoon of the interaction geometry. The SPR angle shift as function of time after injection and removal of the Mdm2 solutions (TST buffer, pH 7.2) at six concentrations is shown (solid profiles). Best fits (dashed black profiles) were obtained by using simultaneous nonlinear regression analysis to a reversible bimolecular interaction model (see details in the experimental procedures section).

In other words, all these SPR results indicate that the specific binding of Az to p53 induces a lowering of the association kinetics and binding affinity of the Mdm2-p53 complex, without obstructing the Mdm2 binding site on p53.

Interesting questions arise then about the mapping of the ternary interaction binding sites and, consequently, about the mechanism of the Az action on the binding kinetics of the Mdm2-p53 complex. Since it is well known that Mdm2 binds to p53 at its N-terminal transactivation domain (Kussie, 1996; Schon et al., 2003), the main issue regards the Az binding site of p53 which has not been, up to date, univocally identified. Indeed, it has been reported that Az can either bind the same N-terminal domain of p53 (Apiyo and Wittung-Stafshede, 2005; Taranta et al., 2008a; Gabellieri et al., 2009) or its DBD (De Grandis et al., 2007). In the former case, however, it should be admitted, in the light of the present results, that Az would somehow affect the Mdm2-p53 recognition process without hindering the accessibility of Mdm2 to its binding pocket on p53. The latter possibility has been previously predicted by a docking study (De Grandis et al., 2007) and has very recently gained experimental ground from studies using the Az fragment p28 (aa 50-77)

(Taylor et al., 2009), which has been found to retain *in vivo* the biochemical interaction and anticancer action of Az (Yamada et al., 2009).

Complex	Binding rate constants and equilibrium dissociation constant
MdM2/p53 binary	$k_{off} = 0.8 \pm 0.3\ s^{-1}$ $k_{on} = (2.1 \pm 0.2)10^{6}\ (Ms)^{-1}$ $K_d = (0.4 \pm 0.1)10^{-6}$ M (χ^2 = 98 %)
Az/p53 binary	$k_{off} = (9.4 \pm 0.7)10^{-2}\ s^{-1}$ $k_{on} = (8.2 \pm 0.5)10^{4}\ (Ms)^{-1}$ $K_d = (1.2 \pm 0.1)10^{-6}$ M (χ^2 = 95 %)
Az/(p53-MdM2) ternary	$k_{off} = (9.0 \pm 0.3)\ 10^{-2}\ s^{-1}$ $k_{on} = (6.8 \pm 0.5)10^{4}\ (M\ s)^{-1}$ $K_d = (1.3 \pm 0.1)\ 10^{-6}$ M (χ^2 = 99 %)
MdM2/(p53-Az) ternary	$k_{off} = (0.6 \pm 0.2)\ s^{-1}$ $k_{on} = (5.0 \pm 0.3)10^{5}\ (Ms)^{-1}$ $K_d = (1.2 \pm 0.4)10^{-6}$ M (χ^2 = 97 %)

Tab. 4.1. Kinetics and equilibrium constants measured by SPR of the binary and ternary complexes formed by the full-length proteins Az, Mdm2 and p53. The global analysis was performed by the Clump biosensor software.

Wherever Az is binding to p53, the protein is able to induce a weakening of the Mdm2-p53 interaction by a non competitive inhibition mechanism, which should be figured out as a long range binding regulation. In other words, we could admit the possibility that the observed change in the p53 folding could reflect an allosteric regulation mechanism by which Az may affect the p53 favourite conformation required for recruitment of the Mdm2-p53 complex (Boehr et al., 2009; Hilser et al., 2010).

Inhibition of the p53 interaction with the oncogenic protein Mdm2 is of utmost therapeutic value in cancer treatment. Up to date, the research has focused on therapeutic agents, natural or synthetic inhibitors (Klein and Vassilev, 2004) suitably designed for a competitive inhibition of Mdm2-p53 interaction by targeting the p53 binding site of Mdm2. However, such p53 activation pathway can lead to toxicity in normal tissues with relatively high proliferative index (Klein and Vassilev, 2004).

In this scenario, the evidenced allosteric inhibition mechanism of Mdm2-p53 interaction, could represent a novel biochemical rationale to design new drugs interacting with p53 for restoring its tumour suppressor activity. Indeed *in vivo* studies have shown that even a

partial inhibition of Mdm2-p53 binding is sufficient to activate the p53 pathway, with low collateral effects (Klein and Vassilev, 2004).

4.3 Conclusion

The binding kinetics of the interaction between the full-length Az, Mdm2 and p53 proteins has been here investigated by SPR, and novel molecular details concerning the interaction between these three proteins have been obtained. Our results are consistent with previous works reporting evidence of complexes formation between p53 and both Mdm2 and Az. Furthermore, our study reveals the occurrence of a ternary interaction among these proteins, and provides the corresponding k_{off}, k_{on} and K_d values. The SPR analysis has revealed that the interaction between Az and p53 is significantly stable and not affected neither by the immobilization strategies used nor by the binding of Mdm2 to p53.

On the other hand our data disclose the Az capability of affecting the Mdm2-p53 interaction by reducing their association rate constant. Moreover, the Az-induced folding in p53, evidenced by CD measurements, suggests that Az could be able to stabilize p53 by allosteric inhibition of the functional, regulative interaction between Mdm2 and p53. The highlighted noncompetitive modulation of the p53 activity may represent an interesting, novel p53-activating strategy to design anticancer drugs to treat tumours in which p53 has retained its wild-type structure and function, and provides further insights into the mechanism underlying the observed anticancer action of Az.

Conclusions and perspectives

In the present study, we have considered advanced biophysical methodologies in the attempt to disclose new interesting aspects connected with biorecognition processes of potential diagnostic and therapeutic relevance. To this aim we have focused on the recently discovered interaction of the tumour suppressor protein p53 with the bacterial protein Azurin because of their growing biomedical interest.

We have realized an innovative SERS-based signal amplification method able to detect Az-p53 binding events under picomolar concentration of p53, thus improving detection limits of traditional analytical methods. We have also highlighted the advantages of a combined use of surface plasmons absorption analysis and AFM imaging.

By using the SPR technology we have followed the interaction between the entire Az, p53 and Mdm2 proteins in real time, without labelling procedures and under physiological condition, providing novel and accurate binding kinetic information connected with the anticancer role of Az-p53 binding.

The realization of p53-receptor substrates has allowed to maintain the native folding of the entire p53, which tends to form insoluble aggregates in bulk solution. The global SPR results indicate that the Az-p53 complex is specific, stable in time and not affected neither by the immobilization strategies used nor by the presence of Mdm2. On the other hand, Az induces a non competitive inhibition on the Mdm2-p53 binding by a significant reduction of their association rate constant.

It is worth noting that the current study, involving the properly folded full-length proteins, provide a more realistic and comprehensive knowledge of their interaction. As a consequence, the observed non competitive modulation of the p53-Mdm2 binding not only suggests new insights into the mechanism underlying the *in vitro* and *in vivo* observed anticancer action of Az, but it may also represent an intriguing, novel p53-activating strategy to design anticancer drugs for the treatment of tumours in which p53 has retained its wild-type structure and function.

Since p53 can be a bioindicator of tumour invasiveness and a molecular marker to identify carcinogens, our proposed Az-assisted SERS approach is also a promising candidate to realize a more accurate, easy and rapid predictive assay for malignant diseases and environmental stressors. Moreover, because of the non-specific linking strategy, this

method can also be easily extended to the detection of other specific markers and implemented into a multiplex assay.

To date, the physical bases of the nano-optical sensing are still in vivid scientific debate (i.e. SERS and optics of nanoparticles). In spite of that, also at the light of the present results, we believe that merging of bio-technology with surface plasmons phenomena will ultimately lead to the realization of innovative signal amplification methods and nano-bio-sensing strategies that will be important in numerous aspects of society, varying from effective and efficient medical diagnosis and therapeutics to a more comprehensive monitoring of ecotoxicity and human risks.

APPENDIX A

Physics of surface plasmons

A.1 SPR and metal surfaces

A.1.1 Surface plasmon dispersion equations

Essential for the generation of surface plasmons (SPs) is the presence of free electrons at the interface of two materials which almost always implies the use of a metal surface where free conduction electrons are abundant.

Surface plasmons can be considered as propagating electron density waves occurring at the interface between metal and dielectric. Alternatively, surface plasmons can be viewed as electromagnetic waves strongly bound to this interface; it is found that the surface plasmon field intensity at the interface can be made very high, which is the main reason why SPR is such a powerful tool for many types of interface studies.

Experimental research on SPs started with electron beam excitation; in 1968, optical excitation was demonstrated by Otto (Otto, 1968) and Kretschmann and Raether (Kretschmann and Raether, 1968).

To date there are several approaches that all result in the dispersion relation for a SP, that is a relation between the angular frequency ω and the wavevector k (Raether, 1988). By following the approach suggested by Cardona (Cardona, 1971), for any interface between two media, the complex reflection coefficient r_p for a p-polarized incident light electric field (the electrical field vector is in the plane of incidence) is described by Fresnel's equations (Reitz et al., 1993):

$$r_p = \frac{E_r}{E_i} = \left|r_p\right| e^{j\varphi} = \left|\frac{\tan(\alpha-\beta)}{\tan(\alpha+\beta)}\right| e^{j\varphi} \tag{A.1}$$

where E_i and E_r are the incident and reflected electric fields, respectively and the angles α and β are defined as shown in Fig. A.1.

Of course, the angle α and β are related by Snell's law. In addition, a phase change φ of the reflected field relative to the incident field occurs, depending on the refractive indices of the materials involved. For the reflectance, defined as the ratio of the reflected intensities, the following relation holds:

$$R_p = \left|r_p\right|^2 . \tag{A.2}$$

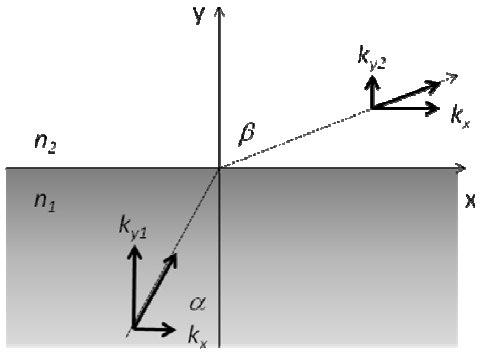

Fig. A.1. Refraction of light at an incident angle α, at an interface of two materials with refractive indices n_1 and n_2. Definition of axis system and quantities.

Following Cardona (Cardona, 1971), two special cases exist: if $\alpha+\beta = \pi/2$, then the denominator of equation (A.1) becomes very large and thus R_p becames zero. This situation describes the Brewster angle, where there is no reflection for p-polarized light.

The other special case occurs when $\alpha-\beta = \pi/2$: we see from equation (A.1) and (A.2) that R_p becomes infinite or in other word there is a finite E_r, for a very small E_i. This circumstance correspond to resonance. From this relation between α and β we can deduce the dispersion relation if $\alpha-\beta = \pi/2$, then the $\cos(\alpha) = -\sin(\beta)$ and $\tan(\alpha) = k_{1x}/k_{1y} = -n_2/n_1$. For the components of the wavevectors $k=(k_x, k_y)$ we can write:

$$k_x^2 = k_1^2 - k_{y1}^2 = k_1^2 - k_x^2 \frac{\varepsilon_1}{\varepsilon_2} \tag{A.3}$$

$$k_x = \frac{\omega}{c}\sqrt{\frac{\varepsilon_1\varepsilon_2}{\varepsilon_1+\varepsilon_2}} \text{ and } k_{yi} = \frac{\omega}{c}\sqrt{\frac{\varepsilon_i^2}{\varepsilon_1+\varepsilon_2}} \tag{A.4}$$

Where ε_1 and ε_2 are the dielectric constants (dielectric constant and refractive index are related by $\varepsilon=n^2$) of materials 1 and 2, respectively, and i=1 or 2.

Equation (A.4) is the sought SPR dispersion equation for an interface between two half infinite media.

When the medium 2 is a metal and thus it contains a large number of free electrons and the consequence is that at an angular frequency $\omega<\omega_p$, its dielectric constant ε_2 will be negative (Reitz et al., 1993):

$$\varepsilon_2(\omega) = 1 - \frac{\omega_p^2}{\omega^2} \tag{A.5}$$

$$\omega_p = \sqrt{\frac{4\pi n_e e^2}{m_e}} \tag{A.6}$$

Where ω_p is the so called plasma frequency, n_e is the free electron density and e and m_e are the electron charge and mass, respectively. Generally this implies that for $\omega<\omega_p$ no

electromagnetic field can propagate in a metal. More specifically, provided that $\varepsilon_2 < -\varepsilon_1$, we find for the interface that k_{yi} is imaginary, whereas k_x remains real. Thus an electromagnetic wave exists, propagating strictly along the interface, with evanescence tails extending into both sides of the interface. To get a feeling for the quantities involved, it is instructive to calculate penetration depths for a real case, on the basis of equation (A.4). We take λ =700 nm, thus ω=2.69·10^{15} s^{-1} and a gold/water interface. At this wavelength $\varepsilon_{gold} \sim$ -16 and $\varepsilon_{water} \sim$ 1.77. we calculate for the penetration depths $1/k_{y,\,water}$=238 nm and $1/k_{y,\,gold}$=26 nm.

Now all ingredients are available to appreciate the use of SPR in sensor applications. Let us assume that we are a situation where molecules X are allowed to adsorb to the water/metal interface. We can view this as a process where water molecules are replaced by molecules X. Because generally $\varepsilon_x \neq \varepsilon_{water}$, the average dielectric constant close to the interface will change.

Equation (A.4) then describes the concomitant change of the wavevector k_x. Because the SP field is evanescent in the direction perpendicular to the interface, a change of the dielectric constant ε_2 is only detectable in SP characteristics if this change occurs within the penetration depth of the SP field: an SPR sensor will only be sensitive to molecular processes (binding, adsorption, etc.) that occur at a distance to the metal surface that is roughly half the wavelength of the used light.

A.1.2 Excitation and surface plasmons

By substitution of equations (A.5) and (A.6) in equation (A.4) we obtain a graphical representation of the SPR dispersion relation in Fig. A.2. In the same figure, the dispersion relation for “normal” light is depicted (line a). We immediately see that, apart from the origin, there is no point where the SPR curve intersect, implying that in this geometry “normal” light cannot simultaneously provide the correct wavevector and angular frequency to excite a surface plasmon. One way to circumvent this problem is to introduce a second interface, as depicted in the inset to Fig. A.2. Here a thin metal layer (dielectric constant ε_m) is sandwiched between two dielectric materials 1 and 3 with different dielectric constants ε_1 and ε_3 with $\varepsilon_1 > \varepsilon_3$. By applying Fresnel’s equation to the interfaces, more complicated dispersion equations are found than equation (A.4); however the essential physics remains unchanged.

We now find two dispersion equations for k_x, one for each interface, and we see that the line representing the dispersion relation for “normal” light in medium 1 (line b) intersects the SP dispersion line for the metal/medium 3 interface. This indicates that light incident

from medium 1 can excites SPs: by proper adjustment of the incoming angle α, we can tune the incoming wavevector: $k_x=kn_1\sin(\alpha)$ to match the wavevector necessary for SP excitation.

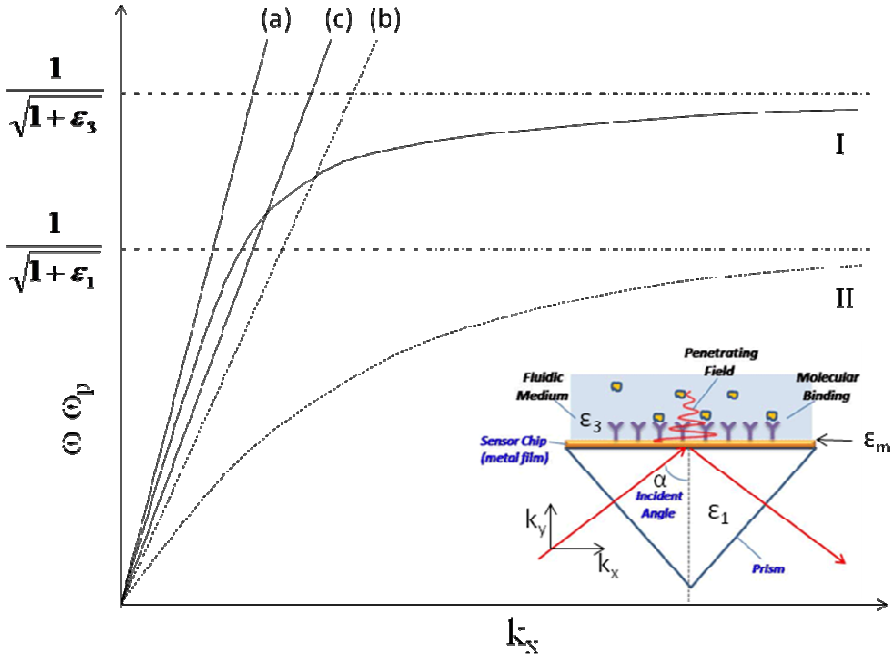

Fig. A.2. Dispersion relation for surface plasmons. Curves I and II represent the SP dispersion for the interfaces $\varepsilon_3/\varepsilon_m$ and $\varepsilon_1/\varepsilon_m$, respectively. The lines a and b are the dispersion relations for "normal" light in ε_3 and ε_1, respectively, which are dependent on the angle of incidence α. In the experimental setup as indicated in the inset. By varying α, any line c between the lines a and b can be realized.

In this way, any k_x between two lines, labeled a and b in Fig. A.2 can be set. As an example, one such line, labeled c, is indicated. This so-caled attenuated total reflection (ATR) technique was first demonstrated by Kretschmann and Rather and has since then almost become the standard technique for SP excitation.

Another way of providing a wavevector appropriate for SP excitation is the use of a metal layer on which a periodic structure is prepared (Cullen e al., 1987; Hecht, 2002). When the light with wavevector $k_x=(2\pi/\lambda)n_1\sin(\Theta)$ falls on such a structure, this acts as a diffraction grating and diffraction orders m=0 ±1 ±2…Again the wavevector k_x can be tuned to the SPR wavevector, given by equation (A.4), by changing the incident angle.

As already pointed out, SPs are conductivity fluctuations brought about by collective surface charge density oscillations. These charge density waves have to be excited by an external electric field. Only an electric field with a component perpendicular to the interface can induce a surface charge density; only p-polarized light has a perpendicular

electric field component. This means that a p-polarized incoming light is required for applications involving SPs excitations at the planar metal-dielectric interface.

A.1.3 Surface Plasmon properties

With SPs, a number of specific properties are associated that are particularly relevant to sensor applications: the field enhancement, the phase jump of the reflected field upon SP excitation and the SP coherence length.

Field enhancement. A calculation of the electric field transmission coefficient on the basis of Fresnel's equation for the interface reveals that the electric field at the low index side of the metal can be much larger than that at the other side of the metal layer.

In Fig. A.3, the intensity enhancement is depicted as a function of the angle of incidence of incoming light for a number of different thickness of a gold layer. It is found that very close to the SPR angle the intensity can be enhanced by a factor of more than 30. This circumstance accounts for much of the remarkable sensitivity that the SPR condition has for a changing dielectric environment.

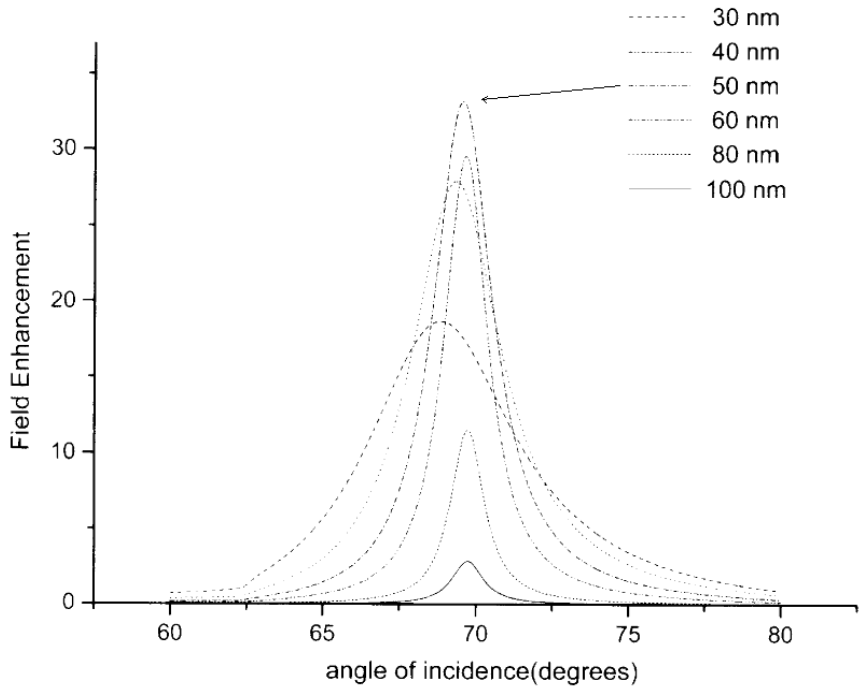

Fig. A.3. Field enhancement for various values of the thickness of the gold layer. Wavelength of the excitation light is 700 nm; the low-index side of the metal layer consist of water ($\varepsilon_3 = 1.77$).

Phase jump. As already expressed in equation (A.1) a reflection event at an interface is generally accompanied by a phase jump of the reflected field. This is illustrated in Fig.

A.4a for a prism-gold-water system. For comparison the "conventional" SPR dip is shown in Fig. A.4b for the same layer system.

We see that around the SPR dip the phase of the reflected electric field undergoes a relatively large change. The significance of this phenomenon for sensing purposes is more clear when we plot the reflectance and phase changes as a function of incident angle for a certain change in dielectric constant of the water. This is depicted in Fig. A.4c and A.4d. In the following rough calculation, we assume that both the change in reflection coefficient ΔR and the phase change $\Delta\varphi$ are proportional to $\Delta\varepsilon$. From Fig. A.4d we estimate that $\Delta R/\Delta\varepsilon \sim 30$, whereas from Fig. A.4.c we find that $\Delta\varphi/\Delta\varepsilon \sim 250$. Experimentally, a minimum $\Delta R \sim 10^{-3}$ can be measured, whereas minimum $\Delta\varphi \sim 10^{-3}$ is feasible, using interferometric techniques.

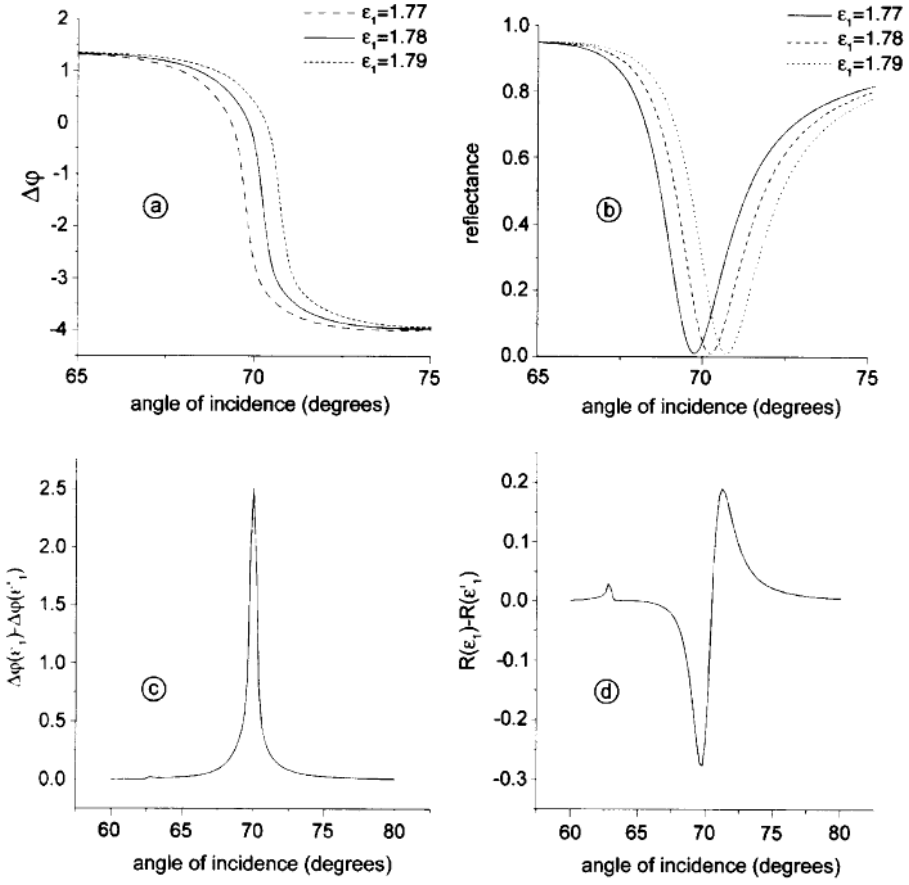

Fig. A.4. Comparison of angle-dependent phase vchanges (a, c) and reflectance changes (b, d) for variation of the dielectric constant at the low-index side of the metal layer. A gold layer is used. SPs are exited at λ=700 nm. (c) and (d) depict the differential phase and reflectance, respectively, for a change in the medium dielectric constant of 0.01.

The conclusion is that on the basis of reflectance measurements a minimum $\Delta\varepsilon \sim 4\cdot 10^{-5}$ can be detected, whereas a phase measurement provides a sensitivity of $\Delta\varepsilon \sim 4\cdot 10^{-6}$. In view of the very approximate character of this calculation, the absolute values found are of limited

validity; however, the finding that a phase measurement provides an order of magnitude better sensitivity is a hard conclusion and, indeed, this was demonstrated by Nikitin and co-worker (Kabashin and Nikitin, 1998; Grigorenko et al., 1999). The only drawback of this approach seems to be much more complicated experimental setup.

SP coherence length. Generally, the metal's dielectric constant ε_2 is complex and this circumstance results in a complex propagation constant $k_x=k_x^{'} + jk_x^{''}$. For a surface plasmon, traveling along the interface with wavevector k_x, this implies that the field intensity decays with a characteristic distance $1/2k_x''$. For gold and silver, the standard metals in sensor applications, the imaginary part of the dielectric constant increases with decreasing wavelength and the SP propagation length decreases accordingly. Both this model and the experiments indicate that a Plasmon needs roughly four times the propagation length L_x for a full decay or for a full build-up; this propagation length can be loosely defined as:

$$L_x = \frac{1}{2k_x^{''}} \tag{A.7}$$

This implies that SPs with mutual distances significantly larger than L_x are independent. This is a very important conclusion because it is the fundament of surface Plasmon microscopy (Yeatman and Ash, 1987; Rothenhausler and Knoll, 1988) with its many applications in SPR imaging and SPR multisensing: on a substrate we can define areas that in an SPR experiment will behave mutually independently, provided that these areas are significantly larger than L_x^2. For SPs on gold, excited at 632 nm, L_x ~7 µm and on a total sensor area of 1 cm^2 more than 10^4 independent sensor "patches" that each have an area of somewhat smaller than 100x100 μm^2 can in principle be defined, of which the optical responses can be simultaneously read out by using an imaging system.

A.1.4 Choice of experimental parameters

It is impossible to define a general set of optimum SPR parameters, for instance, optimal spatial resolution in an SPR microscopy/imaging setup requires values of the experimental parameters other than those to obtain maximum sensitivity for dielectric changes. Therefore, this section provides only some general guidelines, based on consideration of the properties of the metal layer. To obtain maximum sensitivity, it is advantageous to maximize the steepness of the reflectance as a function of the angle of incidence, because this allows for a more accurate determination of the angle of minimum reflectance (Fig. A.5). This implies optimization of the reflectance minimum R_{min} and minimizing the width

of the resonance curve. R_{min} can be made very close to zero by selecting the appropriate thickness of the metal layer; as can be seen in Fig. A.5, optimum thickness are somewhat dependent on the applied wavelength and are between 40 and 50 nm. The width of the resonance curve is mainly determined by the complex value of the metal's dielectric constant.

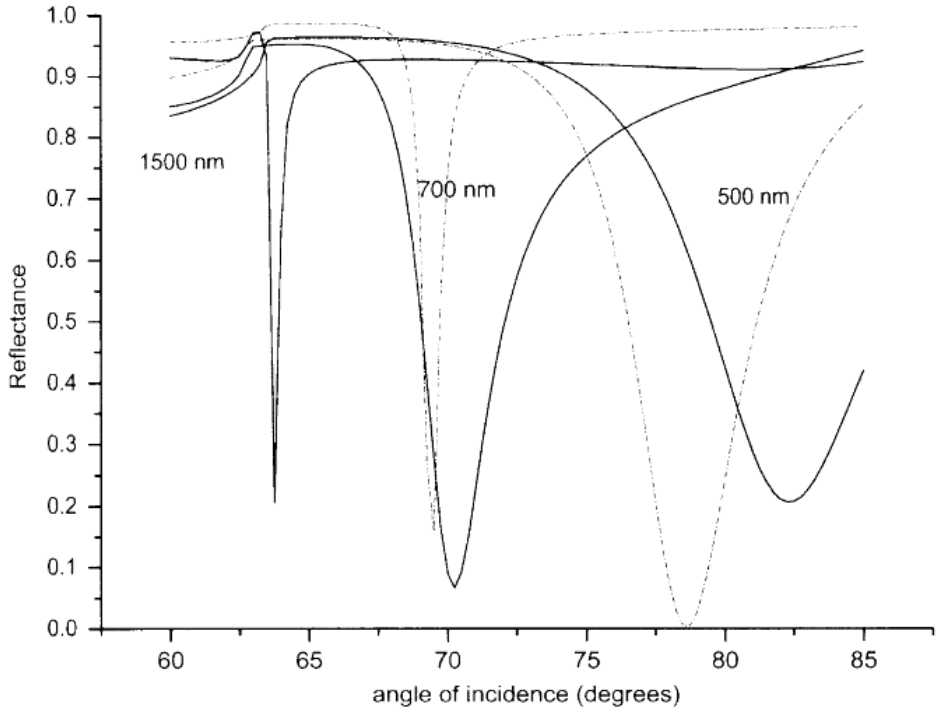

Fig. A.5. The SPR "dip" for 46 nm of silver (dashed) and gold (solid) with water on the low-index side, for several excitation wavelengths.

Generally, a large (negative) real part, together with a small imaginary part, results in a narrow resonance curves. In practice only two options are available for the choice of the metal layer: gold or silver. As seen in Fig. A.5, silver has the better SPR characteristics in view of the larger real part of its dielectric constant; however, it is chemically less inert. In Fig. A.5, it is also seen that the use of higher excitation wavelengths has an appreciable effect on the width of the resonance curve. This is one of the reasons why (near-) infrared SPR experiments are attracting attention (Tiefentahler and Lukosz, 1989; Patskovsky et al., 2003). However, it should be realized that narrowing the reflectance curve necessarily implies increasing the SPR propagation length which can be a disadvantage in certain SPR imaging applications. For a gold layer, it can be calculated that an increase in wavelength from 450 to 1500 nm results in a change in the propagation length from 100 µm to almost 1 mm. Finally, it should be mentioned that an increase in wavelength results in an increase in the penetration depth $1/k_Y$, with the consequence that the reflectance minimum will

become more sensitive to dielectric changes relatively far from the metal/dielectric interface; hence the surface sensitive character of SPR becomes less prominent. This implies that for detection of the growth of thin layers the optimum choice of wavelengths will be different from that in a situation where a more bulk-like change in refractive index has to be detected (Johansen et al., 2000).

A.1.5 Enhancement of fluorescence and absorbance

Up to now we have only considered, apart from the metal layer, transparent layers, i.e. layers that are characterized by a positive, real dielectric constant. When one or more layers contain a light-absorbing compound, SPs can boost the fluorescence intensity from a thin layer more than 40-fold (Liebermann and Knoll, 2000). This effect is due solely to the large field enhancement that occurs on the low index side of the metal layer when an SP resonance condition is established (Fig. A.3). Another, more suitable, feature of the interaction between SPs and light-absorbing molecules is the increased sensitivity for the detection of absorbances in thin layers. The addition of a light-absorbing layer results in two effects on the SPR angular-dependent curve: (1) the SPR dip shifts to a larger angle of incidence and (2) the value of the reflectance minimum increases. This last effect can readily be understood as light absorption necessarily results in a decreased reflectance. In addition, the SPR field enhancement on the low-index side of the metal layer will result in increased sensitivity for dielectric changes (Kogelnik, 1975) and therefore also for changes in the absorbance. The first effect is a consequence of the Kramers-Kronig relation (Ditchburn, 1963), which in the present context can be expressed as the statement that any change in the imaginary part of the dielectric constant will be accompanied by a change in the real part; in SPR it is mainly the real part of the dielectric profile on top of the metal layer that determines the angular position of the SPR dip. It has been demonstrated (Wang et al., 2001) that an SPR-assisted monolayer absorbance measurement can result in a 40-fold reflectance increase as compared with a metal-lacking ATR system. In addition, it is possible to extract unambiguously the thickness and the dielectric constant of an absorbing layer from a single SPR experiment (Vukusic et al., 1992).

A.2 SPR and metal nanoparticles

SPR phenomena are not restricted to planar multilayers as discussed so far; it turns out that for metal particles with dimensions much smaller than the wavelength of the interacting light, SP effects can be much more prominent. Generally, the net electric field E_{tot} around a

dielectric particle is composed of the superposition of an external applied field E_0 and the induced (dipole) field in the particle. For a polarizable spherical particle with radius r_m and dielectric constant ε, placed in a medium with dielectric constant ε_1, the following expression is found (Reitz, 1993) for the field gain G:

$$G(\omega) = \frac{E_{tot}(\omega)}{E_0(\omega)} \approx 1 + \frac{\varepsilon(\omega) - \varepsilon_1}{\varepsilon(\omega) + 2\varepsilon_1} \left(\frac{r_m}{r + r_m} \right)^3 \tag{A.8}$$

It is seen that G can reach enormous values for ε closet to -2ε_1; in a "normal" dielectric medium where ε_1>0, this condition points to the use of a metal, where ε can be negative; additionally, the imaginary part of ε should be as small as possible. It turns out that this condition corresponds to the excitation of a surface Plasmon in the metallic nanoparticles (Kreibig and Vollmer, 1995). Particularly in the field of Raman spectroscopy this can result in enormous sensitivity enhancements[1] (Kneipp et al., 2002).

A.2.1 Raman and SERS spectroscopy

One must understand the principles of the Raman spectroscopy before the comprehension of SERS principles.

Since its discovery in 1928 by Sir. C. V. Raman (Raman, 1928), Raman spectroscopy has been a very powerful characterization tool in a variety of fields such as materials science, biology, chemistry, physics and forensic science. The Raman effect results from the interaction of vibrational motions of molecules with an electromagnetic wave, providing unique spectral fingerprint of vibrations in the molecules. When a sample is irradiated with an intense beam of light, two types of scattering are observed: (a) Rayleigh scattering and (b) Raman scattering. Rayleigh scattering is intense and has the same frequency as the incident beam, whereas Raman scattering is very weak and has the frequency shifted from the incident frequency. Raman scattering can be explained by using the classical theory for the interaction of the molecule with electromagnetic radiation or by the quantum theory which relates scattering frequencies and intensities to the vibrational and the electronic energy states of the molecule.

In the classical theory, the interaction of the molecule with electromagnetic radiation gives rise to infrared absorption and Raman scattering. The interpretation of the optical response

[1] Conventional Raman spectroscopy suffers from a very low scattering efficiency which can be 12 orders of magnitude lower than that of fluorescence.

mentioned can be explained by using the basic models of the rigid rotator and harmonic oscillator in Herzberg's book (Herzberg, 1945). Electromagnetic radiation with an oscillating electric field can induce a change in the dipole moment of the molecule. The induced polarization μ is proportional to the strength of the electric field, E, as given in the equation:

$$\mu = \alpha \cdot E \tag{A.9}$$

where the proportionality, α, corresponds to the polarizability of the molecule. The polarizability reflects the ease to distort the electron cloud of a molecule susceptible to an electromagnetic radiation. The electromagnetic radiation can be simply described by the following equation:

$$E = E_0 \cos(2\pi \upsilon_l t) \tag{A.10}$$

where E_0 is the electric field strength and ν_l, is the radiation frequency. Molecular vibrations compose of normal modes, Q_j expressed as

$$Q_j = Q_{j0} \cos(2\pi \upsilon_j t) \tag{A.11}$$

where Q_{j0} is normal coordinate amplitude and ν_j is the angular frequency of molecular vibrational mode j. During the molecular vibration, the polarizability varies with the conformation if the molecule and the amplitude of the polarizability can be summed with all the possible vibration modes as

$$\alpha = \alpha_o + \left[\frac{\partial \alpha}{\partial Q_j}\right] \cdot Q_j + ... \tag{A.12}$$

When a molecule interacts with the electromagnetic field of the radiation, equation (A.9) becomes

$$\mu = \alpha \cdot E = \alpha \cdot E_0 \cos(2\pi \nu_l t) \tag{A.13}$$

Substituting equation (A.11) and (A.12) into (A.13) the induced dipole expression is derived as

$$\mu = \alpha_0 \cdot E_0 \cos(2\pi \nu_l t) + \frac{1}{2}\left[\frac{\partial \alpha}{\partial Q_j}\right] \cdot E_0 Q_{j0} \cos 2\pi(\nu_l + \nu_j)t + \frac{1}{2}\left[\frac{\partial \alpha}{\partial Q_j}\right] \cdot E_0 Q_{j0} \cos 2\pi(\nu_l - \nu_j)t + ... \tag{A.14}$$

The first term in the equation (A.14) will account for the Rayleigh scattering. The second and third terms in the equation (A.14) consist of a frequency shift due to the molecular vibration and they are called anti-Stokes scattering and Stokes scattering respectively.

The quantum theory of Raman spectroscopy is depicted by Fig. A.6. When a molecule in a low quantized energy state absorbs the energy from the radiation and is excited to a higher quantized state, the excited molecule decays back to an alternate lower state by re-emitting

the light having a frequency different from the incident light. If the re-emitted frequency is lower than the radiation frequency, this refers to Stokes scattering shown in Fig. A.6a and vice versa for anti-Stokes scattering in Fig. A.6b.

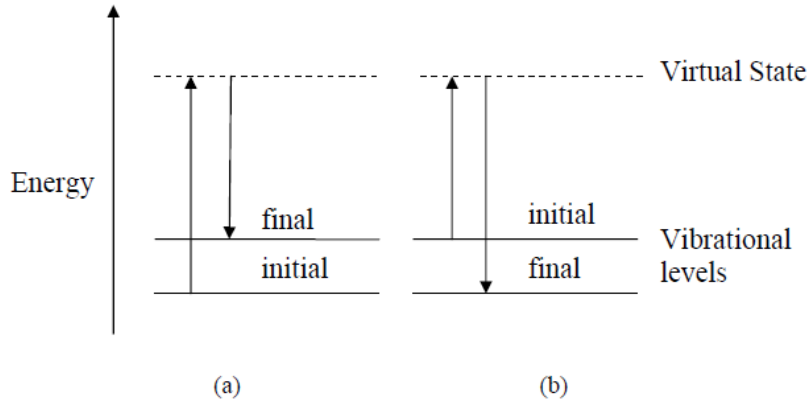

Fig. A.6. Quantum theory for (a) the Stokes and (b) anti-Stokes scattering. The arrow lines indicate the electron transition.

Since most of the molecules under standard conditions are in the lowest-lying quantized energy state, the Stokes scattering occurs more frequently than the anti-Stokes scattering. As a result, the intensity of Stokes signals is always higher than the anti-Stokes scattering. The Stokes signals are most often used for measuring Raman shift and it has a unit of cm^{-1}. The Stokes intensity for a particular mode is proportional to the fourth order of radiation frequency and is a function of polarizability shown as equation (A.15).

$$I_{Stokes} \cong (\nu_l - \nu_j)^4 \left[\frac{\partial \alpha}{\partial Q_j}\right]^2 \cdot I_0 \qquad \text{(A.15)}$$

The equation shows that higher Raman signal can be produced from higher radiation frequency and larger change in the polarizability.

The polarizability of the molecule depends on the vibration mode of different molecular bonds and the surface plasmon assisted enhancement. The Raman signals from a highly polar moiety, such as the O-H bonds in water, are usually weak. An external electric field cannot induce a large change in the polarizability of the O-H bond. Therefore, Raman spectroscopy is insensitive to water, herein makes Raman spectroscopy or SERS an excellent fingerprinting technique for the unknown in an aqueous solution. Strong Raman scattering is often observed from the moieties with distributed electron clouds, such as carbon-carbon double bonds due to the fact that the π-electron cloud of the double bond can be easily distorted through bending or stretching mode by the electric field of radiation.

Now consider a Raman-active molecule near a metal nanoparticles. The detected Raman intensity I(ω, ω_{sc}) can be expressed as

$$I_{Raman}(\omega,\omega_{sc}) = \gamma E_{exc}^2 * E_{sc}^2 = \gamma G^2(\omega) G^2(\omega_{sc}) I_0(\omega) I_{0,sc}(\omega_{sc}) \quad \text{(A.16)}$$

where E_{exc} is the total excitation electric field to which the molecule is exposed and E_{sc} is the total Raman-scattered field. The constant γ is an experimental constant that is unimportant in the present discussion. By choosing an angular frequency ω that excites surface plasmons in the metal (usually gold or silver) and detecting scattering frequencies ω_{sc} not too far from the excitation frequency, both the excitation and the scattered field are enhanced by the presence of the metal particle, this phenomenon is called Surface-Enhanced Raman Spectroscopy. It has been found experimentally that a SERS experiment can result in experimental Raman signals that are enhanced 10^{12}-10^{14} times compared with those obtained from non-surface-enhanced experiments. By substituting equation (A.8) into equation (A.16), we see that the distance dependence of the net Raman scattering intensity changes with the power -12 of the molecule-nanoparticle distance.

It should be added that apart from this SPR enhancement mechanism, another chemical enhancement effect is operational, which accounts for a 10-100-fold amplification of the bare Raman signal (Nie and Emory, 1997; Lombardi and Birke, 2008). It has been demonstrated (Kneipp et al., 1997; Bizzarri and Cannistraro, 2005) that SERS is able to detect single molecules. Together with its very high molecular specificity, this offers great promise as a detection tool for very low concentrations of biomolecules, such as DNA strands or proteins. In principle, these fields enhancements should also be important in the detection of fluorescent molecules near a metal nanoparticles. However, the nearby presence of a metal layer leads to additional non-radiative decay paths of the electronic excited states of a nearby molecule, with the net result that in many cases the fluorescence will be largely quenched. So far, metal nanoparticles were considered as surface Plasmon-assisted field amplifiers.

A.2.2 Detection based on SERS

As noted before, complex molecules exhibit many vibrational modes which can be readily identified by the pattern or "fingerprint" created by the corresponding Raman peaks. As such, there are many uses for micro-Raman spectrometers, including SERS investigation, as they can non-destructively identify microscopic samples or microscopic areas of larger

samples, providing an enormous enhancement of the Raman cross-section of molecules and moreover offering the possibility of studying the topology of complex system due to the short range character of the Raman enhancement.

The research directions for improvement of bio-sensing methods require reduction or elimination of sample preparation or amplification procedures. Detection and discrimination of specimens in complex biological media are also a necessity, together with reproducible results, cost and time effectiveness, and ease of use under most conditions.

For this reason, SERS has emerged as a powerful analytical tool that extends the possibilities of Raman vibrational spectroscopy to overcome some of these limitations. Indeed, because of its ability to solve a vast array of chemical and biochemical problems has been exploited to a wide variety of analytical applications, including life sciences (Carey, 1982), including our proposed SERS based bio-sensing approach, shown in Chapter 3.

Generally there are two principle SERS configurations that have been used in biosensing, intrinsic or extrinsic, as shown in Fig. A.7. In intrinsic detection (Fig. A.7 A), the analyte can be directly applied to the nanostructured surfaces and the inherent Raman spectrum of the biomolecule directly measured to identify the specimen. To allow for capture and to aid specificity of detection, antibodies, aptamers, or related molecules can be immobilized onto nanostructured surfaces as shown in Fig. A.7 B, and the Raman spectral differences before and after capture of the specimen can be used to identify the species. In extrinsic detection, a Raman reporter molecule is used to generate a signal for detection. For example, as shown in Chapter 3 Au nanoparticle may be used as the SERS-active substrate to which a Raman reporter molecule is immobilized (Fig. A.7 C) and further on decorated with capture molecules (such as antibodies).

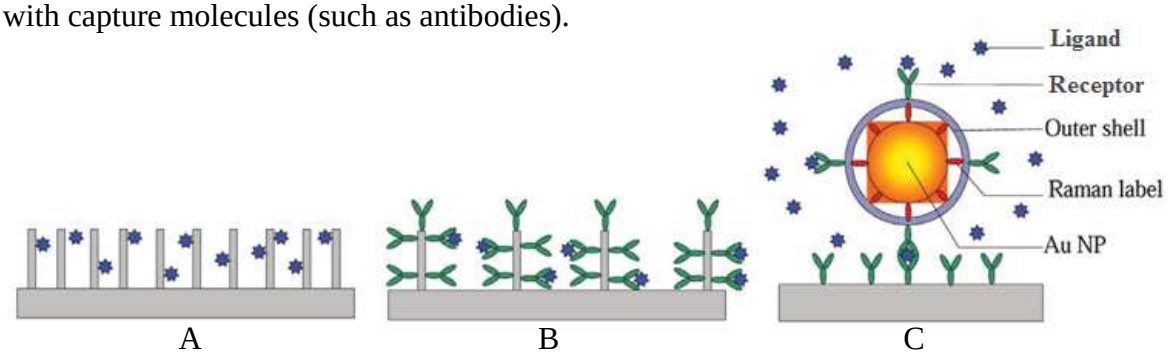

Fig. A.7. Different SERS detection configurations: (A) Direct intrinsic detection; (B) indirect intrinsic detection; and (C) extrinsic detection.

This extrinsic SERS detection method has been successfully used also for *in vivo* SERS imaging of unique or rare cancer cells (Qian et al., 2008).

The remarkable analytical sensitivity of SERS has yet to be translated into the development of widely accepted, commercially viable diagnostic applications, due in large part to the difficulty in preparing robust, metal-coated substrates of the correct surface morphology that provide maximum SERS enhancements. Some of the important requirements for an ideal SERS substrate in practical diagnostic applications are that the substrate produces a high enhancement, generates a reproducible and uniform response, has a stable shelf-life, and is simple to fabricate. Many substrate preparation techniques exist that can formroughened metal surfaces of the types required for ideal SERS enhancements. Currently, there are five fabrication techniques that could potentially produce the desired SERS substrates to meet these requirements: electron beam lithography, nanosphere lithography, the template method, the hybrid method, and an oblique angle vapor deposition method. It is worth noting that the extrinsic SERS detection method proposed in Chapter 3 provides a SERS gain factor of seven order of magnitude which is comparable with the results obtained by modern SERS substrates (Tripp et al., 2008).

A.2.3 LSPR absorbance

Nobel metal nanoparticles can also be exploited as intrinsic refractive index sensors, analogous to the more familiar planar SPR experiments (Link and El-Sayed, 1999; Haynes and Van Duyne, 2001). The physical basis of this application is the light extinction (absorption and scattering), which is heavily dependent on the nanoparticle's dielectric constant, size and geometry and also on the dielectric constant ε_1 of the surrounding medium. Mie theory gives a reasonable adequate description of the extinction coefficient A_{ext} and for spherical particles with diameter less than about 20 nm the following expression is found (Kreibig et al., 1995):

$$A_{ext} = \frac{18\pi N_p V \varepsilon_1^{\frac{3}{2}}}{\lambda} \frac{\mathrm{Im}(\varepsilon)}{[\mathrm{Re}(\varepsilon) + 2\varepsilon_1]^2 + [\mathrm{Im}(\varepsilon)]^2} \tag{A.17}$$

where N_p is the number of nanoparticles, each of which has a volume V, and λ is the wavelength of the applied light. Again we see the pronounced influence of the occurrence

of SPs: at $\mathrm{Re}(\varepsilon) = -2\varepsilon_1$ we found a maximum in the extinction coefficient, which can reach large values for low values of $\mathrm{Im}(\varepsilon)$. Hence also in this situation we are led to the use of gold or silver as a metal nanoparticle. More sophisticated models also account for the size and shape of the nanoparticles and computer programs are available in the public domain that can predict the extinction spectrum of nanoparticles of any shape (Schultz et al., 2000), by modeling the particle as a series of dipoles placed in an oscillating electric field. However, the main features of nanoparticle extinction remain contained in equation (A.17). For one nanoparticle with a diameter around 25 nm, excited close to its SP resonance, equation (A.17) results in A_{ext} of the order of 10^{-16} m^2, which corresponds to the more familiar molar extinction coefficient in the order of 10^9 1 $mol^{-1}cm^{-1}$. This value, which indeed was observed experimentally, is more than three orders of magnitude larger than that of strong light-absorbing organic dye molecules, allowing for relatively simple optical detection and characterization of individual nanoparticles (Johansen et al., 2000; Haes et al., 2004). In another series of experiments, the shift of the extinction maximum as a function of the refractive index of the surrounding medium was investigated (Link and El-Sayed, 1999). It was found experimentally that for silver nanoparticles the spectrum could shift as much as 20 nm for a change of 0.1 in the refractive index. Because molecules that adsorb to a nanoparticle change the refractive index around the particle, it is obvious that this, analogous to conventional SP resonance, can be used as a sensor principle. Indeed, it has been demonstrated experimentally that the full coverage of a silver nanoparticle with low molecular mass molecules resulted in a spectrum shift of approximately 40 nm. The full coverage correspond to only 4 x 10^4 molecules. Together with the single particle detection capability, this promises enormous sensitivity, allowing for near single molecule detection (Johansen et al., 2000).

A.3 Conclusions

The phenomenon of SPR is one of the many examples where an interesting physical phenomenon leads to applications that are highly important to both applied science and society. In a planar SPR system, it is particularly the combination of field enhancement and relatively short coherence length that allows for a unique sensor concept that provides both multiplexing capabilities and very high sensitivity. The general physical picture is well understood; however, some areas are still in vivid scientific debate (SERS, optics of nanoparticles). From a technological point of view, the emerging field of nanotechnology

will enable us to exploit to its full potential the SP phenomena of tailored nanoparticles. We believe that merging of bio-nano-technology and SP phenomena of nanoparticles will ultimately lead to sensor concepts and sensor realizations that will be important in numerous aspects of society, varying from food safety monitoring and high-throughput screening to early in vivo detection of tumor growth.

APPENDIX B

Principles of atomic force microscopy

B.1 Introduction

The resolution power, *R*, of a classical optical microscope is limited by the wavelength λ of the radiation used, according to the Rayleigh principle, as follows:

$$R = 0.61 * \left(\frac{\lambda}{\eta \sin \alpha} \right) \quad \text{(B.1)}$$

Where $\eta \sin \alpha$ is the numerical aperture.

For an optical microscope exploiting a radiation in the visible range (between about 400 and 700 nm), the resolution power will be of 200-300 nm, thus allowing the observation, for instance, of entire cells within a tissue or bacteria.

The electron microscope allows to overcome the limits of an optical microscope, by using the De Broglie wavelength of electrons accelerated by a voltage. In this case, the resolution power is extremely increased (until about 10 nm). Thus an electron microscope allows to observe viruses or sub-cellular compartments and structures (such as ribosomes or nuclear pores and gap-junctions).

The so called “scanning probe microscopies” or SPMs, on the contrary, exploits an innovative principle of microscopy: images of a surface are obtained by measuring changes in a quantity which relates to the magnitude of the interaction between a sharp probe and the specimen surface, as it is scanned beneath the probe. The kind of interaction monitored by a scanning probe microscope can differ among different techniques, but it is always strongly dependent on the probe/surface distance. Moreover, all SPMs are characterized by a feed-back loop, that regulates a quantity that is in relationship with the probe/sample interaction (to maintain this quantity at a constant value) through piezoelectric scanners, whose improvement has allowed the development of SPMs. Thus, the resolution of SPMs will depend on physical parameters, such as the probe sharpness and the accuracy with which the sample is positioned and moved in relation to the probe, through piezoelectric elements and reaches the atomic resolution (0.1 nm). SPMs began in the early 1980s when Binnig and Rohrer (Nobel prizes in Physics in 1986) invented the scanning tunnelling microscope. It is based on the measurements of a small electric current (Pa) between a tip and a surface (the two metal electrodes, separated by a distance called “vacuum gap”) in the presence of an applied voltage. The existence of this current relates to the “tunnel

effect": according to quantum mechanics, there is some probability that electrons penetrate the potential barrier represented by the vacuum gap, thus operating a flow of charges, called tunnelling current. This tunnelling current varies of one order of magnitude per angstrom of distance and hence it provides an extremely sensitive method to detect minute displacements on the pit. A few years later, Binnig and colleagues announced the birth of the second member of the SPMs family, the Atomic Force Microscope (AFM) (Binnig and Quate, 1986). AFM is probably one of the easiest forms of microscopy to understand at a basic level. All notions of the conventional microscopy, however, need to be disregarded with respect to AFM principles: AFM, in fact, images a sample by "feeling" rather than by "looking" it. It acquires topographic images by methodically scanning the specimen with a flexible probe that bends under the influence of inter-atomic probe-sample forces, according to the contours of the surface. More specifically in such a microscope (see also paragraph 2.4.3), the probe/sample interaction is based on attractive or repulsive inter-atomic forces ($10^{-12}/10^{-9}$ Newton), that are able to bend the probe (consisting of a tip mounted at the end of a lever, called cantilever) during the scan over the surface. By following how the intensity of this inter-atomic forces change while scanning the surface, the topography of a surface can be determined.

The enormous attractive potential of the atomic force microscope for biophysicists and biologists (Alessandrini et al., 2005) consists in the ability to operate in fluid conditions. This allow to image, without preliminary staining or labelling steps, a variety of biological samples (ranging in size from individual molecules to entire cells or tissue portions) at high-resolution under native conditions, and to visualise in real time molecular processes with non-destructive methods.

B.2 Probe-sample interactions

The probe/sample interaction that characterizes atomic force microscopy (AFM) measurements is due to the contribution of different types of inter-atomic forces, discussed in the following.

B.2.1 Van der Waals forces

They are the main inter-atomic forces and imply interactions between permanent dipoles, induced dipoles and asymmetrical distributions of electric charges, due to instantaneous fluctuations of electrons. Although often masked by stronger electrostatic forces, they become predominant at distances of few nanometres, as in AFM measurements. The

behaviour of van der Waals interactions can be analytically described in terms of the Lennard-Jones function, that provides the mathematical expression of the pair potential energy, $E^{pair}(r)$, as a function of the distance, as follows:

$$E^{pair}(r) = 4\varepsilon\left[\left(\sigma/r\right)^{12} - \left(\sigma/r\right)^{6}\right] \tag{B.2}$$

where ε and σ are constants depending on the material properties, r is the physical separation between the interacting pair. Fig. B.1 graphically shows the force vs. distance curve, whose trend results from Lennard-Jones potential. The $1/r^6$ term, dominating at larger distance, represents the attractive contribution.

The term $1/r^{12}$, instead, constitutes the repulsive contribution that dominates at shorter distances (unit of angstrom). The physical origin of this repulsion relates to Pauli exclusion principle and takes place when the electronic clouds, surrounding the atoms, begin to overlap.

B.2.2 Electrostatic forces

They are attractive or repulsive interactions between charged particles, that follow Coulomb force law, that defines the force acting between two charges, Fc, by the following expression:

$$Fc = \left(1/4\pi\varepsilon\right) * \left[\left(q_1 q_2\right)/r^2\right] \tag{B.3}$$

where ε is the permittivity of dielectric space, q_1 and q_2 are the charge values, r is the distance between them.

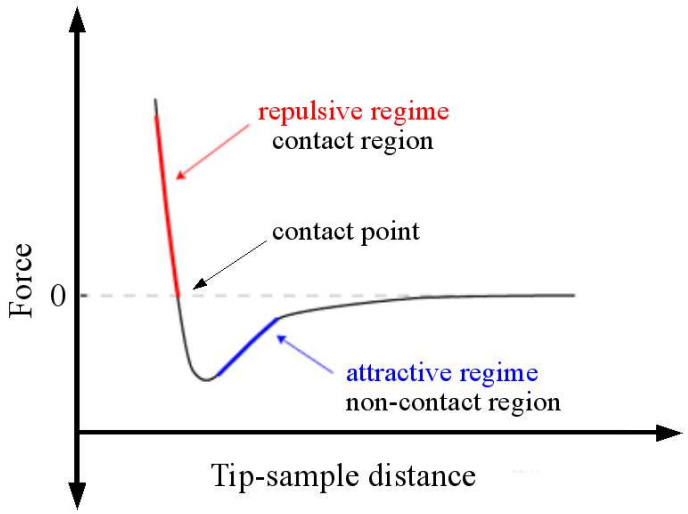

Fig. B.1. Force experienced by the cantilever as a function of the tip-sample distance.

B.2.3 Capillary and adhesive forces

When imaging in air, a thin layer of water can often condense at the sample surface. It pulls down the tip toward the surface, generating the so called "capillarity force", that can entrap the tip, causing distortion-effects and artefacts. Excessive capillarity forces can be avoided by working in fluid condition.

B.2.4 The cantilever-tip probe

By considering the cantilever as an elastic spring governed by the Hook law, its spring constant, *k*, represents the constant of proportionality between the force contribution from the bending of the cantilever *F* and its displacements *x*, as follows:

$$F = -k * x \tag{B.4}$$

k is general strongly dependent on the geometry of the spring itself and on the material, of which it is made of. The resonant frequency f_0 of the cantilever represents its natural mode of vibration. It is given by the expression:

$$f_0 = \left(k \diagup m\right)^{1/2} \tag{B.5}$$

where *k* is the cantilever spring constant and *m* its mass.

The quality factor *Q* is a parameter of particular interest in presence of a vibrating motion of the cantilever (such as in vibrating imaging modes mentioned in paragraph B.3.2). It is generally defined as the ratio between the stored vibration energy and the dissipated energy during a period of vibration. It is considered, in fact, as an indicator of the goodness of the oscillator. The most practical way to experimentally define it is given by:

$$Q = f_0 \diagup \Delta f \tag{B.6}$$

Where Δf is the width at half height of the resonance peak. The tip is generally characterized by its shape and apical radius of curvature (about 1-30 nm). Both these properties influence the resolution. In particular, when topographical elements are comparable in size with the tip, the correspondent image is a "combination" of the tip shape and the sample topography.

B.3 Imaging modes

Various AFM imaging modes have been developed to investigate samples with different properties and features. Each mode is characterized by a particular regime of the inter-

atomic forces (see Fig. B.1) and possesses typical advantage. All the imaging modes below described can be performed under air or liquid conditions.

B.3.1 Contact mode

In this imaging mode, the AFM tip is brought into direct contact with the surface of the sample and the scan is made in a repulsive regime of probe-sample forces. This mode is particularly suitable for hard samples that are not distorted by the significant lateral forces. The set-point, the parameter under the control of the feedback-loop, is the probe-sample that is kept at a constant value, by regulating the tip-sample distance during the scan. However, by excluding the feed-back controller, the distance itself can be kept at a constant value: in this case the cantilever deflection is directly recorded to image the topography. Contact mode under liquid conditions allows eliminating capillary forces, thus allowing a greater precision of the applied forces.

Contact mode can be exploited for frictional force imaging, as well: the twisting behaviour of the cantilever under the effect of lateral forces changes the path of the reflected laser beam along the horizontal direction of the photo detector face. These lateral deflections provide information on frictional or viscoelastic components of the sample.

B.3.2 Vibrating modes

The cantilever is put in vibration, at a frequency close to its own resonant frequency, by an internal oscillator during its scan across the sample surface. The set-point is the amplitude of the cantilever oscillation, that is kept constant through the feed-back controller, by changing the probe-sample distance.

Alternatively, by excluding the feed-back, the distance can be maintained at a fixed value: hence, changes of the cantilever deflection, due to changes in its amplitude oscillation, are directly recorded to determine the sample topography.

Vibrating modes strongly reduce lateral forces and thus sample damages. They additionally allow the so called phase imaging. While scanning, the tip can strike the sample and transfer a part of its energy to it, in dependence of the elastic nature of the sample itself.

Hence, the cantilever oscillation phase is disturbed and it is no longer precisely in step with the phase of the internal oscillator, that drives it. This phase shift is the recorded. Going beyond the tomographical aspect, the phase imaging informs about variations in composition, adhesion, friction and viscoelastic properties of the sample. Sample

components with sufficiently different elastic features and non-contact represent the two main vibrating modes.

In tapping mode (TM-AFM), the cantilever vibrates over the surface, by coming in contact with it. During the vibration, the regime of inter-atomic forces switches between the attractive and the repulsive one.

In TM-AFM, the oscillation amplitude and frequency are typically in the range of 10-100 nm and 100-400 KHz, respectively; these values ensures that the rip does not get stuck in the thin liquid layer on the sample surface when the scan is performed in air conditions.

It is particularly suitable for soft and delicate samples, such as the biological ones, and for imaging larger areas of rough surfaces.

In non-contact mode (NC-AFM), the cantilever is vibrated near the surface of the sample with an oscillation amplitude of about 5 nm and a frequency close to 30 kHz and it never comes in contact with the surface. The probe-sample forces are characterized by an attractive regime and they are smaller and more difficult to maintain than the repulsive contact forces. For these reasons NC-AFM requires stiffer cantilevers (to better control the vibration during the scan) and is more appropriate for smooth surfaces.

B.4 AFM resolution and sensitivity

Lateral resolution (in the xy plane) is primarily a function of the radius of curvature at the end of the tip. Features on the surface of smaller radius of curvature than the tip itself will be mapped out as a replica of the tip and all the information about the surface in the region of high curvature will be lost. Vertical resolution, on the other hand, is not dependent on tip properties and it is determined by the accuracy of the vertical movement (controlled by the piezoelectric scanner of the z axis), which is generally of angstrom order.

AFM sensitivity is in relation with the intrinsic sensitivity of the optical system (that, in turn, is a function of power laser and cantilever size), and it is strongly influenced by the thermal noise. In general, the mechanical energy, associated with the inter-atomic forces deflecting the cantilever, has to be greater than the thermal energy, to obtain an appropriate signal/noise ratio and to distinguish the cantilever deflection due to probe-sample interactions with respect to its thermal background. For this reason, with a cantilever of spring constant k, the smallest resolvable vertical displacement Δz is approximately given by:

$$\tfrac{1}{2}k(\Delta z)^2 \approx \tfrac{1}{2}k_B T \qquad \text{(B.7)}$$

where k_B is the Boltzmann constant, T the absolute temperature. The term $\frac{1}{2}k_BT$ is in the order of $2*10^{-21}$ J at room temperature. With a cantilever with k = 1 N/m, for instance, the best vertical resolution obtainable is on the order of 0.05 nm.

B.5 Combined AFM-SPR

Although AFM is capable of imaging dynamic events on a molecular scale, it is limited in its ability to provide quantitative of such events due to factors such as scan size. And number of scans per unit time. This means that while the AFM is excellent for providing a description on a highly detailed scale it is less useful for measuring average properties of a system as a whole. On the other hand, as shown in Chapter 4, SPR is a technique which is dedicated for quantifying the dynamics of biomolecular interactions, by monitoring changes in surface refractive index over relatively large areas of a sample. Therefore the combination of AFM with SPR can result in a powerful unique method for a quantitative kinetic data on surface dynamic and the AFM provided detailed spatial information on the nature of the events which were invisible to the SPR.

B.6 Atomic force spectroscopy

Given the AFM sensitivity to weak forces ($10^{-7}\div10^{-12}$ N), its cantilever can be used as a piconewton-sensitive probe for measuring inter- and intra-molecular forces. The AFM based force spectroscopy technique (AFS) has become very diffuse in the latest years to study many different molecular properties and mechanisms, such as polymers stretching (Bizzarri and Cannistraro, 2010), cellular membranes elasticity, proteins unfolding and complex dissociations. In these cases, the tip is moved along the z direction, pulling molecules apart to stretch, unfold or separate them. To study the binding properties of two proteins, which is the case treated also in this thesis (Funari et al., 2010), one interacting partner is immobilized on a flat and rigid support, while the other one is anchored to the AFM tip. The immobilization is often achieved by means of organic spacers which covalently link proteins to tip and support. The functionalized tip is therefore repeatedly brought into contact with the sample below and retracted, performing the so-called force-distance cycles. In this way, the complex is continually formed and dissociated. The output of this process is a force-distance curve, like that shown in Fig. B.2. On the x-axis the (z) tip displacement is plotted, whereas on the y-axis the deflection of the cantilever is represented (deflection *vs* distance curve). Due to the elastic properties of the cantilever,

deflection data can be easily converted into force values, providing a force *vs* distance plot, from which the name force-distance curve (or simply force curve) originates. In the point 1 of the curve (see Fig. B.2), the tip is far from the support and thus the cantilever deflection is zero. Then the tip goes down, approaching the support in the point 2 and the cantilever deflection changes. Further pushing of the tip makes the deflection (Δd) increase, reaching a maximum value in the point 2'. After that, the tip is retracted and, when in the point 2 it loses the contact with the support, the cantilever returns to zero deflection. Further retraction of the tip stretches the linker molecules (region 3-4 of the curve) until the proteins dissociate (point 4). This is spotlighted by a pull-off jump on the retraction curve, far away from the sample surface, characterised by the deflection Δd'. Once the specific bond is broken, the deflection of the cantilever returns to zero, then retracing the approach curve until point 1. By measuring the deflection value Δd' of the pull-off jump, and multiplying it by the spring constant of the cantilever, it is possible to know the force we have applied to dissociate the complex and the possibility of extracting thermodynamics parameters from these studies is tightly dependent on the analysis of force data by means of proper theoretical models (Bizzarri and Cannistraro, 2011).

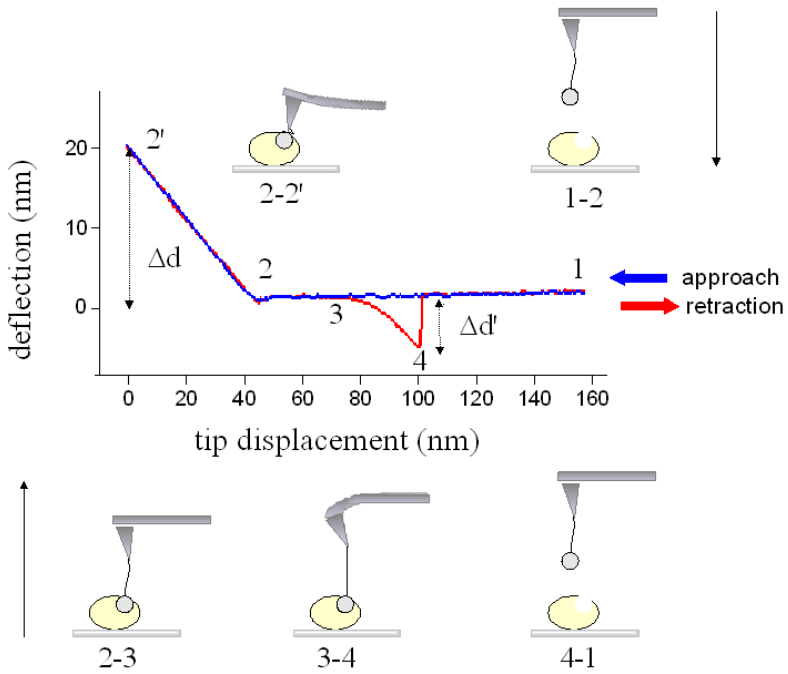

Fig B.2. Force-distance curve displaying an unbinding event. Both the approach and the retraction lines are shown. Δd and Δd' represent the cantilever deflection in the contact region and in the pull-off jump respectively. Sketches represent the various positions of the cantilever with respect to the support, during the approach (up) and the retraction (down), corresponding to the different regions of the curve (1-2; 2-2'; 2-3; 3-4; 4-1).

References

- Adman ET.**1991**. Copper protein structures. *Adv. Protein Chem.* 42, 145-197.
- Alessandrini A, Facci P. **2005**. AFM: a versatile tool in biophysics. *Meas. Sci. Technol.* 16, 65-92.
- Andersson K, Hämäläinen M, Malmqvist M. **1999**. Identification and optimization of regeneration conditions for affinity-based biosensor assays. A multivariate cocktail approach. *Anal. Chem.* 71, 2475-2481.
- Andolfi L, Bizzarri AR, Cannistraro S. **2006**. Assembling of redox proteins on Au (111) surfaces: a scanning probe microscopy investigation for application in bio-nanodevices. *Thin Solid Films* 515, 212-219.
- Andrikopoulos PC, McCarney KM, Armstrong DR, Littleford RE, Graham D, Smith WEA. **2006**. Density functional theory and resonance Raman study of a benzotriazole dye used in surface enhanced resonance Raman scattering. *J. Mol. Struct.* 789, 59-70.
- Ano Bom APD, Freitas MS, Moreira FS, Ferraz D, Sanches D, Gomes AMO, Valente AP, Cordeiro Y, Silva JL. **2010**. The p53 core domain is a molten globule at low pH: functional implication of a partially unfolded structure. *J. Biol. Chem.* 285, 2857-2866.
- Apiyo D, Wittung-Stafshede P. **2005**. Unique complex between bacterial azurin and tumour-suppressor protein p53. *Biochem. Biophys. Res. Commun.* 332, 965-968.
- Askari M, Alarie JP, Moreno-Bondi M, Vo-Dinh T. **2001**. Application of an antibody biochip for p53 detection and cancer diagnosis. *Biotechnol. Prog.*17, 543-552.
- Aslan K, Lakowicz JR, Geddes CD. **2005**. Plasmon light scattering in biology and medicine: new sensing approaches, visions and perspectives. *Curr. Opin. Cell Biol.* 9, 538-544.
- Baia M, Toderas F, Baia L, Popp J, Astilean S. **2006**. Probing the enhancement mechanisms of SERS with p-aminothiophenol molecules adsorbed on self-assembled gold colloidal nanoparticles. *Chem. Phys. Lett.* 422, 127-132.
- Banaszynski LA, Liu CW, Wandless TJ. **2005**. Characterization of the FKBP·Rapamycin·FRB ternary complex. *J. Am. Chem. Soc.* 127, 4715-4721.
- Bell S, Klein C, Müller L, Hansen S, Buchner J. **2002**. p53 contains large unstructured regions in its native state. *J. Mol. Biol.* 322, 917-927.

- Benini E, Costa A, Abolafio G, Silvestrini R. **1998**. p53 expression in human carcinomas: could flow cytometry be an alternative to immunohistochemistry? *J. Histochem. Cytochem.* 46, 41-47.
- Binnig G, Quate CF. **1986**. Atomic force microscope. *Phys. Rev. Lett.* 56, 930-933.
- Bizzarri AR, Andolfi L, Taranta M, Cannistraro S. **2008**. Optical and electronic coupling of the redox copper Azurin ITO-coated quartz substrate. *Biosens. Bioelectron.* 24, 204-209.
- Bizzarri AR, Cannistraro S. **2005**. Lévy Statistics of Vibrational Mode Fluctuations of Single Molecules from Surface-Enhanced Raman Scattering. *Phys. Rev. Lett.* 94, 068303-068306.
- Bizzarri AR, Cannistraro S. **2007a**. SERS detection of thrombin by protein recognition using functionalized gold nanoparticles. *Nanomed.-Nanotechnolog.* 3, 306-310.
- Bizzarri AR, Cannistraro S. **2007b**. Statistical analysis of intensity fluctuations in single molecule SERS spectra. *Phys. Chem. Chem. Phys.* 9, 5314-5319.
- Bizzarri AR, Cannistraro S. **2009** Surface-enhanced Raman spectroscopy combined with atomic force microscopy for ultrasensitive detection of thrombin. *Anal. Biochem.* 393, 149-154.
- Bizzarri AR, Cannistraro S. **2010**. The application of Atomic Force Spectroscopy to the study of biological complexes undergoing to a biorecognition process. *Chem. Soc. Rev.* (*Critical Reviews*) 39, 734-749.
- Bizzarri AR, Cannistraro S. **2011**. Free energy evaluation of the p53-Mdm2 complex from unbinding work measured by dynamic force spectroscopy. *Phys. Chem. Chem. Phys.* 13, 2738-2743.
- Boehr DD, Nussinov R, Wright PE. **2009**. The role of dynamic conformational ensembles in biomolecular recognition. *Nat. Chem. Biol.* 5, 789-796.
- Boisselier E, Astruc D. **2009**. Gold nanoparticles in nanomedicine: preparations, imaging, diagnostics, therapies and toxicity. *Chem. Soc. Rev.* 38, 1759-1782.
- Bossi G, Sacchi A. **2007**. Restoration of wild-type p53 function in human cancer: relevance for tumor therapy. *Head Neck (basic science review)* 29, 272-284.
- Bothner B, Lewis WS, DiGiammarino EL, Weber JD, Bothner SJ, Kriwacki RW. **2001**. Defining the Molecular Basis of Arf and Hdm2 Interactions. *J. Mol. Biol.* 314, 263-277.
- Campion A, Kambhampati P. **1998**. Surface enhanced Raman scattering. *Chem. Soc. Rev.* 27, 241-50.

- Cardona M. **1971**. Fresnel Reflection and Surface Plasmons. *Am. J. Phys.* 39 1277-1278.
- Carey PR. Biochemical Applications of Raman and Resonance Raman Spectroscopies, Academic Press, New York, **1982**.
- Chen H, Jiang C, Yu C, Zhang S, Liu B, Kong J. **2009**. Protein chips and nanomaterials for application in tumor marker immunoassays. *Biosens. Bioelectron.* 24, 3399-3411.
- Chi SW, Lee SH, Kim DH, Ahn MJ, Kim JS, Woo JY, Torizawa T, Kainosho M, Han KH. **2005**. Structural details on mdm2-p53 interaction. *J. Biol. Chem.* 280, 38795-38802.
- Choi JW, Oh BK, Jang YH, Kang DY. **2008**. Ultrasensitive immunoassay for prostate specific antigen using scanning tunneling microscopy-based electrical detection. *Appl. Phys. Lett.* 93, 033110 1-3.
- Chung JW, Kim SD, Bernhardt R, Pyun JC. **2005**. Application of SPR biosensor for medical diagnostics of human hepatitis B virus (hHBV). *Sensors and Actuators B* 111-112, 416-422.
- Ciapponi G, Scagliarini A, Tenca P. Guida al laboratorio di chimica organica. Edizioni Scolastiche Unicopli, **1987**.
- Cloarec J-P, Chevolot Y, Laurenceau E, Phaner-Goutorbe M, Souteyrand E. **2008**. A multidisciplinary approach for molecular diagnostics based on biosensors and microarrays. *ITBM-RBM.* 29, 105-127.
- Cooper MA. **2002**. Optical biosensors in drug discovery. *Nat. Rev. Drug Discov*. 1, 515-528.
- Cooper MA. **2003**. Label-free screening of bio-molecular interactions. *Anal. Bioanal. Chem.* 377, 834-842.
- Crass JJ, Rowe-Taitt CA, Nivens DA, Ligler FS. **1999**. Comparison of chemical cleaning methods of glass in preparation for silanizzation. *Biosens. Bioelectron.* 14, 683-688.
- Cullen DC, Brown RG, Lowe CR. **1987**. Detection of immuno-complex formation via surface plasmon resonance on gold-coated diffraction gratings. *Biosensors* 88, 211-225.
- Dahlman-Wright K, Baumann H, McEwan IJ, Almlof T, Wright AP, Gustafsson JA, Hard T. **1995**. Structural characterization of a minimal functional transactivation

domain from the human glucocorticoid receptor. *Proc. Natl. Acad. Sci. U.S.A.* 92, 1699-1703.

- Dawson R, Müller L, Dehner A, Klein C, Kessler H, Buchner J. **2003**. The N-terminal Domain of p53 is Natively Unfolded. *J. Mol. Biol.* 332, 1131-1141.
- De Grandis V, Bizzarri AR, Cannistraro S. **2007**. Docking study and free energy simulation of the complex between p53 DNA-binding domain and azurin. *J. Mol. Recognit.* 20, 215-226.
- Delfino I, Cannistraro S. **2009**. Optical investigation of the electron transfer protein azurin–gold nanoparticle system. *Biophys. Chem.* 139, 1-7.
- Ditchburn RW. Light. Blackie, London. **1963**.
- Domenici F, Frasconi M, Mazzei F, D'Orazi G, Bizzarri AR, Cannistraro S. **2011**. Azurin modulates the association of Mdm2 with p53: SPR evidence from interaction of the full-length proteins. *J. Mol. Recognit.* 24, 707-714.
- Dyson HJ, Wright PE. **2002**. Coupling of folding and binding for unstructured proteins. *Curr. Opin. Struct. Biol.* 12, 54-60.
- El-Sayed IH, Huang X, El-Sayed MA. **2005**. Surface Plasmon Resonance Scattering and Absorption of anti-EGFR Antibody Conjugated Gold Nanoparticles in Cancer Diagnostics: Applications in Oral Cancer. *Nano Lett.* 5, 829-834.
- Ferreon JC, Lee CW, Arai M, Martinez-Yamouta MA, Dyson HJ, Wright PE. **2009**. Cooperative regulation of p53 by modulation of ternary complex formation with CBP/p300 and HDM2. *Proc. Natl. Acad. Sci. U.S.A.* 106, 6591-6596.
- Freedman DA, Wu L, Levine AJ. **1999**. Functions of the Mdm2 oncoprotein. *Cell Mol. Life Sci.* 55, 96-107.
- Fuentes L, Oyola J, Fernandez M, Quinones E. **2004**. Conformational Changes in Azurin from *Pseudomona aeruginosa* Induced through Chemical and Physical Protocols. *Biophys. J.* 87, 1873-1880.
- Funari G, Domenici F, Nardinocchi L, Puca R, D'Orazi G, Bizzarri AR, Cannistraro S. **2010**. Interaction of p53 with MDM2 and Azurin as studied by Atomic Force Spectroscopy. *J. Mol. Recognit.* 23, 343-351.
- Gabellieri E, Bucciantini M, Stefani M, Cioni P. **2009**. Spectroscopic characterization of the complex between azurin and p53 transactivation domain. *Eur. Biophys. J.* 38, (suppl. 1), s161.
- Gannon JV, Greaves R, Iggo R, Lane DP. **1990**. Activating mutations in p53 produce a common conformational effect. A monoclonal antibody specific for the mutant form.

EMBO J. 9, 1595-1602.

- Giljohann DA, Mirkin CA. **2009**. Drivers of biodiagnostic development. *Nature* 462, 461-464.
- Grigorenko AN, Nikitin PI, Kabashin AV. **1999**. Phase jumps and interferometric surface plasmon resonance imaging. *Appl. Phys. Lett.* 75, 3917-3919.
- Guihong Y, Da X, Shici T, Qun C. **2004**. Rapid and sensitive immunomagnetic-electrochemiluminescent detection of p53 antibodies in human serum. *J. Immunol. Methods* 288, 47-54.
- Guzzi R, Sportelli L. **1992**. Interaction of azurin with alcohols: An ESR, optical absorption, and fluorescence emission investigation. *J. Inorg. Biochem.* 45, 39-45.
- Haes AJ, Stuart DA, Nie S, Van Duyne RP. **2004**. Using solution-phase nanoparticles, surface-confined nanoparticle arrays and single nanoparticles as biological sensing platforms. *J. Fluor*. 14, 355.
- Halliwell CM, Cass AEG. **2001**. A factorial analysis of silanization conditions for the immobilization of oligonucleotides on glass surfaces. *Anal. Chem.* 73, 2476-2483.
- Haynes CL, Van Duyne RP. **2001**. Nanosphere Lithography: A Versatile Nanofabrication Tool for Studies of Size-Dependent Nanoparticle Optics. *J. Phys. Chem. B.* 105, 5599-5611.
- Hecht E. Optics. Addison-Wesley, New York, **2002**.
- Herzberg G. Molecular Spectra and Molecular Structure. I. Infrared and Raman Spectra of Polyatomic Molecules. van Nostrand, Princeton **1945**.
- Hilser VJ. **2010**. An ensemble view of allostery. *Science* 327, 653-654.
- Hofseth LJ, Saito S, Hussain SP, Espey MG, Miranda KM, Araki Y, Jhappan C, Higashimoto Y, He P, Linke SP, Quezado MM, Zurer I, Rotter V, Appella E, Harris CC. **2002**. Nitric oxide-induced cellular stress and p53 activation in chronic inflammation. *Proc. Natl. Acad. Sci. U.S.A.*100, 143-148.
- Homola J. **2003**. Present and future of surface plasmon resonance biosensors. *Anal. Bioanal. Chem.* 377, 528-539.
- Honda R, Tanaka H, Yasuda H. **1997**. Oncoprotein Mdm2 is an ubiquitin ligase E3 for tumor suppressor p53. *FEBS Lett.* 420, 25-27.
- Houk KN, Leach AG, Kim SP, Zhang X. **2003**. Binding affinities of host-guest, protein-ligand, and protein-transition-state complexes. *Anghew Chem. Int. Ed*. 42, 4872-4897.
- Iakoucheva LM, Brown CJ, Lawson JD, Obradović Z, Dunker AK. **2002**. Intrinsic

disorder in Cell-signaling and Cancer-associated Proteins. *J. Mol. Biol.* 323, 573-584.

- Jackson JB, Halas NJ. **2004**. Surface-enhanced Raman scattering on tunable plasmonic nanoparticle substrates. *Proc. Natl. Acad. Sci. U.S.A.* 101, 17930-17935.
- Janin J. **1995**. Principles of protein-protein recognition from structure to thermodynamics. *Biochimie* 77, 497-505.
- Jia CP, Zhong XQ, Hua B, Liu MY, Jing FX, Lou XH, Yao SH, Xiang JQ, Jin QH, Zhao JL. **2009**. Nano-ELISA for highly sensitive protein detection. *Biosens. Bioelectron.* 24, 2836-2841.
- Jiao LS, Niu L, Shen J, You T, Dong S, Ivaska A. **2005**. Simple Azo derivazion on 4-aminothiophenol/ Au monolayer. *Electrochem. Commun.* 7, 219-222.
- Johansen K, Arwin H, Lundstrom I, Liedberg B. **2000**. An Imaging Surface Plasmon Resonance Sensor Based on Multiple Wavelengths: Sensitivity Considerations. *Rev. Sci. Instrum*. 71, 3530-3538.
- Kabashin AV, Nikitin PI. **1998**. Surface plasmon resonance interferometer for bio- and chemical-sensors. *Opt. Commun.* 150, 5-8.
- Kenny GE, Dunsmoor CL. **1983**. Principles, problems, and strategies in the use of antigenic mixtures for the enzyme-linked immunosorbent assay. *J. Clin. Microbiol.* 17, 655-665.
- Klein C, Vassilev LT. **2004**. Targeting the p53-MDM2 interaction to treat cancer. *Brit. J. Cancer*. 91, 1415-1419.
- Klein J. **2007**. Probing the interactions of proteins and nanoparticles. *Proc. Natl. Acad. Sci. U.S.A.* 104, 2029-2030.
- Kneipp K, Kneipp H, Itzkann I, Dasari RR, Feld MSJ. **2002**. Surface-enhanced Raman scattering and biophysics. *J. Phys.-Condens. Matter.* 14, 597-624.
- Kneipp K, Wang Y, Kneipp H, Perelman LT, Itzkan I, Dasari R, Feld MS. **1997**. Single molecule detection using surface-enhanced raman scattering (SERS). *Phys. Rev. Lett.* 78, 1668-1670.
- Kogelnik H. in "Topic in Aplied Physics" vol 7, ed. T. Tamir, Springer, Berlin, **1975**.
- Kreibig U, Vollmer M. Optical Properties of Metal Clusters. Springer. Berlin, **1995**.
- Kretschmann E, Raether HZ. **1968**. Radiative decay of nonradiative surface plasmon excited by light. *Naturforsch.* 230, 2135-2136.
- Kumar R, Thompson EB. **2003**. Transactivation functions of the N-terminal domains of nuclear hormone receptors: protein folding and coactivator interactions. *Mol. Endocrinol.* 17, 1-10.

- Kussie PH. **1996**. Structure of the Mdm2 oncoprotein bound to the p53 tumor suppressor transactivation domain. *Science* 274, 948-953.
- Lai Z, Auger KR, Manubay CM, Copeland RA. **2000**. Thermodynamics of p53 binding to hdm2 (1-126): effects of phosphorylation and p53 peptide length. *Arch. Biochem. Biophys.* 381, 278-284.
- Lavin MF, Gueven N. **2006**. The complexity of p53 stabilization and activation. *Cell. Death Diff.* 13, 941-950.
- Leckner J, Bonander N, Wittung-Stafshede P, Malmström BG, Karlsson BG. **1997**. The effect of the metal ion on the folding energetics of azurin: a comparison of the native, zinc and apoprotein. *Biochim. Biophys. Acta* 1342, 19-27.
- Legros Y, Meyer A, Oryt K, Soussi T. **1994**. Mutations in p53 produce a common conformational effect that can be detected with a pane of monoclonal antibodies directed toward the central part of the p53 protein. *Oncogene* 9, 3689-3694.
- Levesque MA, Katsaros D, Yu H, Giai M, Genta F, Roagna R, Ponzone R, Massobrio M, Sismondi P, Diamandis EP. **1998**. Immunofluorometrically determined p53 accumulation as a prognostic indicator in italian breast cancer patients. *Int. J. Cancer (Pred. Oncol.)* 79, 147-152**.**
- Li J, Wang H, Zhao Y, Cheng L, He H, Lu Z. **2001**. Assembly method fabricating linkers for covalently bonding DNA on glass surface. *Sensors* 1, 53-59.
- Li J. **1997**. Detection of ras p21 and p53 proteins in serum of the lung cancer patients exposed to indoor coal-burning pollution with western blotting. *Fuel Energy Abstr.* 38, 350-350.
- Liebermann T, Knoll W. **2000**. Surface-plasmon field-enhanced fluorescence spectroscopy. *Colloids Surf. A.* 171, 115-130.
- Link S, El-Sayed MA. **1999**. Spectral Properties and Relaxation Dynamics of Surface Plasmon Electronic Oscillations in Gold and Silver Nanodots and Nanorods *J. Phys. Chem. B.* 103, 8410-8426.
- Lombardi JR, Birke RL. **2008**. A Unified Approach to Surface-Enhanced Raman Spectroscopy. *J. Phys. Chem. C* 112, 5605-5617.
- Ma J, Martin JD, Zhang H, Auger KR, Ho TF, Kirkpatrick RB, Grooms MH, Johanson KO, Tummino PJ, Copeland RA, Lai Z. **2006**. A second p53 binding site in the central domain of Mdm2 is essential for p53 ubiquitination. *Biochemistry* 45, 9238-9245.

- Malviya V, Singh H, Usha USD, Singh PB. **2004**. Serum p53 and bladder cancer: can serum p53 be used as a tumor marker? *Urol. Res.* 32, 391-394.
- Moll UM, Petrenko O. **2003**. The MDM2-p53 interaction. *Mol. Cancer Res.* 1, 1001-1008.
- Momand J, Zanbetti GP, Olson DC, George D, Levine AJ. **1992**. The Mdm2 oncogene product forms a complex with the p53 protein and inhibits p53-mediated transactivation. *Cell* 69, 1237-1245.
- Moore MN, Simpson MG. **1992**. Molecular and cellular pathology in environmental impact assessment. *Aquat. Toxicol.* 22, 313-322.
- Morton TA, Myszka DG. **1998**. Kinetic analysis of macromolecular interactions using surface plasmon resonance biosensors. *Method. Enzymol.* 295, 268-294.
- Mukherjee JJ, Sikka HC. **2006**. Attenuation of BPDE-induced p53 accumulation by TPA is associated with a decrease in stability and phosphorylation of p53 and downregulation of NFkB activation: role of p38 MAP kinase. *Carcinogenesis* 27, 631-638.
- Myszka DG, Morton TA, Doyle ML, Chaiken IM. **1997**. Kinetic analysis of a protein antigenantibody interaction limited by mass transport on an optical biosensor. *Biophys. Chem.* 64, 127-137.
- Nel AE, Madler L, Velegol D, Xia T, Hoek EMV, Somasundaran P, Klaessig F, Castranova V, Thomson M. **2009**. Understanding biophysicochemical interactions at the nano-bio interface. *Nat. Mater.* 8, 543-557.
- Nie S, Emory SR. **1997**. Probing single molecules and single nanoparticles by surface-enhanced Raman scattering. *Science* 275, 1102-1106.
- Nooren IMA, Thornton JM. **2003**. Structural characterization and functional significance of transient protein-protein interactions. *J. Mol. Biol.* 325, 991-1018.
- Osawa M, Matsuda M, Yoshii K, Uchida I. **1994**. Charge transfer resonance Raman process in surface-enhanced Raman scattering from p-aminothiophenol adsorbed on silver: Herzberg-Teller contribution. *J. Phys. Chem.* 98, 12702-12707.
- Otto A, Mrozek I, Grabhorn H, Pommier Y. **1992**. Surface-enhanced Raman scattering. *J. Phys. Condens. Matter*. 4, 1143-1406.
- Otto A. **1968**. Excitation of nonradiative surface plasma waves in silver by the method of frustrated total reflection. *Z. Phys.-Handron. Nucl*.216, 398-410.
- Park SH, Im JH, Chun BH, Kim JH. **1999**. Adsorption kinetics of Au and Ag nanoparticles on functionalized glass surfaces. *Microchem. J.* 63, 71-91.

- Patskovsky S, Kabashin AV, Meunier M, Luong JHT. **2003**. Properties and sensing characteristics of surface-plasmon resonance in infrared light. *J. Opt. Soc. Am. A.* 20, 1644.
- Phillips JH, Robrish SA, Bates C. **1965**. High efficiency coupling of diazonium ion to proteins and amino acids. *J. Biol. Chem.* 240. 699-704.
- Polman A. **2008**. Plasmonics applied. *Science* 322, 868-869.
- Pontius BW. **1993**. Close encounters: why unstructured, polymeric domains can increase rates of specific macromolecular association. *Trends Biochem. Sci.* 18, 181-186.
- Portefaix J-M, Fanutti C, Granier C, Crapez E, Perham R, Grenier J, Pau B, Del Rio M. **2002**. Detection of anti-p53 antibodies by ELISA using p53 synthetic or phage-displayed peptides. *J. Immunol. Methods* 259, 65-75.
- Psyrri A, Kountourakis P, Yu Z, Papadimitriou C, Markakis S, Camp RL, Economopoulos T, Dimopoulos MA. **2007**. Analysis of p53 protein expression levels on ovarian cancer tissue microarray using automated quantitative analysis elucidates prognostic patient subsets. *Ann. Oncol.* 18, 709-715.
- Punj V, Bhattacharyya S, Saint-Dic D, Vasu C, Cunningham EA, Graves J, Yamada T, Constantinou AI, Christov K, White B, Li G, Majumdar D, Chakrabarty AM, Das Gupta TK. **2004**. Bacterial cupredoxin azurin as an inducer of apoptosis and regression in human breast cancer. *Oncogene* 23, 2367-78.
- Punj V, Das Gupta KT, Chakrabarty MA. **2003**. Bacterial cupredoxin azurin and its interactions with the tumour suppression protein p53. *Bioch. Bioph. Res. Commun.* 312, 109-114.
- Qian X, Peng XH, Ansari DO, Yin-Goen Q, Chen GZ, Shin DM, Yang L, Young AN, Wang MD, Nie S. **2008**. *In vivo* tumor targeting and spectroscopic detection with surface-enhanced Raman nanoparticle tags. *Nat Biotechnol.* 26, 83-90.
- Raether H. Surface Plasmons on Smooth and Rough Surfaces and on Gratings. Springer, Berlin, **1988**.
- Raman CV, Krishnan KS. **1928**. A new type of secondary radiation. *Nature* 121, 501-502.
- Reitz JR, Milford J, Christy RW. Foundations of Electromagnetic Theory. Addison Wesley, New York, **1993**.

- Robert P, Benoliel AM, Pierres A, Bongrand P. **2007**. What is the biological relevance of the specific bond properties revealed by single-molecule studies? *J. Mol. Recognit.* 20, 432-447.
- Robert P, Limozin L, Pierres A, Bongrand P. **2009**. Biomolecule association rates do not provide a complete description of bond formation. *Biophys. J.* 96, 4642-4650.
- Rössner PJr, Chvatalova I, Schmuczerova J, Milcova A, Rössner P, Sram RJ. **2004**. Comparison of p53 levels in lymphocytes and in blood plasma of nuclear power plant workers. *Mutat. Res. Fundam. Mol. Mech. Mugag.* 556, 55-63.
- Roth J, Dobbelstein M, Freedman DA, Shenk T. **1998**. Nucleo-cytoplasmic shuttling of the hdm2 oncoprotein regulates the levels of the p53 protein via a pathway used by the human immunodeficiency virus rev protein. *EMBO J.* 2, 554-564.
- Rothenhausler B, Knoll W. **1988**. Surface-plasmon microscopy. *Nature* 332, 615 617.
- Sarah LW, Steven JO, Lee TR, Halas NJ. **1999**. Construction of simple gold nanoparticle aggregates with controlled plasmon–plasmon interactions. *Chem. Phys. Lett.* 300, 651-655.
- Schon O, Friedler A, Bycroft M, Freund SMV, Fersht AR. **2002**. Molecular mechanism of the interaction between Mdm2 and p53. *J. Mol. Biol.* 323, 491-501.
- Schultz S, Smith DR, Mock JJ, Schultz DA. **2000**. Single-target molecule detection with nonbleaching multicolor optical immunolabels. *Proc. Natl. Acad. Sci. USA.* 97, 996-1001.
- Shimada H, Nakajima K, Sakamoto K, Takeda A, Hori S, Hayashi H, Kenmochi T, Gunji Y, Suzuki T, Asano T, Kashiwabara H, Yokoyama K, Arita S, Ochiai T. **2000**. Existence of Serum p53 Antibodies in Cyclosporine A-Treated Transplant Patients: Possible Detection of p53 Protein Over-Expression. *Transplant. Proc.* 32, 1779.
- Shurbaji MS, Kalbfleisch JH, Thurmond TS. **1995**. Immunohistochemical detection of p53 protein as a prognostic indicator in prostate cancer. *Hum. Patol.* 26, 106-109.
- Slistan-Grijalva A, Herrera-Urbina R, Rivas-Silva JF, Valos-Borja MA, Castillon-barraza FF, Posada-Amarillas A. **2005**. Classical theoretical characterization of the surface plasmon absorption band for silver spherical nanoparticles suspended in water and ethylene glycol. *Physica E.* 27, 104-112.
- Soper SA, Brown K, Ellington A, Frazier B, Garcia-Manero G, Gauf V, Gutmang SI, Hayes DF, Korte B, Landers JL, Larson D, Ligler F, Majumdarm A, Mascini M, Nolte D, Rosenzweig Z, Wang J, Wilson D. **2006**. Point-of-care biosensor systems for cancer diagnostics/prognostics. *Biosens. Bioelectron.* 21, 1932-1942.

- Sreerama N, Woody RW. **1994**. Protein secondary structure from circular dichroism spectroscopy. *J. Mol. Biol.* 242, 497-507.
- Stefanek ME, Andrykowski MA, Lerman C, Manne S, Glanz K. **2009**. Behavioral Oncology and the War on Cancer: Partnering with Biomedicine. *Cancer Res.* 69, 7151-7156.
- Szeghalmi A, Kaminskyj S, Rosch P, Popp J, Gough KM. **2007**. Time fluctuations and imaging in the SERS spectra of fungal hypha grown on nanostructured substrates. *J. Phys. Chem. B.* 111, 12916-12924.
- Taranta M, Bizzarri AR, Cannistraro S. **2008a**. Probing the interaction between p53 and the bacterial protein azurin by single molecule force spectroscopy. *J. Mol. Recognit.* 21, 63-70.
- Taranta M, Bizzarri AR, Cannistraro S. **2008b**. Modelling the interaction between the N terminal domain of the tumor suppressor p53 and azurin. *J. Mol. Recognit.* 22, 215-222.
- Taylor BN, Mehta RR, Yamada T, Lekmine F, Christov K, Chakrabarty AM, Green A, Bratescu L, Shilkaitis A, Beattie CW, Das Gupta TK. **2009**. Noncationic peptides obtained from azurin preferentially enter cancer cells. *Cancer Res.* 69, 537-546.
- Thomas MD, McIntosh GG, Anderson JJ, McKenna DM, Parr AH, Johnstone R, Lennard TW, Horne CH, Angus B. **1997**. A novel quantitative immunoassay system for p53 using antibodies selected for optimum designation of p53 status. *J. Clin. Pathol.* 50, 143-147.
- Tiefentahler K, Lukosz W. **1989**. Sensitivity of grating couplers as integrated-optical chemical sensors. *J. Opt. Soc. Am. B* 6, 209-220.
- Toledo F, Wahl GM. **2006**. Regulating the p53 pathway: *in vitro* hypotheses, *in vivo veritas. Nat. Rev. Cancer* 6, 909-923.
- Tripp RA, Dluhy RA, Zhao Y. **2008**. Novel nanostructures for SERS biosensing. *Nano Today* 3, 31-37.
- Uversky VN. **2002**. Natively unfolded proteins: a point where biology waits for physics. *Protein Sci.*11, 739-756.
- Van Duyne P, Haller KL, Altkorn RI. **1986**. Spatially resolved surface enhanced Raman spectroscopy: feasibility, intensity dependence on sampling area and attomole mass sensitivity. *Chem. Phys. Lett.* 126, 190-196.

- Van Emon JM, Gerlach CL, Bowman K. **1998**. Bioseparation and bioanalytical techniques in environmental monitoring. *J. Chrom. B Biomed. Sci. Appl.* 715, 211-228.
- Veprintsev DB, Freund SMV, Andreeva A, Rutledge SE, Tidow H, Cañadillas JMP, Blair CM, Fersht AR. **2006**. Core domain interactions in full-length p53 in solution. *Proc. Natl. Acad. Sci. U.S.A.* 103, 2115-2119.
- Vise PD, Baral B, Latos AJ, Daughdrill GW. **2005**. NMR chemical shift and relaxation measurements provide evidence for the coupled folding and binding of the p53 transactivation domain. *Nucleic Acid Res.* 33, 2061-2077.
- Vogelstein B, Lane D, Levine AJ. **2000**. Surfing the p53 network. *Nature* 408, 307-317.
- Vukusic PS, Sambles JR, Wright JD. **1992**. Surface plasmon resonance characterization of spin-deposited phthalocyanine films. *J. Mater. Chem.* 2, 1105-1106.
- Wang J, Kong LT, Guo Z, Xu JY, Liu JH. **2010**. Synthesis of novel decorated one-dimensional gold nanoparticle and its application in ultrasensitive detection of insecticide. *J. Mater. Chem.* 20, 5271-5279.
- Wang S, Boussaad S, Tao N. **2001**. Surface Plasmon Resonance Enhanced Optical Absorption Spectroscopy for Studying Molecular Adsorbates. *J. Rev. Sci. Instrum.* 72, 3055-3060.
- Wang Y, Zhu X, Wu M, Xia N, Wang J, Zhou F. **2009**. Simultaneous and Label-Free Determination of Wild-Type and Mutant p53 at a Single Surface Plasmon Resonance Chip Preimmobilized with Consensus DNA and Monoclonal Antibody. *Anal. Chem.* 81, 8441-8446.
- Wei A, Kim B, Sadtler B, Tripp SL. **2001**.Tunable surface-enhanced Raman scattering from large gold nanoparticles arrays. *Chemphyschem*. 12, 743-745.
- Whitmore L, Wallace BA. **2004**. DICHROWEB an online server for protein secondary structure analyses from circular dichroism spectroscopic data. *Nucleic Acid Res.* 32, 668-673.
- Wu J, Buranda T, Metzenberg RL, Sklar LA, Lopetz GP. **2006**. Diazo coupling method for covalent attachment of proteins to solid substrates. *Bioconjugate Chem.* 17, 359-365.

- Yamada T, Fialho AM, Punj V, Bratescu L, Das Gupta TK, Chakrabarty AM. **2005**. Internalization of bacterial redox protein azurin in mammalian cells: entry domain and specificity. *Cell. Microbiol.* 7, 1418-1431.
- Yamada T, Goto M, Punj V, Zaborina O, Chen ML, Kimbara K, Majumdar D, Cunningham E, Das Gupta TK, Chakrabarty AM. **2002**. Bacterial redox protein azurin, tumour suppressor protein p53, and regression of cancer. *Proc. Natl. Acad. Sci. U.S.A.* 99, 14098-14103.
- Yamada T, Hiraoka Y, Ikehata M, Kimbara K, Avner SB, Tapas KDG, Chakrabarty AM. **2004**. Apoptosis or growth arrest: modulation of tumor suppressor p53's specificity by bacterial redox protein azurin. *Proc. Natl. Acad. Sci. U.S.A.* 101, 4770-4775.
- Yamada T, Mehta RR, Lekmine F, Christov K, King ML, Majumdar D, Shilkaitis A, Green A, Bratescu L, Beattie CW, Das Gupta TK. **2009**. A peptide fragment of azurin induces a p53-mediated cell cycle arrest in human breast cancer cells. *Mol. Cancer. Ther*. 8, 2947-2958.
- Yang J, Duerksen-Hughes P. **1998**. A new approach to identifying genotoxic carcinogens: p53 induction as an indicator of genotoxic damage. *Carcinogenesis* 19, 1117-1125.
- Yeatman E, Ash E. **1987**. Surface-plasmon microscopy. *Electron. Lett.* 23, 1091-1092.
- Yeo J, Park JY, Bae WJ, Lee YS, Kim BH, Cho Y, Park SM. **2009**. Label-Free Electrochemical Detection of the p53 Core Domain Protein on Its Antibody Immobilized Electrode. *Anal. Chem.* 81, 4770-4777.
- Zhu Z, Zhu T, Liu Z. **2004**. Raman scattering enhancement contributed from individual gold nanoparticles and interparticle coupling. *Nanotechnology* 15, 357-364.
- Zusman I, Sandler B, Gurevich P, Zusman R, Smirnoff P, Tendler Y, Bass D, Shani A, Idelevich E, Pfefferman R, Davidovich B, Huszar M, Glick J. **1996**. Comparative study of the role of serum levels of p53 antigen and its tumor cell concentration in colon cancer detection. *Hum. Antibodies Hybridomas* 7, 123-128.

Acknowledgments

The last three and a half years have been a very pivotal time for me, both scientifically and personally. Many people were involved in this and I would like to thank every one of them for their friendship, help, time, guidance and understanding.

In particular I would like to thank the members of the Biophysics and Nanoscience Centre: Prof. Salvatore Cannistraro, Prof. Anna Rita Bizzarri, Dr. Ines Delfino, Dr. Chiara Baldacchini, (including the former members Dr. Laura Andolfi, Dr. Monia Taranta, Dr. Luca Pandolfi and Dr. Gloria Funari) for giving me the opportunity to conduct my research in their group; the great benefit of the support they provided me; the highly productive discussions which have helped me to become an independent scientist, giving me the opportunity to realize my own ideas.

I am very grateful for the excellent scientific environment I encountered during my time at the Tuscia University. In particular, many thanks are due to my Ph.D Coordinator Maurizio Petruccioli, the Director Silvano Onofri and his staff. I have greatly benefited for the excellent support they provided me.

Special thanks to Prof. Agostina Congiu Castellano for pursuing my scientific education and for providing me the optical equipment of the Structure of Biological Matter Laboratory, Sapienza University of Rome, thus contributing significantly to my thesis.

Express thanks go to Prof. Franco Mazzei and Dr. Marco Frasconi of the Biosensors Laboratory, Sapienza University of Rome, for their technical and scientific support concerning the SPR measurements.

Extra special thanks to Dr. Cristina Olmati for the pleasant times and innumerable hours spent on correcting and suggesting improvements.

List of publications

Publications of results presented in this work

- Funari G, Domenici F, Nardinocchi L, Puca R, D'Orazi G, Bizzarri AR, Cannistraro S. **2010**. Interaction of p53 with MDM2 and Azurin as studied by Atomic Force Spectroscopy. *J. Mol. Recognit.* 23, 343-351.

- Domenici F, Frasconi M, Mazzei F, D'Orazi G, Bizzarri AR, Cannistraro S. **2011**. Azurin modulates the association of Mdm2 with p53: SPR evidence from interaction of the full-length proteins. *J. Mol. Recognit.* 24, 707-714.

- Domenici F, Bizzarri AR, Cannistraro S. **2011**. SERS-based nanobiosensing for ultrasensitive detection of the tumour suppressor p53. (Under review).

Additional publications

- Domenici F., Castellano C., Dell'Unto F., Albinati A., Congiu A. **2011**. Silicon supported lipid-DNA thin films structure at varying temperature studied by Energy Dispersive X-ray Diffraction and Neutron Reflectivity. *Colloid Surface B* (under review).

Research Article

Journal of Molecular Recognition

Received: 23 March 2009, Revised: 3 August 2009, Accepted: 15 September 2009, Published online in Wiley InterScience: 25 November 2009

(www.interscience.wiley.com) DOI:10.1002/jmr.999

Interaction of p53 with Mdm2 and azurin as studied by atomic force spectroscopy

Gloria Funari[a], Fabio Domenici[a], Lavinia Nardinocchi[b,c], Rosa Puca[b,c], Gabriella D'Orazi[b,c], Anna Rita Bizzarri[a] and Salvatore Cannistraro[a]*

Azurin, a bacterial protein, can be internalized in cancer cells and induce apoptosis. Such anticancer effect is coupled to the formation of a complex with the tumour-suppressor p53. The mechanism by which azurin stabilizes p53 and the binding sites of their complex are still under investigation. It is also known that the predominant mechanism for p53 down-regulation implies its association to Mdm2, the main ubiquitin ligase affecting its stability. However, the p53/Mdm2 interaction, occurring at the level of both their N-terminal domains, has been characterized so far by experiments involving only partial domains of these proteins. The relevance of the p53/Mdm2 complex as a possible target of the anticancer therapies requires a deeper study of this complex as made up of the two entire proteins. Moreover, the apparent antagonist action of azurin against Mdm2, with respect of p53 regulation, might suggest the possibility that azurin binds p53 at the same site of Mdm2, preventing in such a way p53 and Mdm2 from association and thus p53 from degradation. By following the interaction of the two entire proteins by atomic force spectroscopy, we have assessed the formation of a specific complex between p53 and Mdm2. We found for it a binding strength and a dissociation rate constant typical of dynamical protein–protein interactions and we observed that azurin, even if capable to bind p53, does not compete with Mdm2 for the same binding site on p53. The formation of the p53/Mdm2/azurin ternary complex might suggest an alternative anti-cancer mechanism adopted by azurin.

Supporting information may be found in the online version of this paper.

Keywords: p53; Mdm2; azurin; force spectroscopy; molecular interaction; AFM

INTRODUCTION

p53, 'the guardian of the genome', is probably the most extensively characterized transcription factor with a tumour-suppressor activity (Oren, 2003; Harris and Levine, 2005). The human p53 protein consists of four major domains which are responsible for its transcriptional activation DNA-binding and tetramerization functions (Ko and Prives, 1996; Levine, 1997). In presence of different stress signals, p53 is stabilized through post-translational modifications (Lavin and Gueven, 2006), its cellular levels increase and it can induce the expression of its target genes that, in turn, control the process of DNA-repair, the cell-cycle arrest and the apoptotic cascade (Vogelstein *et al*., 2000).

The activity of p53 is down regulated by the cellular oncoprotein Mdm2 (Freedman *et al*., 1999) that promotes its ubiquitin-dependent degradation (Honda *et al*., 1997), inhibits its transcriptional function (Momand *et al*., 1992) and exports it from the nucleus to the cytoplasm (Roth *et al*., 1998). The action of Mdm2 has been demonstrated to be coupled with the formation of a complex with p53 (Momand *et al*., 1992). However, detailed information on the overall structure of the corresponding complex is missing to date, mainly due to the presence, within both proteins, of large unstructured regions (Bell *et al*., 2002; Dawson *et al*., 2003) that prevent the entire complex from crystallization. The only piece of structural and kinetic information available to date derives from studies performed on partial domains of both p53 and Mdm2 (Kussie *et al*., 1996; Lai *et al*., 2000; Schon *et al*., 2002; Chi *et al*., 2005).

Undoubtedly, a study involving the two entire proteins would be better suited for a more realistic and comprehensive knowledge about their interaction. Moreover, the importance of investigating this interaction is not limited to structural or kinetic aspects: due to the role of p53 on cellular equilibrium and integrity, it represents a central target for a variety of attractive anticancer strategies with the common aim at stabilizing and enhancing p53 tumour-suppression function (Vassilev *et al*., 2004; Wiman, 2006; Bossi and Sacchi, 2007; Vassilev, 2007).

In this connection, it has been reported that azurin, a copper-containing protein with electron-transfer activity in

* *Correspondence to: S. Cannistraro, Biophysics and Nanoscience Centre, Facoltà di Scienze, Università della Tuscia; Largo dell'Università, 01100 Viterbo, Italy.*
E-mail: cannistr@unitus.it

a *G. Funari, F. Domenici, A. R. Bizzarri, S. Cannistraro*
Biophysics and Nanoscience Centre, CNISM, Facoltà di Scienze, Università della Tuscia, Viterbo, Italy

b *L. Nardinocchi, R. Puca, G. D'Orazi*
Molecular Oncogenesis Laboratory, Regina Elena Cancer Institute, Rome, Italy

c *G. D'Orazi*
Department of Oncology and Neurosciences, University 'G. D'Annunzio', Chieti, Italy

Pseudomonas Aeruginosa (Vijgenbbom *et al*., 1997), plays an anticancer role, as observed in different cell lines: it can enter cancer cells and induce their apoptotic death *in vitro* and *in vivo* (Yamada *et al*., 2002). Interestingly, it has been demonstrated that the pro-apoptotic action of azurin on cancer cells is concomitant with the formation of a complex with p53, thereby leading to both its stabilization and its intracellular level increase.

In this connection, the p53/azurin complex has been subjected to different experimental investigations (Yamada *et al*., 2002; Apiyo and Wittung-Stafshede, 2005; Taranta *et al*., 2008a).

Site-direct mutagenesis (Yamada *et al*., 2002) has shown that azurin interacts through two methionine residues located within its hydrophobic patch surrounding the copper atom, with a not univocally established portion of p53. Two different docking computational studies have predicted that azurin could interact with the DNA-binding domain (DBD) of p53 (De Grandis *et al*., 2007) or, alternatively, contact its N-terminal region (Taranta *et al*., 2008b). The latter possibility is also suggested by an experimental fluorescence work (Apiyo and Wittung-Stafshede, 2005). Nevertheless, even if the molecular mechanism underlying the action of azurin has to be completely elucidated, the protein is undoubtedly capable to stabilize p53, contrasting in such a way the negative regulation exerted by Mdm2. An appealing hypothesis to this end could be that azurin, by contacting the p53 N-terminal portion, might partially, or totally, cover the Mdm2-binding site on p53 and therefore prevent the two proteins from association and then p53 from degradation.

Before examining this working hypothesis, we have assessed the formation of the p53/Mdm2 complex involving the two entire proteins with atomic force spectroscopy (AFS). This innovative and powerful nano-technological methodology, able to investigate the strength and kinetics of bio-complexes, at the single-molecule level, in native conditions and without any label or sample preparation, has been widely employed in recent times to get detailed information on biological interactions (Ratto *et al*., 2004; Bonanni *et al*., 2005; Bonanni *et al*., 2006; Hinterdorfer and Dufrêne, 2006; Sulchek *et al*., 2006) We have found that a specific bio-recognition process occurs between p53 and Mdm2 when the full-length-protein interaction is studied at the single-molecule level by AFS. The measured binding strength and dissociation rate constant of the corresponding complex fall in the range of values typical of ligand/receptor interactions. Moreover, it has been observed that azurin, even if it is capable to strongly and specifically bind p53, does not appear to compete with Mdm2 for the same binding site.

MATERIALS AND METHODS

Protein expression and purification

Glutathione S-transferase (GST) fusions of human MDM2 (kindly provided by A. L. Haas, LSU Health Sciences Center, New Orleans, LA, USA) and human wild-type-p53 (kindly provided by S. Soddu, National Cancer Institute 'Regina Elena', Rome, Italy) were expressed in log phase *Escherichia coli* BL-21 that had been grown overnight at room temperature, diluted 1:20 in fresh Luria-Bertani medium containing 50 μg/ml ampicillin at 37°C with vigorous shaking. Isopropyl-1-thio-β-D-galactoside (IPTG) was added to a final concentration of 0.4 mM when the OD_{600} reached 0.4–0.8 value. Bacteria were harvested 3 h after addition of IPTG by centrifugation at 5000 rpm for 10 min. Cell pellets were resuspended with NENT buffer (Tris 20 mM at pH 8, NaCl 100 mM, EDTA 1 mM and NP40 0.5%), proteases inhibitors, phenylmethylsulfonylfluoride (PMSF) 1 μM and lysozyme and lysed by sonication. The sonicate was clarified by centrifugation at 4°C for 15 min at 5000 rpm and stored at −80°C. Levels of expressed GST fusion proteins were estimated by incubating sonicates with glutathione-Sepharose (GS) beads (Sigma), washing, and quantification by SDS-PAGE followed by staining with Comassie Brilliant Blue R-250. Known amounts of bovine serum albumine (BSA) were used as standards. Cleavage of the GST portion was achieved by digestion with thrombine CleaveClean kit (Sigma) according to the manufacturer's instructions. The quality, correct folding, and purity of the obtained proteins were assessed through structural and functional studies, as reported in the Supporting Material.

Tip functionalization

Silicon nitride cantilevers (Veeco Instruments, Santa Barbara, CA) used in the experiments consist of contact microlevers with backside gold coating and an oxide-sharpened tip. The tips were cleaned in acetone for 10 min, dried with a stream of nitrogen and then UV irradiated for 30 min. Tips were then immersed in a solution of 2% (v/v) 3-mercatopropyl-trimethoxysilane (Aldrich) in toluene, incubated for 2 h at room temperature, then extensively washed with toluene and dried with nitrogen. The silanized tips were immersed in a solution of 1 mM N-hydroxysuccinimide-polyethylenglycol-maleimide (NHS-PEG-MAL, MW 3400 Da, 30 ± 10 nm in length, from Nektar Therapeutics) in DMSO for 3 h at room temperature. This spacer contains a thiol-reactive group (MAL) at one end, to link silane molecules, and an amino-reactive group (NHS) at the other end, to couple $–NH_2$ groups of lysines exposed on the protein surface. Tips were then rinsed in three changes of DMSO to remove the unbound PEG. Eventually tips were incubated on parafilm, according to a protocol previously described (Ebner *et al*., 2007) with 50 μl of a 3.2 μM solution of Mdm2 (and, in alternative, a 10 μM solution of azurin, from Sigma) for 4 h at 4°C, then gently rinsed with buffer and stored in PBS at 4°C. The protocol used is sketched in Figure 1A.

Substrate preparation

The substrates used in our experiments consist of vacuum-evaporated thin gold film (250 nm in thickness) on borosilicate glass (Arrandee, Germany). These substrates were firstly flame-annealed (to obtain re-crystallized Au (111) terraces), immersed in a solution of 0.2 mM cisteamine (Sigma) in ethanol for 3 h at room temperature, then washed with ethanol and dried under a stream of nitrogen. The modified substrates were incubated with 100 μl of a solution of 1% glutaraldehyde (Sigma) in milliQ water for 10 min at room temperature, rinsed carefully with milliQ water and dried with nitrogen. For the protein immobilization, 50 μl of a solution of 1.2 μM p53-GST fusion protein were dropped on the amine-reactive surface of the substrates and incubated over-night at 4°C. Next day the substrates were gently washed and stored in milliQ water at 4°C. The protocol used is sketched in Figure 1B.

Imaging and force spectroscopy

The substrate imaging and the force measurements were performed with a Nanoscope IIIa/ Multimode atomic force

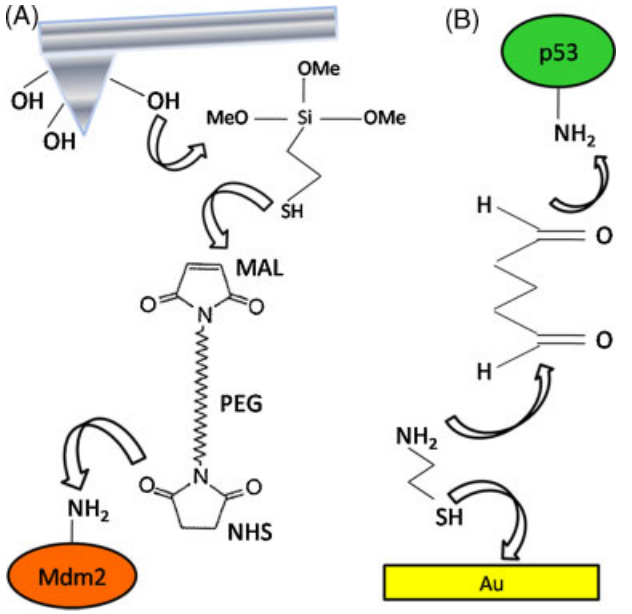

Figure 1. Schematic sketch of the surface chemistry employed to covalently anchor p53 and Mdm2 to AFM supports. (A) Mdm2 protein is bound to the mercapto-silanized tip via a 30 nm-long PEG chain. (B) p53 molecules are attached to a gold substrate via a chemical platform involving cisteamine and glutaraldehyde sequentially linked. Both p53 and Mdm2 are bound by randomly targeting aminic groups of lysine residues exposed on the protein surfaces. (For additional details see Materials and Methods section).

microscopy (AFM; Digital instruments, Santa Barbara, CA). Imaging of the p53 substrate was conducted in milliQ water by tapping mode AFM, with an amplitude set point corresponding to the 95% of the free amplitude value. The cantilever nominal spring constant, k_{nom}, was 0.5 N/m. Scratching of the substrate (to assess the presence of a single protein layer) was performed in contact mode AFM, by using a cantilever with a k_{nom} of 0.02 N/m. The applied force was varied from few nano-Newton for imaging to hundreds of nano-Newton for scratching. Force measurements were carried out in 50 mM (pH 7.2) PBS buffer by force calibration mode AFM. The cantilevers used to perform force measurements had k_{nom} of 0.02 and 0.03 N/m. The effective spring constants of the cantilevers, $k_{effective}$, calibrated using the non-destructive thermal noise method (Hutter and Bechhoefer, 1993), were in the range of 0.017–0.045 N/m. In all measurements a relative trigger of 23–35 nm was applied to limit at 0.7 nN the maximum contact force exerted on the protein monolayer by the tip, a ramp size of 150 nm was set and an encounter time (interval between approach and retraction phase) of 100 ms was established. The approach velocity was set, through the software actuating the piezo scan of our AFM Nanoscope IIIa, operating in open loop configuration, at a value of 69.8 nm/s, while the retraction velocity was changed from 50 to 8400 nm/s. Loading rates at which measurements were performed (instantaneous values, see Results and Discussion section) have been selected in the range 0.6–72 nN/s. All measurements performed for blocking experiments and competition experiments (see Results and Discussion section) were conducted at the same loading rate of 3 nN/s.

RESULTS AND DISCUSSION

p53/Mdm2 interaction

All experiments were performed by AFS, a single-molecule technique particularly useful to complement traditional proteomic and molecular biology approaches for the functional analysis of biological interactions (Zlatanova *et al*., 2000; Merkel, 2001; Rief and Grubmüller, 2002; Ratto *et al*., 2004; Bonanni *et al*., 2005; Bonanni *et al*., 2006; Hinterdorfer and Dufrêne, 2006; Sulchek *et al*., 2006; Taranta *et al*., 2008a). AFS is based on AFM, which operates by scanning a sharp tip mounted on a cantilever over a substrate. Inter-atomic forces, which are strongly dependent on tip-substrate distance, are measured by the cantilever deflection through the reflection of a laser beam from the back of the tip edge towards a photodiode. During the scan of the substrate (*xy* plane) the cantilever deflection is converted into height information to reproduce the surface topography. AFS exploits the principles of AFM to measure inter-atomic forces between the tip and the substrate at a fixed *xy* position. With reference to Figure 2, a ligand-functionalized tip is approached to a surface covered by immobilized receptors (point 1); at a given tip-sample distance the cantilever begins to deflect in consequence of intermolecular repulsive forces (point 2). From this point on, the cantilever exerts a pushing force on the substrate as evidenced by its deflection, while ligand and receptor, brought in close proximity, can interact and form a complex. The approach phase (dotted line) is stopped when the cantilever applies upon the substrate the maximum contact force (limited in order to avoid protein damage), having undergone an upward deflection, as shown in point 3. Next, the direction of motion is reversed and the cantilever retracts from the surface. During this retraction phase (continuous line) the cantilever reaches the baseline deflection and, by increasing further the tip-sample distance, it begins to bend downward (due to the attractive interaction-force displayed by the ligand–receptor complex, point 4). Its deflection follows a nonlinear course (curved tract) because of the stretching of the linker. When the force exerted by the cantilever overcomes the stability of the complex bonds, a sudden jump in the deflection occurs, as a consequence of the complex

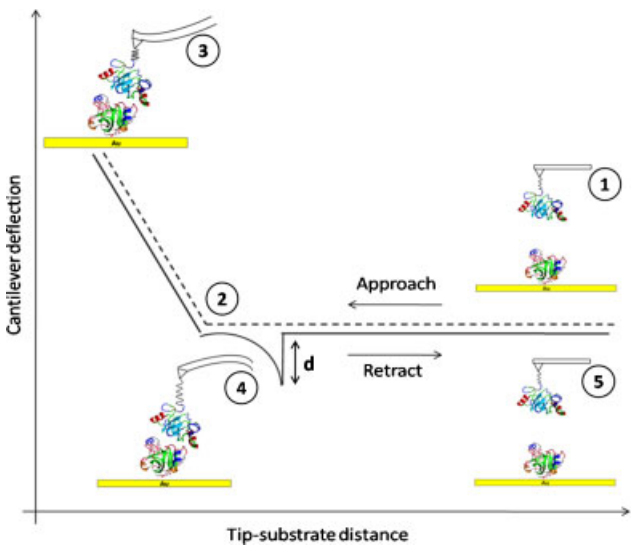

Figure 2. Sketch of AFS experiments. See text for a detailed description.

dissociation that separates the ligand–receptor pair (point 5). The deflection (d) measured at the jump-point is used to determine the force required to break the complex, the so called 'unbinding or rupture force', as the product between such deflection and the constant of the functionalized cantilever, by considering it as a spring governed by the Hooke law.

A fundamental prerequisite to investigate a ligand–receptor interaction by AFS is a robust attachment of ligand and receptor on their respective AFM supports, preferentially through covalent bonds, which are unquestionably stronger than those characteristics of protein-protein interactions (Hinterdorfer and Dufrêne, 2006). The strong immobilization of the two partners is useful to ensure the stability of the tethered system during time, by allowing repeated approach/retraction cycles.

Our immobilization strategy, described in details in Materials and Methods section, is schematically illustrated by the tethered system sketched in Figure 2 (point 1). Mdm2 was covalently fastened to the AFM tip via a flexible 30 nm-long polymer PEG (Figure 1A). The use of such a linker confers flexibility and provides the necessary re-orientational freedom for the occurrence of the bio-recognition between ligand and receptor (Friddle *et al*., 2007). Moreover, the linker spatially isolates non-specific tip-substrate adhesions, taking place near to the substrate surface, from the specific unbinding events of proteins that, being tethered, dissociate at larger tip-substrate distance (Hinterdorfer *et al*., 1996; Hinterdorfer *et al*., 2000).

p53 was covalently bound to a gold slide through a chemical platform composed by cisteamine and glutaraldehyde linked in sequence, to generate a protein monolayer on the substrate surface (Figure 1B).

Both partners were immobilized by targeting aminic groups exposed on the protein surfaces. The presence of several lysine residues available for the reaction (with glutaralheyde or NHS-group) generated different orientations of the proteins on tip and substrate, some of which might have been unfavourable for the bio-recognition event (see later).

Before proceeding with AFS measurements, we evaluated the aspect of p53 molecules immobilized on gold slide by tapping mode AFM with a bare tip. Figure 3 (left side) shows an AFM image corresponding to noticeable single protein molecules assembled to form a dense and uniform p53 layer. To assess the presence of a monolayer (of the expected height) we performed a scratch on it with the tip working in contact mode. As shown in Figure 3 (right side), the scratch depth was found to be about of 5 nm that corresponds to the expected thickness for a single protein layer and the cysteamine-glutaralheyde platform.

By repeating force-distance cycles on the tethered system sketched in Figure 2 (point 1), we collected thousands of force-curves. All curves were recorded at a constant approach speed, while the retraction velocity was varied from 50 to 8400 nm/s. To prevent protein damage, we fixed at 0.7 nN the value for the maximum contact force applied on the substrate. In these experimental conditions we performed measurements at several distinct points of the substrate by obtaining different kinds of force-curves. The most recurrent ones are shown in Figure 4. Curves that display acceptable unbinding events are collected in the left panel. They are characterized by: sharp peaks, starting and ending points at zero-deflection line, an initial nonlinear curved shape, due to the viscoelastic properties of a PEG molecule under stretching (Kienberger *et al*., 2000b; Thormann *et al*., 2006), and straight pull-off jumps. The right panel, instead, shows curves discarded from the analysis due to the lack of events or the presence of hysteresis or dubious deflection-jumps. Moreover, control experiments with a bare tip versus a p53-coated substrate and with a Mdm2-functionalized tip versus a bare substrate. Under these conditions we registered curves similar to those shown in Figure 4B.

The unbinding frequency, defined as the ratio between the number of accepted unbinding events and the totality of the collected force-curves, was found to be about 15% (at a loading rate of 3 nN/s). Such frequency was found to be consistent with values previously reported for other biological interactions (Sulchek *et al*., 2005; Fuhrmann *et al*., 2008). Even if a low unbinding frequency might originate also from the massive presence of unfolded or inactive proteins, we were led to exclude such a possibility on the basis of surface plasmon resonance checks with p53 covalently bound to a gold substrate, as for force spectroscopy measurements, that gave results (unpublished

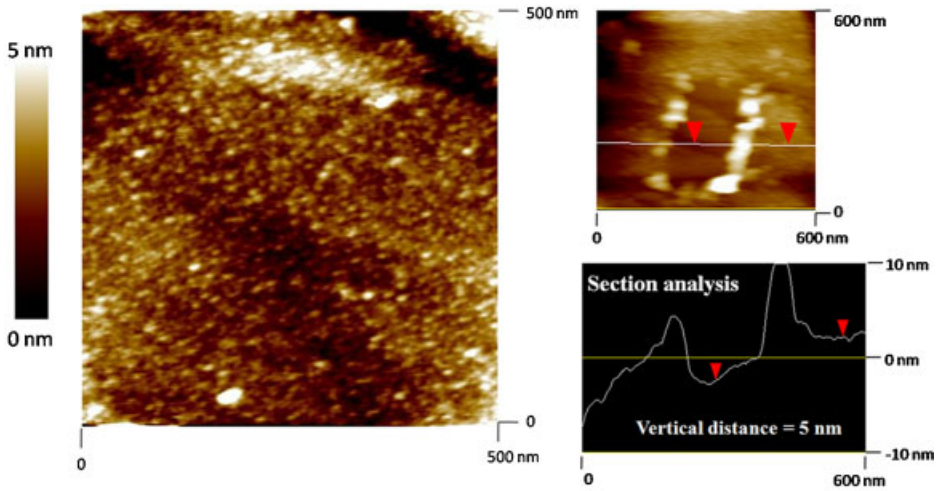

Figure 3. Left side: tapping mode AFM image of p53 monolayer on a gold substrate. The image has been recorded in milliQ water with an amplitude setpoint corresponding to the 95% of free amplitude value. Right side: contact mode AFM image of a scratching on p53 monolayer and the vertical profile analysis.

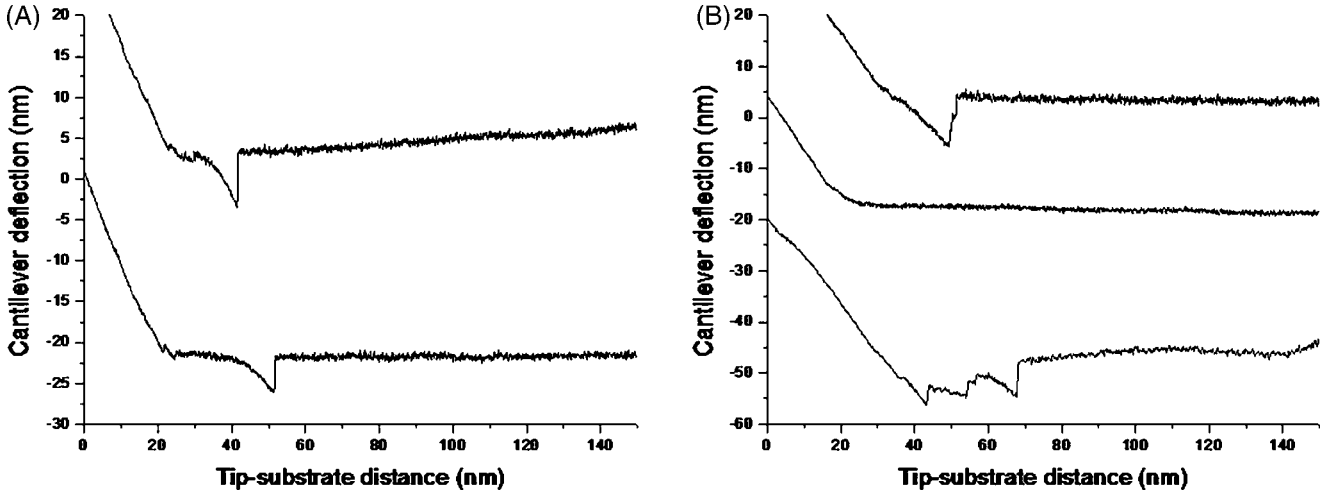

Figure 4. Representative examples of force-curves registered with a Mdm2-coated tip over a p53 protein monolayer (only the retraction traces are shown). The tip deflection (vertical axes) is plotted as a function of tip-substrate distance (abscissa axes). (A) Accepted curves containing specific unbinding events with sharp peak and nonlinear curved shape. (B) Rejected curves displaying adhesion (hysteresis), without events or with dubious adhesion events.

data) consistent with those obtained by force spectroscopy and in agreement with the literature (Schon *et al*., 2002). Rather, we believe that low unbinding frequencies could be due to the presence of unfavourable binding geometries and steric hindrance (Bonanni *et al*., 2005). Interestingly, the unbinding frequency was found to be dependent on the loading rate: it initially increased, reached a maximum and decreased thereafter, as already described (Lü *et al*., 2006).

As mentioned before, for each curve the unbinding force was determined as the product between the cantilever deflection (d) and its effective spring constant ($k_{effective}$). Accordingly, a number of force histograms, corresponding to the different loading rates at which the force spectroscopy measurements have been carried on, were generated. The histograms of the unbinding forces exhibit an almost single mode distribution with a skewness toward high force values; such an asymmetric shape, rather similar to that observed in other systems, can be due to several factors, such as multiple binding events, binding heterogeneity, etc (Baumgartner *et al*., 2000; Ratto *et al*., 2004; Sulchek *et al*., 2005). On such a basis, and in agreement with what commonly done in literature, we determined the most probable unbinding force from the maximum of the main peak of each histogram. At a loading rate of 3 nN/s, we found an unbinding force value of 105 ± 6 pN (Figure 5). This rupture force is in the range of values reported for other specific biological interactions at similar loading rates (Kienberger *et al*., 2000a; Zhang *et al*., 2002). The unbinding force values and the widths of their corresponding distributions increased with rising the loading rate, as observed in other force spectroscopy works (Janshoff and Steinem, 2001; Marshall *et al*., 2005).

Subsequently, to verify if the measured forces could be attributed to specific interaction events between p53 and Mdm2, we performed a blocking experiment on the complex. A solution of free Mdm2 was incubated on p53 substrate to allow the binding between p53 and the free molecules of Mdm2 to occur (Figure 6A). After incubation, we washed the substrate with buffer (to remove the unbound Mdm2) and we measured again the unbinding frequency with the same Mdm2-functionalized tip. Figure 6B shows a decrement from 15 to 5% of such unbinding frequency upon blocking. The significant reduction (of about 70%) observed after blocking is clearly indicative of the specificity of the p53/Mdm2 complex formation. The persistence of a residual unbinding activity (5%) upon blocking was observed also in other force spectroscopy experiments and could be related to the forced interaction between the two partners, induced by the experimental setup (Hinterdorfer *et al*., 1996; Wielert-Badt *et al*., 2002). Importantly, the force distributions before and after blocking (Figure 6C) showed a good overlap, thus indicating the same nature of the corresponding interactions.

Before describing the dissociation kinetics of the p53/Mdm2 complex by our force spectroscopy experiments, it is worth discussing, in more details, the general principles that govern the dissociation of a complex under the influence of an external force. In general, the application of a force to a complex until it

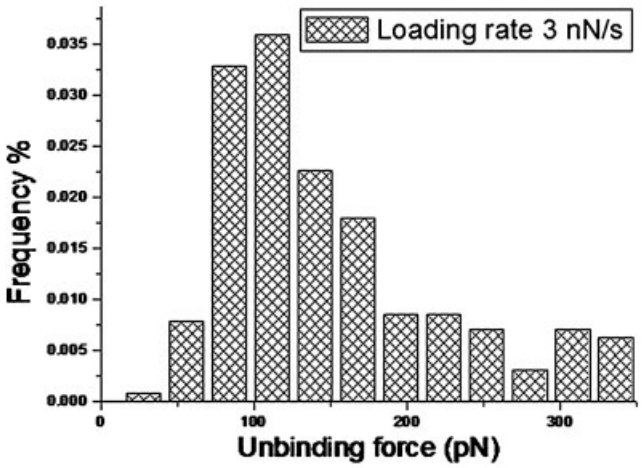

Figure 5. Unbinding force histogram for the p53/Mdm2 complex. The histogram was obtained by binning at 28 pN. The most probable unbinding force value was determined from the maximum of the main peak of each histogram. Data come from 210 unbinding events found within 1350 force curves, recorded at a loading rate of 3 nN/s.

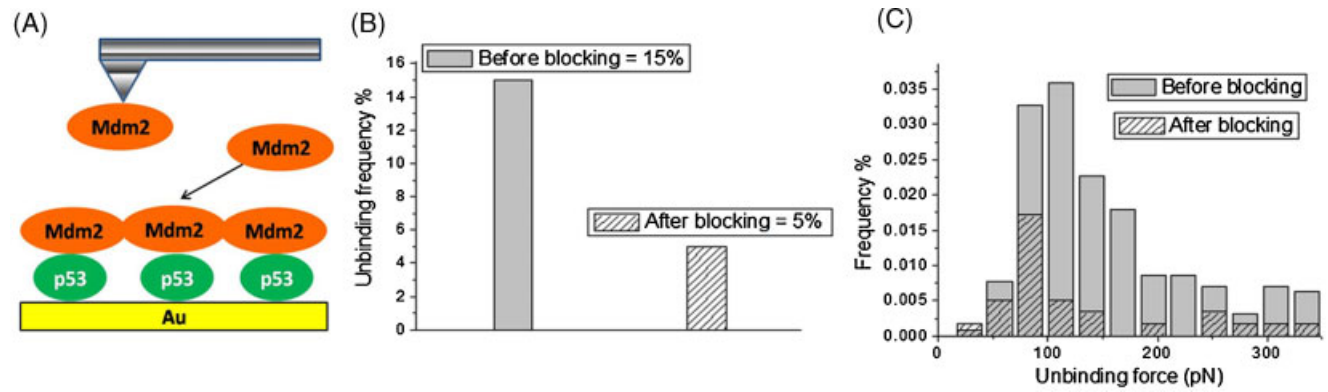

Figure 6. Blocking experiment. (A) A solution of free Mdm2 is incubated over the p53 monolayer. (B) Unbinding frequency between p53 and Mdm2 before and after blocking. (C) Unbinding force distributions before and after blocking. All measurements here illustrated are performed at a loading rate of 3 nN/s.

reaches the dissociated state renders the reaction a far-from equilibrium transformation that needs to be treated within an appropriate theoretical context. Bell-Evans model (Bell, 1978; Evans and Ritchie, 1997) represents the most widely used theory to explain and analyze force spectroscopy data. According to the model, the application of a force F on a complex toward the unbound state deforms the energy landscape of the ligand-receptor pair, leading to a reduction of the activation barrier and consequently in an exponential increase of the dissociation rate constant with the pulling force F, as follows:

$$k_{off}(F) = k_{off} \cdot \exp[F x_\beta/(k_B T)] \quad (1)$$

where k_{off} (F) and k_{off} are the dissociation rate constant in the presence and without any applied force respectively, x_β is the width of the potential barrier along the direction of the applied force, k_B is the Boltzmann's constant and T the absolute temperature. The effect of the applied force on the energy landscape distortion increases with raising the loading rate r_F at which the force is ramped. As a consequence the unbinding forces measured depend not only on the nature of the ligand-receptor interaction, but also on the rate at which the force is applied during time. As predicted by the model, in fact, the most probable rupture force F is a linear function of the natural logarithm of the loading rate r_F. Under conditions of constant loading rate r_F, the most probable unbinding force is given by the following expression:

$$F = (k_B T/x_\beta) \cdot \ln[r_F x_\beta/(k_{off}\, k_B\, T)] \quad (2)$$

Experimentally, F is determined from the maximum of the main peak of each force histogram, while for the loading rate it is considered the instantaneous value at the moment of bond rupture, determined as the product between the retraction speed and the spring constant of the entire system, k_{syst}. It is appropriate, in fact, to take into account the contribution of the spring constant of protein and linker molecules bound to the tip, by considering the k_{syst} parameter calculated from the slope of the retraction curve immediately prior to the unbinding event (Friedsam *et al.*, 2003).

By plotting the measured rupture forces versus the natural logarithm of the loading rate, we obtained a dynamic force spectrum displaying an evident linear relationship between the two quantities (Figure 7). The kinetic parameters x_β and k_{off}, at zero force conditions, were obtained by fitting the plot of F versus ln (r_F) with equation 2 and relate to the slope and intercept of the linear fit, respectively. Our dynamic force spectrum showed, at least in the range of the loading rates here taken in consideration, a single regime indicative of a single energy barrier and unique transition state of the reaction and provided values of 0.17 ± 0.01 nm for x_β and $1.5 \pm 0.5\ s^{-1}$ for k_{off}.

This k_{off} value falls within a range of values characteristic of several other ligand-receptor pairs, such as cadherins, selectins, integrins, etc. (Baumgartner *et al.*, 2000; Hanley *et al.*, 2003; Panorchan *et al.*, 2006; Friddle *et al.*, 2007; Lim *et al.*, 2008).

It is not surprising, on the other hand that the k_{off} value obtained for the p53/Mdm2 complex is found comparable to that of the above mentioned ligand-receptor pairs, rather to that of stronger complexes, such as antigen-antibody couples (with k_{off} going down to $10^{-10}\ s^{-1}$). Indeed, the cellular functionality of the p53/Mdm2 complex would more likely require a k_{off} typical of dynamical, transient interactions; for instance to allow, after the regulative association of Mdm2 to p53 for ubiquitination, the

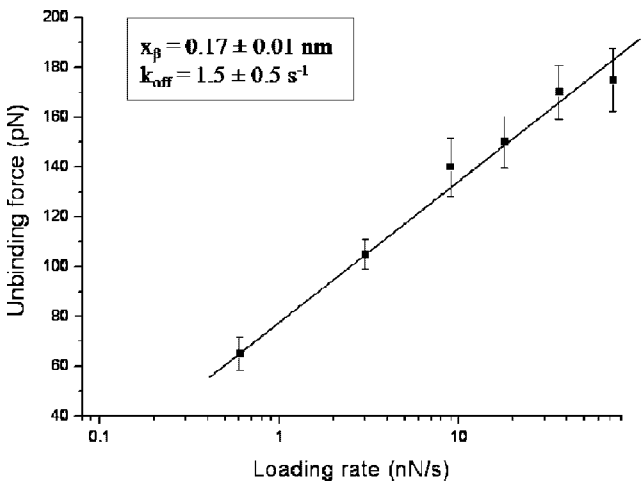

Figure 7. Dynamic force spectrum for the p53/Mdm2 interaction. Plot of the unbinding forces versus the natural logarithm of the different loading rates. The continuous line represents the fit of the experimental data with Bell-Evans model (equation 2). The kinetics parameters obtained are reported in the inset. The uncertainties of force values are given as $\sigma/(N)^{1/2}$, where σ is the standard deviation on N data.

dissociation of the latter to undergo degradation (Haupt *et al*., 1997; Kubbutat *et al*., 1997). Moreover, the k_{off} here estimated is very close to that determined in a stopped-flow fluorimetric study ($k_{off} = 2.0\,s^{-1}$), which has been obtained from the interaction between the two N-terminal domains of both p53 and Mdm2 (Schon *et al*., 2002), where the binding sites of the complex are supposed to be located (Chen *et al*., 1993). Taking into account the striking similarity of the two k_{off} values and, at the same time, the fact that our measured dissociation rate relates to a p53/Mdm2 complex as made up by the full-length proteins, it can be inferred that the two cognate binding sites of the complex undergo a bio-recognition process without any steric hindrance effect from the presence of the entire milieu of the proteins. The occurrence of a specific, dynamical complex between the full-length p53 and Mdm2 proteins, here evidenced for the first time by AFS, adds a new piece of valuable information about the mechanism of p53 regulation.

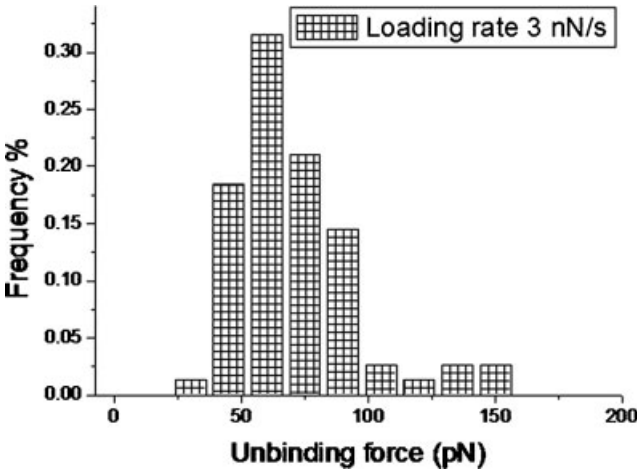

Figure 8. Unbinding force histogram for the p53/azurin interaction.

p53/azurin interaction

Before considering the effect of azurin on the p53/Mdm2 complex, we repeated AFS measurements on p53/azurin system, already studied in a previous work (Taranta *et al*., 2008a), to achieve an inner control, coherent with the present experimental setup. In the previous study, azurin was covalently linked to the AFM tip via one of the two thiol-groups located at the protein surface, a condition that favoured the exposure of the hydrophobic patch to facilitate the binding to p53 (Yamada *et al*., 2002). In the present case instead, azurin was bound to the tip by targeting one of its eleven aminic groups, belonging to lysines exposed on the protein surface. On the other hand, also p53 has been immobilized on the gold substrate with a different strategy with regard to the previous work, according to the protocol illustrated in Figure 1.

Again, we performed thousands of force-distance cycles on different sample positions. The force-curves were recorded at the same approach speed, but varying the retraction velocities to obtain the same loading rate values used for the p53/Mdm2 interaction (0.6–72 nN/s). By processing the curves with the same analysis criteria adopted for the p53/Mdm2 interaction, we obtained a mean unbinding frequency of 14% (at a loading rate of 3 nN/s). This frequency was found to be somewhat lower than that observed in the previous work (19%), due to the random immobilization of azurin in the present case.

All the unbinding force histograms, obtained at the different loading rates, were characterized by clustered distributions. We determined the most probable rupture force from the maximum of the main peak of each force histogram and we found an unbinding force value of 60 ± 5 pN, at a loading rate of 3 nN/s (Figure 8), a value consistent with that reported in the previous work.

Again, the specificity of the unbinding forces and the complex formation was assessed by blocking p53 molecules with a solution of 26 μM azurin and eventually washing the substrate with buffer to remove the unbound azurin. We observed, as a result, a significant reduction from 14 to 6% of the unbinding frequency that was indicative of the specificity of the interactions.

The plot of the unbinding forces versus the natural logarithm of the loading rate (not shown) displayed a linear relationship between the two quantities and provided a k_{off} of $2.4 \pm 1.1\,s^{-1}$.

The k_{off} here obtained indicates that the p53/azurin interaction shows a lower stability than the p53/Mdm2 one: the lifetime of the p53/azurin complex at zero force (τ_0), defined as $1/k_{off}$ (Bell, 1978), results to be, in fact, of 0.4 s, in comparison with 0.7 s for the p53/Mdm2 complex.

p53/Mdm2/azurin competition experiments

As before reported, the formation of a specific p53/Mdm2 complex occurs with the two entire proteins that interact at the level of both their N-terminal domains. On the other hand, azurin can specifically bind to an undetermined region of p53, with its hydrophobic patch. In this respect, it could be very interesting to investigate about a possible competition of azurin with Mdm2 for the same binding site on p53 N-terminus.

In order to probe such a hypothesis, we conceived competitive blocking experiments. The strategy adopted by us is schematically sketched in Figure 9. Firstly, we estimated the frequency of the unbinding events between immobilized p53 and Mdm2 (15%), and then we blocked the substrate with a solution of free azurin, as a possible competitive agent for the p53/Mdm2 interaction (Figure 9A). After washing the substrate, we measured again the unbinding frequency that was found to be almost unchanged after blocking (16%; Figure 9B). To strengthen such a result, we repeated a second blocking experiment in a different protein-combination: we measured the unbinding frequency between immobilized p53 and azurin (14%) and then we blocked the substrate with free Mdm2, by using it as a putative competitor (Figure 9C). Again, after washing, no substantial reduction in the rupture frequency was found (12%; Figure 9D).

These results indicate that no competition is observed between azurin and Mdm2 for the same binding site on p53. From such an evidence and the fact that p53 specifically interacts with both Mdm2 and azurin, it can be inferred that a p53/Mdm2/azurin ternary complex is formed. Very likely, within such complex p53 and Mdm2 would interact by their respective N-terminal domains (Chen *et al*., 1993; Kussie *et al*., 1996), while azurin could bind, through its hydrophobic patch (Yamada *et al*., 2002), to the DBD of p53, as recently proposed by a docking study (De Grandis *et al*., 2007).

We therefore wonder if such a ternary complex might play a functional role. Intriguingly, we could speculate about the possibility that binding of azurin to the p53-DBD could interfere with the ubiquitination process, which is catalyzed by Mdm2 at

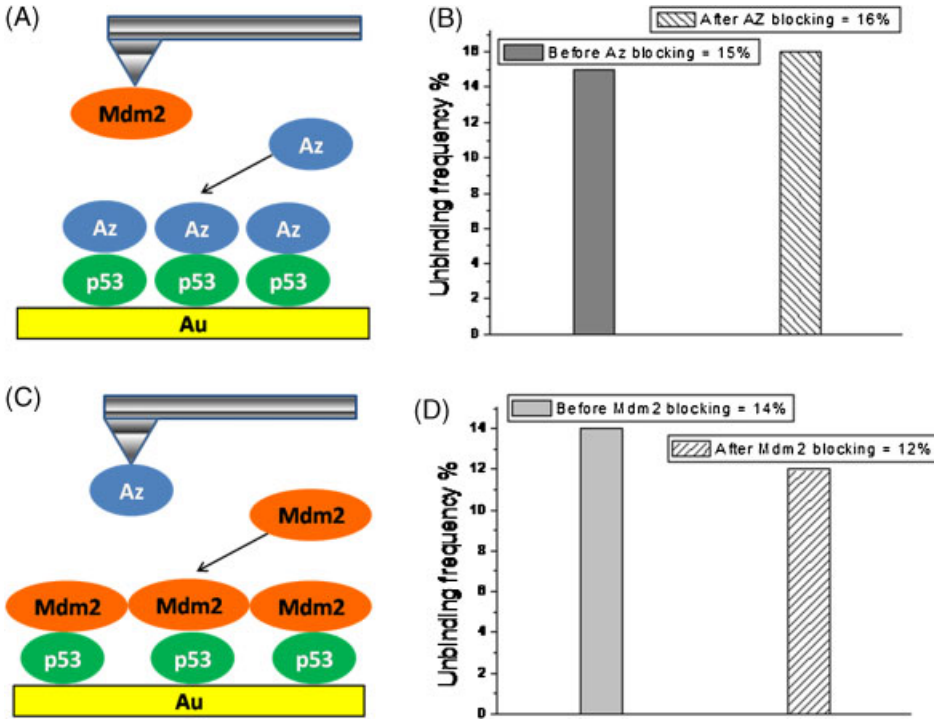

Figure 9. Competitive blocking experiments on the p53/Mdm2/azurin ternary complex. (A) Sketch of the system with azurin used as competitor. (B) Unbinding frequency before and after blocking with azurin. (C) Sketch of the system with Mdm2 used as competitor. (D) Unbinding frequency before and after blocking with Mdm2. All measurements refer to a loading rate of 3 nN/s.

the level of lysine residues located within the p53-DBD (Chan *et al*., 2006), and thus resulting in a steric protection of crucial sites involved in p53 negative regulation (Clegg *et al*., 2008). Undoubtedly, further investigation will be required to assess a possible biological relevance of such a ternary complex.

In conclusion, AFS has proven to be a powerful approach to complement biochemical and bio-molecular information on the p53/Mdm2 interaction. In fact, it allowed us to reach unprecedented kinetic results on the p53/Mdm2 complex formed by the two full-length proteins. Moreover, the AFS study on p53/Mdm2/azurin system has evidenced that the stabilization induced by azurin on p53 cannot be attributed to a competitive binding with respect to Mdm2, for the N-terminal domain of p53. The occurrence of a p53/Mdm2/azurin ternary complex opens a possible new scenario for the anti-cancer action of azurin.

Acknowledgements

All the authors would like to thank Dr. Ada Sacchi (Regina Elena Cancer Institute, Rome; Italy) for useful discussion and suggestions. We are grateful to Prof. Agostina Congiu Castellano and her group for providing circular dichroism equipment. G.F. thanks Dr. Monia Taranta for experimental advises. R. P. is a recipient of a Fellowship from Fondazione Italiana per la Ricerca Sui Cancro (FIRC). The work was partially supported by the PRIN-MIUR 2006 project n. 2006027587.

REFERENCES

Apiyo D, Wittung-Stafshede P. 2005. Unique complex between bacterial azurin and tumour-suppressor protein p53. *Biochem. Biophys. Res. Commun.* **332**: 965–968.

Baumgartner W, Hinterdorfer P, Ness W, Raab A, Vestweber D, Schindler H, Drenckhahn D. 2000. Cadherin interaction probed by atomic force microscopy. *Proc. Natl Acad. Sci. USA* **97**: 4005–4010.

Bell GI. 1978. Models for the specific adhesion of cells to cells. *Science* **200**: 618–627.

Bell S, Klein C, Müller L, Hansen S, Buchner J. 2002. p53 contains large unstructured regions in its native state. *J. Mol. Biol.* **322**: 917–927.

Bonanni B, Bizzarri AR, Cannistraro S. 2006. Optimized biorecognition of cytochrome c 551 and azurin immobilized on thiol-terminated monolayers assembled on Au (111) substrates. *J. Phys. Chem. B* **110**: 14574–14580.

Bonanni B, Kamruzzahan SM, Bizzarri AR, Rankl C, Gruber HJ, Hinterdorfer P, Cannistraro S. 2005. Single molecule recognition between cytochrome c 551 and gold-immobilized azurin by force spectroscopy. *Biophys. J.* **89**: 2783–2791.

Bossi G, Sacchi A. 2007. Restoration of wild-type p53 function in human cancer: relevance for tumour therapy. *Head & Neck* **29**: 272–284.

Chan RY, Mak MC, Fung TK, Lan A, Sin WY, Poon RY. 2006. Ubiquitination of p53 at multiple sites in the DBD—binding domain. *Mol. Cancer Res.* **1**: 15–25.

Chen J, Marechal V, Levine AJ. 1993. Mapping of the p53 and Mdm2 interaction domains. *Mol. Cell. Biol.* **13**: 4107–4114.

Chi SW, Lee SH, Kim DH, Ahn MJ, Kim JS, Woo JY, Torizawa T, Kainosho M, Han KH. 2005. Structural details on Mdm2-p53 interaction. *J. Biol. Chem.* **18**: 38795–38802.

Clegg HV, Itahana K, Zhang Y. 2008. Unlocking the Mdm2/p53 loop. *Cell Cycle* **7**: 1–6.
Dawson R, Muller L, Dehner A, Klein C, Kessler H, Buchner J. 2003. The N-terminal domain of p53 is natively unfolded. *J. Mol. Biol.* **332**: 1131–1141.
De Grandis V, Bizzarri AR, Cannistraro S. 2007. Docking study and free energy simulation of the complex between p53 DNA-binding domain and azurin. *J. Mol. Recognit.* **20**: 215–226.
Ebner A, Hinterdorfer P, Gruber HJ. 2007. Comparison of different aminofunctionalization strategies for attachment of single antibodies to AFM cantilevers. *Ultramicroscopy* **107**: 922–927.
Evans E, Ritchie K. 1997. Dynamic strength of molecular adhesion bonds. *Biophys. J.* **72**: 1541–1555.
Freedman DA, Wu L, Levine AJ. 1999. Functions of the Mdm2 oncoprotein. *Cell. Mol. Life Sci.* **55**: 96–107.
Friddle RW, Sulchek TA, Albrecht H, De Nardo SJ, Noy A. 2007. Counting and breaking individual biological bonds: Force spectroscopy of tethered ligand-receptor pairs. *Current Nanosci.* **3**: 41–48.
Friedsam C, Wehle AK, Kuhner F, Gaub HE. 2003. Dynamic single molecule force spectroscopy: bond rupture analysis with variable spacer length. *J. Phys. Cond. Matt.* **15**: S1709–S1723.
Fuhrmann A, Anselmetti D, Ros R. 2008. Refined procedure of evaluating experimental single-molecule force spectroscopy data. *Phys. Rev.* **E77** 031912: 1–10.
Hanley W, McCarty O, Jadhav S, Tseng Y, Wirtz D, Konstantopoulos K. 2003. Single molecule characterization of P-selectin/Ligand binding. *J. Biol. Chem.* **278**: 10556–10561.
Harris SL, Levine AJ. 2005. The p53 pathway: positive and negative feedback loops. *Oncogene* **24**: 2899–2908.
Haupt Y, Maya R, Kazaz A, Oren M. 1997. Mdm2 promotes the rapid degradation of p53. *Nature* **387**: 296–299.
Hinterdorfer P, Baumgartner W, Gruber HJ, Schilcher K, Schindler H. 1996. Detection and localization of individual antibody-antigen recognition events by atomic force microscopy. *Proc. Natl Acad. Sci. USA* **93**: 3477–3481.
Hinterdorfer P, Dufrêne YF. 2006. Detection and localization of single molecular recognition events using atomic force microscopy. *Nature Meth.* **3**: 347–355.
Hinterdorfer P, Kienberger F, Raab A, Gruber HJ, Baumgartner W, Kada G, Riener C, Wielert-Badt S, Borken C, Schindler H. 2000. Poly (Ethylene Glycol): an ideal spacer for molecular recognition force microscopy/spectroscopy. *Single Mol.* **1**: 99–103.
Honda R, Tanaka H, Yasuda H. 1997. Oncoprotein Mdm2 is an ubiquitin ligase E3 for tumor suppressor p53. *FEBS Lett.* **420**: 25–27.
Hutter JL, Bechhoefer J. 1993. Calibration of atomic-force microscope tips. *Rev. Sci. Instrum.* **64**: 1868–1873.
Janshoff A, Steinem C. 2001. Energy landscapes of ligand-receptor couples probed by dynamic force spectroscopy. *ChemPhysChem* **2**: 577–579.
Kienberger F, Kada G, Gruber HJ, Pastushenko V, Riener C, Trieb M, Knaus HG, Schindler H, Hinterdorfer P. 2000a. Recognition force spectroscopy studies of the NTA-His6 bond. *Single Mol.* **1**: 59–65.
Kienberger F, Pastushenko VP, Kada G, Gruber HJ, Riener C, Schindler H, Hinterdorfer P. 2000b. Static and dynamical properties of single poly (ethylene glycol) molecules investigated by force spectroscopy. *Single Mol.* **1**: 123–128.
Ko LJ, Prives C. 1996. p53: puzzle and paradigm. *Genes Develop.* **10**: 1054–1072.
Kubbutat MH, Jones SN, Vousden KH. 1997. Regulation of p53 stability by Mdm2. *Nature* **387**: 299–303.
Kussie PH, Gorina S, Marechal V, Elenbaas B, Moreau J, Levine AJ, Pavletich NP. 1996. Structure of the Mdm2 oncoprotein bound to the p53 tumor suppressor transactivation domain. *Science* **274**: 948–953.
Lai Z, Auger KR, Manubay CM, Copeland RA. 2000. Thermodynamics of p53 binding to hdm2 (1–126): effects of phosphorylation and p53 peptide length. *Arch. Biochem. Biophys.* **381**: 278–284.
Lavin MF, Gueven N. 2006. The complexity of p53 stabilization and activation. *Cell Death Diff.* **13**: 941–950.
Levine AJ. 1997. p53, the cellular gatekeeper for growth and division. *Cell* **88**: 323–331.
Lim TS, Vedula SR, Kausalya PJ, Hunziker W, Lim CT. 2008. Single-molecular-level study of claudin-1-mediated adhesion. *Langmuir* **24**: 490–495.
Lü S, Ye Z, Zhu C, Long M. 2006. Quantifying the effects of contact duration, loading rate, and approach velocity on P-selectin-PSGL-1 interactions using AFM. *Polymer* **47**: 2539–2547.
Marshall BT, Sarangapani KK, Lou J, McEver RP, Zhu C. 2005. Force history dependence of receptor-ligand dissociation. *Biophys. J.* **88**: 1458–1466.
Merkel R. 2001. Force spectroscopy on single passive biomolecules and single biomolecular bonds. *Physics Reports* **346**: 343–385.
Momand J, Zanbetti GP, Olson DC, George D, Levine AJ. 1992. The Mdm2 oncogene product forms a complex with the p53 protein and inhibits p53-mediated transactivation. *Cell* **69**: 1237–1245.
Oren M. 2003. Decision making by p53: life, death and cancer. *Cell Death Diff.* **10**: 431–442.
Panorchan P, Thompson MS, Davis KJ, Tseng Y, Konstantopoulos K, Wirtz D. 2006. Single molecule analysis of cadherin-mediated cell-cell adhesion. *J. Cell Sci.* **119**: 66–74.
Ratto TV, Langry KC, Rudd RE, Balhorn RL, Allen MJ, McElfresh MW. 2004. Force spectroscopy of the double-tethered concanavalin A mannose bond. *Biophys. J.* **86**: 2430–2437.
Rief M, Grubmüller H. 2002. Force spectroscopy of single biomolecules. *ChemPhysChem* **3**: 255–261.
Roth J, Dobbelstein M, Freedman DA, Shenk T, Levine AJ. 1998. Nucleo-cytoplasmic shuttling of the hdm2 oncoprotein regulates the levels of the p53 protein via a pathway used by the human immunodeficiency virus rev protein. *EMBO J.* **2**: 554–564.
Schon O, Friedler A, Bycroft M, Freund SMV, Fersht AR. 2002. Molecular mechanism of the interaction between Mdm2 and p53. *J. Mol. Biol.* **323**: 491–501.
Sulchek TA, Friddle RW, Langry K, Lau EY, Albrecht H, Ratto TV, DeNardo SJ, Colvin ME, Noy A. 2005. Dynamic force spectroscopy of parallel individual Mucin-1-antibody bonds. *Proc. Natl Acad. Sci. USA* **102**: 16638–16643.
Sulchek T, Friddle RW, Noy A. 2006. Strength of multiple parallel biological bonds. *Biophys. J.* **90**: 4686–4691.
Taranta M, Bizzarri AR, Cannistraro S. 2008a. Probing the interaction between p53 and the bacterial protein azurin by single molecule force spectroscopy. *J. Mol. Recognit.* **21**: 63–70.
Taranta M, Bizzarri AR, Cannistraro S. 2008b. Modelling the interaction between the N-terminal domain of the tumor suppressor p53 and azurin. *J. Mol. Recognit. 22:* 215–222.
Thormann E, Hansen PL, Simonsen AC, Mouritsen OG. 2006. Dynamic force spectroscopy on soft molecular systems: improved analysis of unbinding spectra with varying the linker compliance. *Coll. Surf. B: Bioint.* **53**: 149–156.
Vassilev LT. 2007. Mdm2 inhibitors for cancer therapy. *Trends Mol. Med.* **13**: 23–31.
Vassilev LT, Vu BT, Graves B, Carvajal D, Podlaski F, Filipovic Z, Kong N, Kammlott U, Lukacs C, Klein C, Fotouhi N, Liu EA. 2004. *In vivo* activation of the p53 pathway by small-molecule antagonists of Mdm2. *Science* **303**: 844–848.
Vijgenbbom E, Busch JE, Canters GW. 1997. *In vivo* studies disprove an obligatory role of azurin in denitrification in *Pseudomonas Aeruginosa* and show that azurin expression is under control of RpoS and ANR. *Microbiology* **143**: 2853–2863.
Vogelstein B, Lane D, Levine AJ. 2000. Surfing the p53 network. *Nature* **408**: 307–310.
Wielert-Badt S, Hinterdorfer P, Gruber H, Lin JT, Badt D, Wimmer B, Schindler H, Kinne RK., 2002. Single molecule recognition of protein binding epitopes in brush border membranes by force microscopy. *Biophys. J.* **82**: 2767–2774.
Wiman KG. 2006. Strategies for therapeutic targeting of the p53 pathway in cancer. *Cell Death Diff.* **13**: 921–926.
Yamada T, Goto M, Punj V, Zaborina O, Chen ML, Kimbara K, Majumdar D, Cunningham E, Das Gupta TK, Chakrabarty AM. 2002. Bacterial redox protein azurin, tumour suppressor protein p53, and regression of cancer. *Proc. Natl Acad. Sci. USA* **99**: 14098–14103.
Zhang X, Wojcikiewicz E, Moy VT. 2002. Force spectroscopy of the leukocyte function-associated antigen-1/intercellular adhesion molecule-1 interaction. *Biophys. J.* **83**: 2270–2279.
Zlatanova J, Lindsay SM, Leuba SH. 2000. Single molecule force spectroscopy in biology using the atomic force microscope. *Progress Biophys. Mol. Biol.* **74**: 37–61.

Research Article

Journal of Molecular Recognition

Received: 3 August 2010, Revised: 28 September 2010, Accepted: 30 September 2010, Published online in Wiley Online Library: 2011

(wileyonlinelibrary.com) DOI:10.1002/jmr.1105

Azurin Modulates the Association of Mdm2 with p53: SPR Evidence from Interaction of the Full-Length Proteins

Fabio Domenici[a], Marco Frasconi[b], Franco Mazzei[b], Gabriella D'Orazi[c,d], Anna Rita Bizzarri[a] and Salvatore Cannistraro[a]*

The tumour suppressor p53 plays a crucial role in cell stress response and its anticancer activity is mainly down-regulated by the oncoprotein Mdm2 that, upon binding to p53, blocks its transcriptional activity and promotes its ubiquitin-dependent degradation. Targeting Mdm2–p53 interaction is believed to be the most direct of all p53-activating strategies to treat tumours in which p53 has retained its wild-type function. The bacterial protein Azurin has been shown to bind p53, inhibiting cancer cell proliferation likely through a post-translational increasing of the p53 level. This apparent antagonist action with respect to the Mdm2–p53 functional interaction suggests that binding of Azurin to p53 might interfere with the Mdm2–p53 association and, thus, preventing p53 from degradation. Toward this end, a detailed kinetic characterization of the binding interaction of these three proteins has been performed by surface plasmon resonance. The occurrence of specific binary interactions of both Azurin and Mdm2 with p53, as investigated more appropriately in their full-length conformation, is ascertained and the corresponding association and dissociation rate constants are measured. Interestingly enough, the three proteins are likely engaged in a ternary interaction, whose kinetics points out that binding of Azurin to p53 causes a significant decrease of the Mdm2–p53 association rate constant and binding affinity, without hindering the accessibility of Mdm2 to the binding pocket of p53. The Azurin-induced p53 conformational change, as demonstrated by circular dichroism, suggests that the protein may affect Mdm2–p53 association through an allosteric mechanism, which could give an useful insight into designing new anticancer drugs. Copyright © 2011 John Wiley & Sons, Ltd.

Keywords: p53; azurin; mdm2; surface plasmon resonance

INTRODUCTION

A great deal of the scientific efforts, made toward the comprehension of the network controlling cell proliferation, is focused on the tumour suppressor role played by the transcriptional p53 protein (Toledo and Wahl, 2006). Human p53 consists of four main domains which are responsible for its transcriptional activation, DNA-binding and tetramerization functions (Lavin and Gueven, 2006; Veprintsev *et al*., 2006). When DNA damage is sensed, the p53 level rises and the protein binds to sequence-specific regulatory sites in the genome, thereby inducing the expression of genes that control the DNA repair and interrupting the cell growth until the damage is repaired; on the other hand, if the damage is too severe, p53 triggers the apoptotic cascade (Vogelstein *et al*., 2000; Lavin and Gueven, 2006).

p53 is mainly down-regulated by the oncoprotein Mdm2 which inhibits its transcriptional activity (Momand *et al*., 1992), shuttles p53 toward the cytoplasmic proteasome and promotes its ubiquitin-dependent degradation (Honda *et al*., 1997; Roth *et al*., 1998; Freedman *et al*., 1999). Such a regulative action of Mdm2 has been demonstrated to be coupled to the formation of a complex with p53 (Momand *et al*., 1992; Moll and Petrenko, 2003), in which the N-terminal regions of both proteins come into close contact (Kussie, 1996; Schon *et al*., 2002). Detailed information on the overall structure of the corresponding complex is however, missing to date, mainly due to the lack of the crystallographic pictures of both full-length proteins undergoing the interaction. Most of the structural and kinetic information currently available is derived from studies performed only on partial domains of both p53 and Mdm2 (Kussie, 1996; Lai *et al*., 2000; Schon *et al*., 2002; Chi *et al*., 2005).

* *Correspondence to: S. Cannistraro, Biophysics and Nanoscience Centre, Facoltà di Scienze, Università della Tuscia; Largo dell'Università, 01100 Viterbo, Italy.*
E-mail: cannistr@unitus.it

a *F. Domenici, A. R. Bizzarri, S. Cannistraro*
Biophysics and Nanoscience Centre, CNISM, Facoltà di Scienze, Università della Tuscia, Viterbo, Italy

b *M. Frasconi, F. Mazzei*
Department of Chemistry and Drug Technologies, "Sapienza" University of Rome, P.le Aldo Moro 5, 00185 Rome, Italy

c *G. D'Orazi*
Molecular Oncogenesis Laboratory, Regina Elena Cancer Institute, Rome, Italy

d *G. D'Orazi*
Department of Oncology and Neurosciences, University "G. D'Annunzio", Chieti, Italy

An *in vitro* binding study of the complex involving the two full-length, native proteins has been conducted by atomic force spectroscopy (AFS), a new nanotechnological tool able to investigate even a single couple of interacting partners to complement biochemical information on biorecognition processes (Bizzarri and Cannistraro, 2010). AFS put into evidence the occurrence of a specific complex between p53 and Mdm2 characterized by a dissociation rate constant (k_{off}) of about 1.5 s^{-1} (Funari *et al*., 2010).

The importance of investigating this interaction is not limited to structural or kinetic aspects; indeed stabilizing and enhancing p53 tumour-suppression function in cancer cells, even by inhibiting its physical interaction with Mdm2, is the main focus of anticancer drug discovery (Klein and Vassilev, 2004; Bossi and Sacchi, 2007).

In this context, it has been reported that the purified bacterial copper-containing protein Azurin (Az) plays a prominent anticancer role. Several *in vitro* and *in vivo* studies have shown that the protein can enter cancer cells and induce their apoptotic death (Yamada *et al*., 2002, 2004, 2005; Punj *et al*., 2004). Interestingly, it has been demonstrated that this pro-apoptotic action of Az is concomitant with the formation of a complex with p53, thereby leading to both its stabilization and intracellular level increase (Yamada *et al*., 2002). The Az–p53 binding process has been therefore investigated by means of different experimental methodologies. Site-direct mutagenesis has shown that Az interacts through two methionine residues, located within its hydrophobic patch surrounding the copper atom, with a not univocally established region of p53 (Yamada *et al*., 2002)). A number of experimental and computational studies have hypothesized the occurrence of either a direct interaction of Az with the p53 N-terminal domain (aa 1–93) (Apiyo and Wittung-Stafshede, 2005; Taranta *et al*., 2009) or, alternatively, with the DNA-binding domain (DBD) (aa 94–292) of p53 (De Grandis *et al*., 2007; Yamada *et al*., 2009). The specificity of the Az–p53 interaction has been demonstrated also by AFS (Taranta *et al*., 2008) and the corresponding k_{off} value has been measured ($9 \cdot 10^{-2}\ s^{-1}$), while the association rate constant (k_{on}) and the dissociation constant (K_d) of the complex, involving the two full-length proteins, have been only estimated.

Despite the fact that the molecular mechanism involved in the Az anticancer action it is not fully understood it is clear that this protein is able to stabilize p53, apparently acting as an antagonist of Mdm2. An appealing hypothesis to this end could be that binding Az to p53 might prevent Mdm2 and p53 from association and, thus, p53 from degradation. In that context, our group has conceived unbinding experiments by AFS (Funari *et al*., 2010) that ruled out a direct binding competition between Az and Mdm2 with respect to p53, and have suggested the possible formation of a ternary interaction among Az, Mdm2 and p53. Since such a ternary interaction could contribute to open a new scenario on the anticancer action of Az, we have then performed a detailed kinetic study of the binding among Az, Mdm2 and p53, by means of surface plasmon resonance (SPR) analysis.

SPR represents a strategic tool in protein-binding studies, especially suited for sensitive kinetic process investigations, in real time and without labeling procedures (Cooper, 2003).

The SPR experiments, conducted here for the first time on the three full-length biomolecules, have evidenced the occurrence of specific binary interactions of both Az and Mdm2 with p53 and provided the corresponding association and dissociation rate constants, and thus the equilibrium constants. A strong association among the three full-length proteins has been registered. Remarkably, we found that the interaction of Az with p53 modulates the Mdm2–p53 binding kinetics by reducing of more than four times the corresponding association rate constant, through a non competitive binding. An allosteric mechanism for this Az-induced inhibition of the Mdm2–p53 association is proposed on the basis of circular dichroism (CD) evidence of changes in the p53 secondary structure occurring upon binding of Az.

EXPERIMENTAL PROCEDURES

Protein preparations

Azurin was purchased from Sigma–Aldrich (St. Louis, Mo), dissolved in PBS 50 mM buffer (pH 7.2) and used without further purification.

The expression and purification of Mdm2 and p53 proteins were obtained following the standard Glutathione S-transferase (GST) method as previously reported (Funari *et al*., 2010). Quality, correct folding and purity of the recombinant proteins used in our SPR experiments were checked through different experimental procedures summarized in the following (see also supporting material in ref. (Funari *et al*., 2010).

The purity of the proteins produced was assessed through gel electrophoresis experiments. The GST and thrombin-purified proteins were separated by SDS-PAGE and analyzed by densitometry. All thrombin-cleaved preparations were of $\geq$ 95% homogeneity.

The folding of the proteins was checked by CD studies. They showed that the secondary structures of the expressed p53 (16% α-helix, 30% β-sheet 54% unordered) and Mdm2 (24% α-helix, 20% β-sheet 56% unordered) were in agreement with the literature for wild-type p53 and Mdm2 (Bell *et al*., 2002; Iakoucheva *et al*., 2002).

The conformation of p53, produced through the GST-method, was studied by immunoprecipitation technique, using two conformation-specific antibodies (Gannon *et al*., 1990; Legros *et al*., 1994).

Immunocomplexes were collected by centrifugation, separated by 10% SDS-PAGE and blotted onto PVDF membrane. Immunoblotting was performed with rabbit polyclonal anti-p53 (FL393, Santa Cruz Biotechnology) antibody and revealed by enhanced chemiluminescence system (ECL, Amersham, IL, USA). As expected, purified p53 resulted exclusively in the wild-type conformation and therefore suitable for wt-p53 activity assay, such as DNA binding.

p53-covered substrate preparation

The planar gold SPR sensor disks for the protein immobilization were purchased from Xantec Bioanalytics (GmbH Munster, Germany). These gold substrates were immersed in an ethanol solution of cysteamine (0.2 mM, Sigma) for 3 h at room temperature (RT), then washed with ethanol and dried under a stream of nitrogen. The modified substrates were incubated with 250 μl of a milliQ water 1% glutaraldehyde (Sigma) solution for 10 min at RT, rinsed carefully with milliQ water and dried with nitrogen. Then, 250 μl of 1.2 μM p53 protein in TST buffer (pH 7.2) was dropped on the amine-reactive surface of the substrate and

incubated over-night at 4 °C. Next day the substrate was gently washed with PBS (pH 7.2) and stored in PBS buffer at 4 °C. A covalent binding between the glutaraldehyde linker and the exposed NH_2 groups of p53 leads to immobilization of the p53 molecules in a multioriented configuration, maintaining at the same time some reorientational freedom to facilitate biorecognition and avoiding denaturation due to direct contact of the protein with the gold surface. Tapping-mode atomic force microscopy (AFM) images in fluid (cantilever force constant, $k = 0.5$ N/m) were recorded by means of a Park XE-100 multimode scanning probe microscope during the different steps of the sample preparation and shown in Figure 1.

SPR binding experiment

An SPR Kretschmann type spectrometer Autolab Esprit (Eco Chemie, Utrecht, The Netherlands), with a LED light source emitting at 670 nm and a prism with 1.52 refraction index was used to measure the intensity of the reflected light at the corresponding resonance angle. This angle can be measured over a range of 4° after focusing by a lens into a photodiode detector. The incident angle was varied by using a vibrating mirror (rotating over an angle of 5° at 77 Hz) with a resolution of one millidegree. The glass supported SPR substrates were clamped against a Teflon cuvette with O-rings, providing liquid-tight seals. An autosampler (Eco Chemie) with controllable aspirating–dispensing–mixing pipette was used to add samples into the cuvette and provide constant mixture by aspiration and dispensing during measurements. This experimental arrangement assures a homogeneous solution and reproducible hydrodynamic conditions. The temperature of the cuvette was kept at 25 ± 1 °C.

By following the time varying SPR angle shift due to binding molecular processes occurring at the sensor surface in real time, it is possible to measure the association and dissociation kinetics of the interaction. In order to confirm the nature of the protein–protein interaction and regenerate the sensor surface after every binding cycle, we evaluated the use of regeneration solutions at different pH and ionic strength (Andersson *et al*., 1999). Among them, a 0.5 M NaCl solution at pH = 5.0 was shown to be mostly effective for disassembling the Mdm2–p53 interaction, although subsequent massive loss of the p53 substrate binding capacity was observed, likely due to partial p53 denaturation (Bom *et al*., 2010). Thus SPR binding studies were conducted by injecting the interacting protein on untreated p53 substrate portions and the homogeneity of p53 deposition was checked (see Figure 1). Further control experiments and reference subtraction were performed to exclude any possible unspecific binding contribution.

Regarding the experiments on the ternary interaction, Az 2 μM in PBS solution (pH 7.2) or Mdm2 2 μM in TST solution (pH 7.2), was incubated on the overall p53-covered substrate for 3 h at 25 °C, and saturation of the p53 binding site was checked on each investigated area by SPR measurements. To check that the saturation condition is maintained also during the sensorgrams acquisition, further SPR control experiments have been performed, by mixing the protein injected with that used to saturate the p53-modified sensor disk (2 μM of Az or Mdm2).

Kinetic analysis of the SPR sensorgrams

Global analysis (Morton and Myszka, 1998) of the SPR sensorgrams was performed by using simultaneous nonlinear regression fit procedure derived from a reversible bimolecular interaction model:

$$A + B \underset{k_{off}}{\overset{k_{on}}{\rightleftarrows}} AB$$

where *A* is the receptor injected in the flow chamber, *B* the ligand immobilized on the surface of the SPR sensor disk and *AB* is the product of the specific interaction.

For this model, the following differential rate equations can be derived to determine the association (k_{on}, $M\,s^{-1}$) and dissociation (k_{off}, s^{-1}) rate constants for protein-protein binding interaction:

$$\text{association} : \frac{d[AB]}{dt} = k_{on}[A][B] - k_{off}[AB] \quad (1)$$

$$\text{dissociation} : -\frac{d[AB]}{dt} = k_{off}[AB] \quad (2)$$

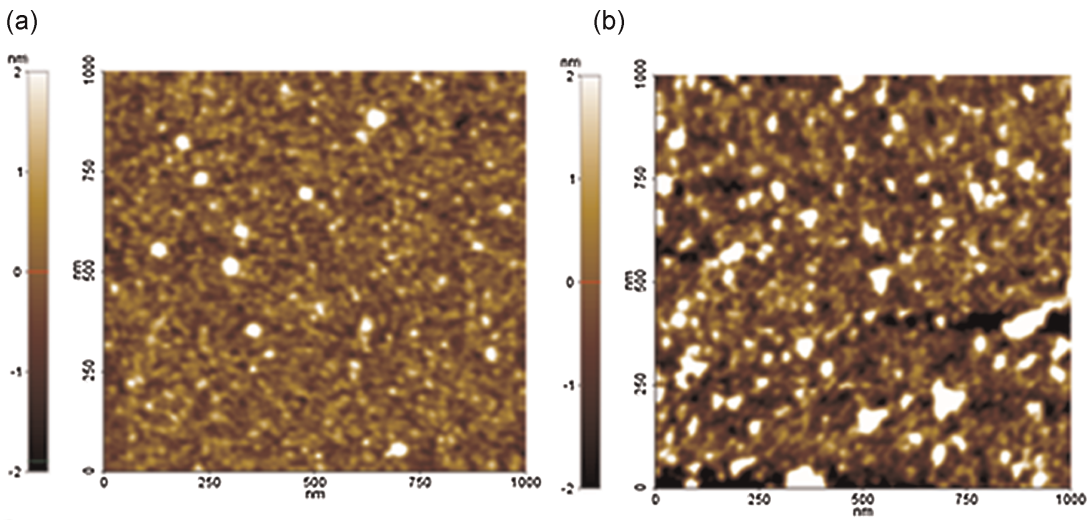

Figure 1. Tapping mode AFM images of the sensor disk surface coated with SAM: before (a) and after (b) incubation with p53. The images has been recorded in PBS buffer solution with a cantilever force constant of 0.5 N/m. The corresponding root mean square roughness (R_q) was 0.5 ± 0.1 nm (a) and1.0 ± 0.1 nm (b).

The kinetic analysis was performed by Clamp biosensor software (Morton and Myszka, 1998). Because the reaction rates in the flow chamber may be limited by the rate of protein diffusion from bulk solution to the sensor surface, the fitting procedure also takes into account for the mass-transport limit effects (Myszka *et al.*, 1997).

The quality of the fits was judged by the residuals and the normalized chi square (χ^2) of the fitting model. In addition, the validity of the obtained rate constants was assessed by simulating data with identical ratio values of the rate constants and varying k_{off} and k_{on} values. The equilibrium dissociation constant (K_d, M), inversely related to the binding affinity, was then determined from the ratio of the measured kinetic parameters:

$$K_d = k_{off}/k_{on} \quad (3)$$

CD Measurements

Circular dichroism measurements were performed both on bare p53 and on p53 previously incubated with Az at 1:1 molar ratio (this corresponds to a 4:1 molar ratio when we consider that p53 is a tetrameric molecule) for 3 h at 25 °C using a JASCO J-715 spectropolarimeter, equipped with a 0.1 cm path length and thermally controlled quartz cell. CD spectra were recorded at 25 °C in TST buffer at pH of 7.2 (50 mM Tris buffer with 150 mM NaCl and 0.1% Triton × 100) and at 0.50 μM proteins concentration obtained by quantitative dilution of the mother solution to prevent spectral contribution from protein aggregation.

All spectra were the average of ten repeats obtained by collecting data from 250 to 190 nm at 0.5 nm intervals, at a rate of 50 nm/min with a response time of 2 s for each point.

The experimental patterns acquired in millidegrees of ellipticity θ, were corrected by solvent subtraction and converted to mean residue ellipticity $[\theta]_{MRW}$. The predicted content of secondary structure was calculated using the CD spectra deconvolution software CDSSTR (Whitmore and Wallace, 2004) with a normalized root mean square deviation value of 0.01.

RESULTS AND DISCUSSION

Binding rate constants and equilibrium dissociation of the complex formed by full-length Mdm2 and p53

We have detected the specific interaction between the Mdm2 and p53 entire proteins by SPR analysis, and the corresponding sensorgrams are shown in Figure 2.

We have before checked the purity, folding and functionality of p53 and Mdm2 samples as described in the experimental procedures section; we have moreover monitored the preparation of the p53 modified sensor disks by the AFM analysis as shown in Figure 1. After incubation of the SPR gold-coated disks with a p53 solution, the sample roughness (R_q), measured over a scanned area of $1.0 \times 1.0\ \mu m^2$, was found to increase from 0.5 ± 0.1 to 1.0 ± 0.1 nm, indicating a successful deposition of the p53 proteins which are shown to adhere strongly to the substrate (Funari *et al.*, 2010).

In order to obtain accurate and reproducible kinetic data, we have repeatedly collected SPR sensorgrams obtained from the injection of Mdm2 protein solutions, at six different concentrations (ranging from 0.1 to 2 μM), on the sensor disks covered by p53. The SPR signal as a function of time provides the binding kinetic characterization of the complex. Upon Mdm2 injection (at an assigned concentration), the observed time-dependent signal increased up to a plateau as due to the Mdm2–p53 association (Eq. 1); after removal of the Mdm2 solution and subsequent buffer injection, the observed decreasing profile characterizes the kinetics of the Mdm2–p53 dissociation (Eq. 2). The kinetic rate constants and equilibrium dissociation values, obtained from the best fits of the SPR signals shown in Figure 2, are summarized in Table 1 (first row). They are

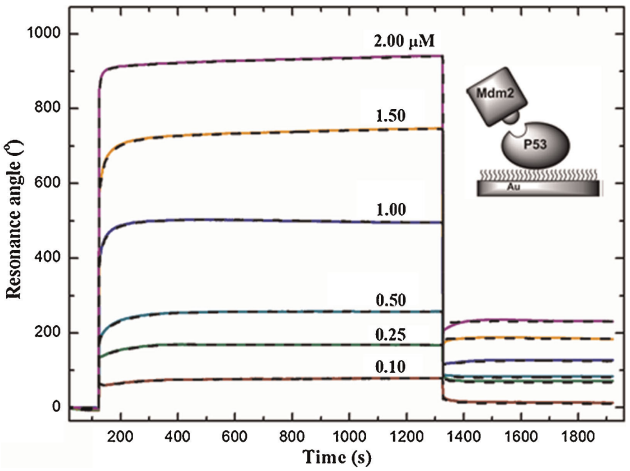

Figure 2. SPR sensorgrams for the binding–unbinding screen of Mdm2 on p53- modified sensor disk, with a cartoon of the interaction geometry. The SPR angle shift as function of time after injection and removal of the Mdm2 solutions (TST buffer, pH 7.2) at six concentrations is shown (solid profiles). The Mdm2–p53 association phases were registered over 20 min at flow rate of 50 μl/min and $T = 25$ °C. Best fits (dashed black profiles) were performed by using simultaneous nonlinear regression analysis to a reversible bimolecular interaction model (see experimental procedures section).

Table 1. Kinetics and equilibrium constants measured by SPR of the binary and ternary complexes formed by the full-length proteins Az, Mdm2 and p53. The global analysis was performed by the Clump biosensor software.

Complex	Binding rate constants and equilibrium dissociation constant
MdM2/p53 binary	$k_{off} = 0.8 \pm 0.3\ s^{-1}$ $k_{on} = (2.1 \pm 0.2)\ 10^6\ M\ s^{-1}$ $K_d = (0.4 \pm 0.1)\ 10^{-6}$ M ($\chi^2 = 98\%$)
Az/p53 binary	$k_{off} = (9.4 \pm 0.7)\ 10^{-2}\ s^{-1}$ $k_{on} = (8.2 \pm 0.5)\ 10^4\ M\ s^{-1}$ $K_d = (1.2 \pm 0.1)\ 10^{-6}$ M ($\chi^2 = 95\%$)
Az/(p53-MdM2) ternary	$k_{off} = (9.0 \pm 0.3)\ 10^{-2}\ s^{-1}$ $k_{on} = (6.8 \pm 0.5)\ 10^4\ M\ s^{-1}$ $K_d = (1.3 \pm 0.1)\ 10^{-6}$ M ($\chi^2 = 99\%$)
MdM2/(p53-Az) ternary	$k_{off} = (0.6 \pm 0.2)\ s^{-1}$ $k_{on} = (5.0 \pm 0.3)\ 10^5\ M\ s^{-1}$ $K_d = (1.2 \pm 0.4)\ 10^{-6}$ M ($\chi^2 = 97\%$)

consistent with the typical values of ligand-receptor pairs undergoing a dynamic, transient interaction (Nooren and Thornton, 2003).

The k_{off} value is very close to that obtained by AFS (1.5 s^{-1}) for the Mdm2–p53 complex, always formed by full-length partners (Funari *et al.*, 2010) and the K_d value is also consistent with the dissociation constant ($K_d = 0.2$ μM) measured in a stopped-flow fluorimetric study (Schon *et al.*, 2002) on the interaction between the N-terminal polypeptide of both Mdm2 and p53. This indicates that, even if the main Mdm2 binding site presumably involves a short helix formed by residues 18–26 of p53 (26 1996; Schon *et al.*, 2002), the two cognate binding sites of the complex undergo a biorecognition process without significant steric hindrance as due to the presence of the entire milieu of the proteins.

It has been recently suggested that the Mdm2–p53 association may also be triggered by initial molecular collisions and multiple approach orientations involving the entire polypeptide chain (which is quite extended and almost completely unfolded) of the p53 N-terminal portion (Dawson *et al.*, 2003; Chi *et al.*, 2005; Toledo and Wahl, 2006). Therefore, the previous Mdm2–p53 complex studies, mostly performed only on their partial domains, provide dissociation constant values ranging from nano to microMolar, according to the different peptide length considered (Lai *et al.*, 2000; Jianhong *et al.*, 2006; Ferreon *et al.*, 2009). A tenfold stronger dissociation constant ($K_d = 0.3$ μM) has been found when, at least, the entire p53 was used (Dawson *et al.*, 2003). Such a value shows a better agreement with the present SPR results and significantly points out that a study involving the two full-length proteins would be better suited for a more realistic and comprehensive knowledge of the p53–Mdm2 interaction.

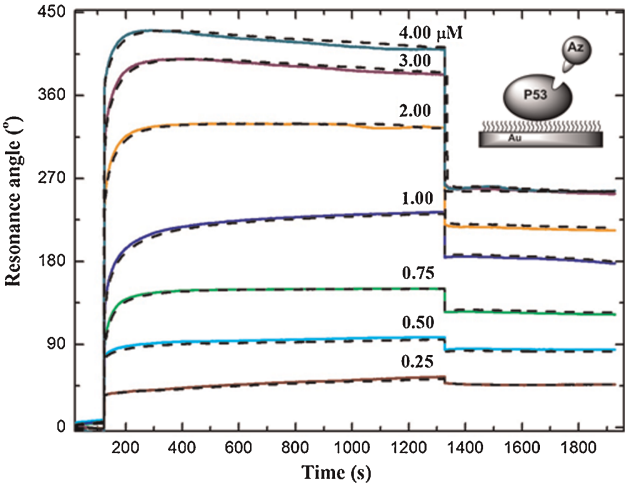

Figure 3. SPR sensorgrams for the binding-unbinding screen of Az on p53-modified sensor disk, with a cartoon of the interaction geometry. The SPR angle shift as function of time after injection and removal of the Az solutions (PBS buffer, pH 7.2) at seven concentrations is shown (solid profiles). The Az–p53 association phases were registered over 20 min at flow rate of 50 μl/min and $T = 25$ °C. Best fits (dashed black profiles) were performed by using simultaneous nonlinear regression analysis to a reversible bimolecular interaction model (see experimental procedures section).

Binding kinetics of full-length p53 and Az and corresponding changes in the p53 secondary structure

Before considering the effect of Az on the formation of the Mdm2–p53 complex, we have performed the binding kinetics measurements also on the binary complex formed by the two entire Az and p53 proteins. The SPR sensorgrams, shown in Figure 3, have been obtained by injecting Az at seven different concentrations, ranging from 0.25 to 4 μM, onto the p53-functionalized substrate. The obtained binding parameters, shown in Table 1, are consistent with the occurrence of a specific Az–p53 complex. While the k_{off} value is in good agreement with that obtained by AFS on the same complex at the single molecule level (Taranta *et al.*, 2008), the corresponding k_{on} and K_d values are instead measured here for the first time.

Quite interestingly, the dissociation constant of the Az–p53 complex results to be only threefold lower than that of the Mdm2–p53 complex, although both the k_{off} and k_{on} values are found much lower than those relevant to this complex (compare the first to the second row of Table 1).

Indeed, two interaction processes with similar affinity may display widely different association and/or dissociation timescale, according to the biochemical mechanism underlying the functional interaction (Robert *et al.*, 2007). In particular, regulative functions requiring rapid transient interactions, could plausibly be characterized from short lifetime (the inverse of k_{off} provides the lifetime of the corresponding complex). In this respect, the Az–p53 complex which displays a higher lifetime is thereby characterized by a more stable interaction than that corresponding to the Mdm2–p53 complex.

On the other hand, the k_{on} value characterizes the inverse of association time at unit concentration of the components and molecular recognition may be driven by binding-induced conformational changes, which could rise the binding association time (lower k_{on}) reasonably to lead the complex to a more stable final state (with lower k_{off}) (Boehr *et al.*, 2009; Robert *et al.*, 2009).

Since similar binding-induced structural changes have been observed also in many protein–protein interactions involving natively unfolded proteins, such as p53 (Pontius, 1993; Uversky, 2002; Dyson and Wright, 2002; Kumar and Thompson, 2003; Dahlman-Wright *et al.*, 1995) we have conceived a far-UV CD experiment in order to investigate the effect of Az binding on the p53 folding.

The CD spectrum recorded from the Az/p53 complex at 1:1 molar ratio shows significant differences with respect to that from wild-type p53 (see Figure 4). In particular, the appearance of both a deep minimum centred at around 206 nm and a shoulder at 220 nm, points out the formation of an alpha-helix motif. Since Az displays a rigid folding (Adman, 1991), the observed changes can be attributed to an Az-induced folding in p53. The data analysis has quantified that the Az-induced secondary structure of p53, from unfolded state to alpha-helix, is of about 10%. Such a conformational change could involve intrinsically unfolded regions within the p53 N-terminal domain (Apiyo and Wittung-Stafshede, 2005) where the Mdm2 binding site is supposed to be located (Kussie, 1996; Dawson *et al.*, 2003; Apiyo and Wittung-Stafshede, 2005; Vise *et al.*, 2005).

Binding kinetics of the Az–p53–Mdm2 association

In this section, we report on the SPR analysis of the Az–p53–Mdm2 ternary interaction as hypothesized by AFS in

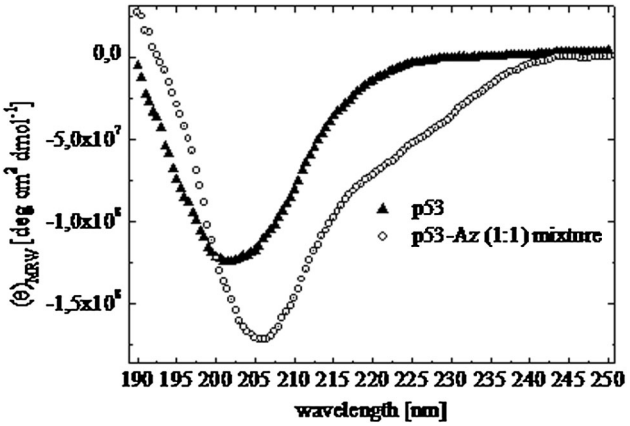

Figure 4. Far-UV CD spectra of p53 alone (black triangles); and in the presence of Az (circles) (1:1 molar ratio) acquired at 25 °C in TST buffer solution (pH 7.2). Buffer signals was subtracted for p53 alone. The spectrum of Az–p53 solution was corrected for Az and buffer contributions.

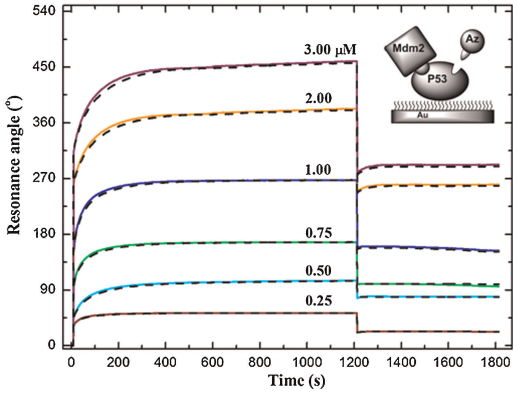

Figure 5. SPR sensorgrams for the binding process of Az with Mdm2–p53 complex, with a cartoon of the interaction geometry. The SPR angle shift as function of time after injection and removal of the Az solutions (PBS buffer, pH 7.2) at six concentrations is shown (solid profiles). Best fits (dashed black profiles) were obtained by using simultaneous nonlinear regression analysis to a reversible bimolecular interaction model (see details in the experimental procedures section).

ref. (Funari *et al*., 2010). We aim at both extracting the relevant kinetic parameters and ascertaining if the observed Az–p53 specific interaction can interfere with the binding kinetics of the Mdm2–p53 complex.

To this end, we need to consider both the binding kinetics of Az with the Mdm2–p53 complex and the binding kinetics of Mdm2 with the Az–p53 complex.

For the first binding configuration, we have treated p53, immobilized on the SPR substrate, with an excess of Mdm2 solution until its binding capacity for Mdm2 has resulted totally reduced as checked by SPR sensorgram, and then we have injected the Az solution on the Mdm2–p53 complex immobilized on SPR sensor disk to analyze the interaction kinetics. Experiments have been performed also by injecting Az mixed with Mdm2 to avoid equilibrium perturbation on the Mdm2–p53 interaction and to ascertain that the SPR response was really due to the specific binding of Az to p53, in turn associated with Mdm2 (see also experimental procedures section).

The sensorgrams obtained at six different concentration of Az are shown in Figure 5. The corresponding kinetic rate constants and equilibrium dissociation values, which have been reported in Table 1 (third row), are found almost equivalent to those obtained for the Az–p53 binary complex (compare the second to the third row of Table 1). This result confirms that Az and Mdm2 do not compete for the same binding site within p53, but they are involved a ternary interaction (Az–p53–Mdm2), as already hypothesized (Funari *et al*., 2010).

We have then studied the interaction of Mdm2 with the Az–p53 complex as follows. After having treated the p53 immobilized on the substrate with an excess of Az solution to saturate its Az binding sites, we have injected the Mdm2 solution at the same six concentrations used for the previous experiment on the Mdm2–p53 binary complex. Experiments have been performed also by injecting Mdm2 mixed with Az to avoid equilibrium perturbation on the Az–p53 interaction and to ascertain that the SPR response was due to the specific binding of Mdm2 to p53 associated with Az.

The obtained SPR sensorgrams are shown in Figure 6 and the extracted kinetic parameters are summarized in Table 1 (fourth row).

Very interestingly, a comparison of the latter SPR analysis with that of the Mdm2–p53 binary interaction indicates that Az affects the interaction of Mdm2 with p53 by reducing of more than four times the corresponding association rate constant (k_{on} goes from $= 2.1 \cdot 10^6$ to $5.0 \cdot 10^5$ M s^{-1}, in the absence and in the presence of Az, respectively); whereas the corresponding k_{off} values resulted to be unchanged and consequently the corresponding equilibrium dissociation constant resulted to be increased (compare fourth to the first row of Table 1). In other words, all these SPR results indicate that the specific binding of Az to p53 induces a lowering of the association kinetics and binding affinity of the Mdm2–p53 complex, without obstructing the Mdm2 binding site on p53.

Interesting questions arise then about the mapping of the ternary interaction binding sites and, consequently, about the

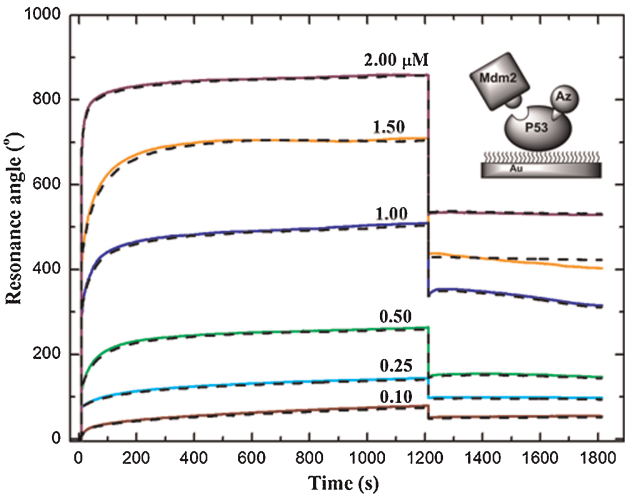

Figure 6. SPR sensorgrams for the binding process of Mdm2 with Az–p53 complex, with a cartoon of the interaction geometry. The SPR angle shift as function of time after injection and removal of the Mdm2 solutions (TST buffer, pH 7.2) at six concentrations is shown (solid profiles). Best fits (dashed black profiles) were obtained by using simultaneous nonlinear regression analysis to a reversible bimolecular interaction model (see details in the experimental procedures section).

mechanism of the Az action on the binding kinetics of the Mdm2–p53 complex.

Since it is well known that Mdm2 binds to p53 at its N-terminal transactivation domain (Kussie, 1996; Schon *et al*., 2002), the main issue regards the Az binding site of p53 which has not been, up to date, univocally identified. Indeed, it has been reported that Az can either bind the same N-terminal domain of p53 (Apiyo and Wittung-Stafshede, 2005; Gabellieri *et al*., 2009; Taranta *et al*., 2009) or its DBD (De Grandis *et al*., 2007). In the former case, however, it should be admitted, in the light of the present results, that Az would somehow affect the Mdm2–p53 recognition process without hindering the accessibility of Mdm2 to its binding pocket on p53. The latter possibility has been previously predicted by a docking study (De Grandis *et al*., 2007) and has very recently gained experimental ground from studies using the Az fragment p28 (aa 50–77) (Taylor *et al*., 2009), which has been found to retain *in vivo* the biochemical interaction and anticancer action of Az (Yamada *et al*., 2009).

Wherever Az is binding to p53, the protein is able to induce a weakening of the Mdm2–p53 interaction by a non competitive inhibition mechanism, which should be figured out as a long range binding regulation. In other words, we could admit the possibility that the observed change in the p53 folding could reflect an allosteric regulation mechanism by which Az may affect the p53 favourite conformation required for recruitment of the Mdm2–p53 complex (Boehr *et al*., 2009; Hilser, 2010).

Inhibition of the p53 interaction with the oncogenic protein Mdm2 is of utmost therapeutic value in cancer treatment. Up to date, the research has focused on therapeutic agents, natural or synthetic inhibitors (Klein and Vassilev, 2004) suitably designed for a competitive inhibition of Mdm2–p53 interaction by targeting the p53 binding site of Mdm2. However, such p53 activation pathway can lead to toxicity in normal tissues with relatively high proliferative index (Klein and Vassilev, 2004).

In this scenario, the evidenced allosteric inhibition mechanism of Mdm2–p53 interaction, could represent a novel biochemical rationale to design new drugs interacting with p53 for restoring its tumour suppressor activity. Indeed *in vivo* studies have shown that even a partial inhibition of Mdm2–p53 binding is sufficient to activate the p53 pathway, with low collateral effects (Klein and Vassilev, 2004).

CONCLUSION

Binding kinetics of the interaction between Az, Mdm2 and p53 full-length proteins has been here investigated by SPR. Our results provide novel molecular insights on the interaction between Az, p53 and Mdm2. They are consistent with previous reports on the occurrence of a specific binary complex between p53 and both Mdm2 and Az and point out the occurrence of a ternary interaction among these proteins, but go beyond these by providing the corresponding k_{off}, k_{on} and K_d values, thus evaluating the influence of Az on the Mdm2–p53 interaction kinetics. Collectively, the SPR analysis has revealed that Az induces a non competitive inhibition on the binding Mdm2–p53 by a significant reduction of their association rate constant. Moreover, the Az-induced folding in p53 evidenced by CD measurements, suggests that Az could be able to stabilize p53 by allosteric inhibition of the functional, regulative interaction between Mdm2 and p53. The highlighted non-competitive modulation of the p53 activity may represent an interesting, novel p53-activating strategy to design anticancer drugs to treat tumours in which p53 has retained its wild-type structure and function, and provides enlightening insights into the mechanism underlying the observed anticancer action of Az.

Acknowledgements

We are grateful to Prof. A. Congiu Castellano for providing circular dichroism equipment. F. Domenici thanks G. Funari for experimental support.

REFERENCES

Adman ET. 1991. Copper protein structures. *Adv. Protein Chem.* **42**: 145–197.

Andersson K, Hämäläinen M, Malmqvist M. 1999. Identification and optimization of regeneration conditions for affinity-based biosensor assays. A multivariate cocktail approach. *Anal. Chem.* **71**: 2475–2481.

Bom AP, Freitas MS, Moreira FS, Ferraz D, Sanches D, Gomes AMO, Valente AP, Cordeiro Y, Silva JL. 2010. The p53 Core domain is a molten globule at low pH: functional implication of a partially unfolded structure. *J. Biol. Chem.* **285**: 2857–2866.

Apiyo D, Wittung-Stafshede P. 2005. Unique complex between bacterial azurin and tumour-suppressor protein p53. *Biochem. Biophys. Res. Commun.* **332**: 965–968.

Bell S, Klein C, Müller L, Hansen S, Buchner J. 2002. p53 contains large unstructured regions in its native state. *J. Mol. Biol.* **322**: 917–927.

Bizzarri AR, Cannistraro S. 2010. The application of atomic force spectroscopy to the study of biological complexes undergoing to a biorecognition process. *Chem. Soc. Rev. (Critical Reviews)* **39**: 734–749.

Boehr DD, Nussinov R, Wright PE. 2009. The role of dynamic conformational ensembles in biomolecular recognition. *Nat. Chem. Biol.* **5**: 789–796.

Bossi G, Sacchi A. 2007. Restoration of wild-type p53 function in human cancer: relevance for tumor therapy. *Head Neck (basic science review)* **29**: 272–284.

Chi SW, Lee SH, Kim DH, Ahn MJ, Kim JS, Woo JY, Torizawa T, Kainosho M, Han KH. 2005. Structural details on mdm2-p53 interaction. *J. Biol. Chem.* **280**: 38795–38802.

Cooper MA. 2003. Label-free screening of bio-molecular interactions. *Anal. Bioanal. Chem.* **377**: 834–842.

Dahlman-Wright K, Baumann H, McEwan IJ, Almlof T, Wright AP, Gustafsson JA, Hard T. 1995. Structural characterization of a minimal functional transactivation domain from the human glucocorticoid receptor. *Proc. Natl. Acad. Sci. USA* **92**: 1699–1703.

Dawson R, Muller L, Dehner A, Klein C, Kessler H, Buchner J. 2003. The N-terminal domain of p53 is natively unfolded. *J. Mol. Biol.* **332**: 1131–1141.

De Grandis V, Bizzarri AR, Cannistraro S. 2007. Docking study and free energy simulation of the complex between p53 DNA-binding domain and azurin. *J. Mol. Recognit.* **20**: 215–226.

Dyson HJ, Wright PE. 2002. Coupling of folding and binding for unstructured proteins. *Curr. Opin. Struct. Biol.* **12**: 54–60.

Ferreon JC, Lee CW, Arai M, Martinez-Yamouta MA, Dyson HJ, Wright PE. 2009. Cooperative regulation of p53 by modulation of ternary complex formation with CBP/p300 and HDM2. *Proc. Natl. Acad. Sci. USA* **106**: 6591–6596.

Freedman DA, Wu L, Levine AJ. 1999. Functions of the Mdm2 oncoprotein. *Cell Mol. Life Sci.* **55**: 96–107.

Funari G, Domenici F, Nardinocchi L, Puca R, D'Orazi G, Bizzarri AR, Cannistraro S. 2010. Interaction of p53 with MDM2 and Azurin as studied by atomic force spectroscopy. *J. Mol. Recognit.* **23**: 343–351.

Gabellieri E, Bucciantini M, Stefani M, Cioni P. 2009. Spectroscopic characterization of the complex between azurin and p53 transactivation domain. *Eur. Biophys. J.* **38**: (suppl 1), s161.

Gannon JV, Greaves R, Iggo R, Lane DP. 1990. Activating mutations in p53 produce a common conformational effect. A monoclonal antibody specific for the mutant form. *EMBO J.* **9**: 1595–1602.

Hilser VJ. 2010. An ensemble view of allostery. *Science* **327**: 653–654.

Honda R, Tanaka H, Yasuda H. 1997. Oncoprotein Mdm2 is an ubiquitin ligase E3 for tumor suppressor p53. *FEBS Lett.* **420**: 25–27.

Iakoucheva LM, Brown CJ, Lawson JD, Obradović Z, Dunker AK. 2002. Intrinsic disorder in cell-signaling and cancer-associated proteins. *J. Mol. Biol.* **323**: 573–584.

Jianhong M, Martin JD, Zhang H, Auger KR, Ho TF, Kirkpatrick RB, Grooms MH, Johanson KO, Tummino PJ, Copeland RA, Lai Z. 2006. A second p53 binding site in the central domain of Mdm2 is essential for p53 ubiquitination. *Biochemistry* **45**: 9238–9245.

Klein C, Vassilev LT. 2004. Targeting the p53-MDM2 interaction to treat cancer. *Br. J. Cancer* **91**: 1415–1419.

Kumar R, Thompson EB. 2003. Transactivation functions of the N-terminal domains of nuclear hormone receptors: protein folding and co-activator interactions. *Mol. Endocrinol.* **17**: 1–10.

Kussie PH. 1996. Structure of the Mdm2 oncoprotein bound to the p53 tumor suppressor transactivation domain. *Science* **274**: 948–953.

Lai Z, Auger KR, Manubay CM, Copeland RA. 2000. Thermodynamics of p53 binding to hdm. 2 (1–126): effects of phosphorylation and p53 peptide length. *Arch. Biochem. Biophys.* **381**: 278–284.

Lavin MF, Gueven N. 2006. The complexity of p53 stabilization and activation. *Cell. Death Diff.* **13**: 941–950.

Legros Y, Meyer A, Oryt K, Soussi T. 1994. Mutations in p53 produce a common conformational effect that can be detected with a pane of monoclonal antibodies directed toward the central part of the p53 protein. *Oncogene* **9**: 3689–3694.

Moll UM, Petrenko O. 2003. The MDM2-p53 interaction. *Mol. Cancer Res.* **1**: 1001–1008.

Momand J, Zanbetti GP, Olson DC, George D, Levine AJ. 1992. The Mdm2 oncogene product forms a complex with the p53 protein and inhibits p53-mediated transactivation. *Cell* **69**: 1237–1245.

Morton TA, Myszka DG. 1998. Kinetic analysis of macromolecular interactions using surface plasmon resonance biosensors. *Meth. Enzymol.* **295**: 268–294.

Myszka DG, Morton TA, Doyle ML, Chaiken IM. 1997. Kinetic analysis of a protein antigen-antibody interaction limited by mass transport on an optical biosensor. *Biophys. Chem.* **64**: 127–137.

Nooren IMA, Thornton JM. 2003. Structural characterization and functional significance of transient protein-protein interactions. *J. Mol. Biol.* **325**: 991–1018.

Pontius BW. 1993. Close encounters: why unstructured, polymeric domains can increase rates of specific macromolecular association. *Trends Biochem. Sci.* **18**: 181–186.

Punj V, Bhattacharyya S, Saint-Dic D, Vasu C, Cunningham EA, Graves J, Yamada T, Constantinou AI, Christov K, White B, Li G, Majumdar D, Chakrabarty AM, Das Gupta TK. 2004. Bacterial cupredoxin azurin as an inducer of apoptosis and regression in human breast cancer. *Oncogene* **23**: 2367–2378.

Robert P, Benoliel AM, Pierres A, Bongrand P. 2007. What is the biological relevance of the specific bond properties revealed by single-molecule studies? . *J. Mol. Recognit.* **20**: 432–447.

Robert P, Limozin L, Pierres A, Bongrand P. 2009. Biomolecule association rates do not provide a complete description of bond formation. *Biophys. J.* **96**: 4642–4650.

Roth J, Dobbelstein M, Freedman DA, Shenk T. 1998. Nucleo-cytoplasmic shuttling of the hdm2 oncoprotein regulates the levels of the p53 protein via a pathway used by the human immunodeficiency virus rev protein. *EMBO J.* **2**: 554–564.

Schon O, Friedler A, Bycroft M, Freund SMV, Fersht AR. 2002. Molecular mechanism of the interaction between Mdm2 and p53. *J. Mol. Biol.* **323**: 491–501.

Taranta M, Bizzarri AR, Cannistraro S. 2008. Probing the interaction between p53 and the bacterial protein azurin by single molecule force spectroscopy. *J. Mol. Recognit.* **21**: 63–70.

Taranta M, Bizzarri AR, Cannistraro S. 2009. Modelling the interaction between the N terminal domain of the tumor suppressor p53 and azurin. *J. Mol. Recognit.* **22**: 215–222.

Taylor BN, Mehta RR, Yamada T, Lekmine F, Christov K, Chakrabarty AM, Green A, Bratescu L, Shilkaitis A, Beattie CW, Das Gupta TK. 2009. Noncationic peptides obtained from azurin preferentially enter cancer cells. *Cancer Res.* **69**: 537–546.

Toledo F, Wahl GM. 2006. Regulating the p53 pathway: *in vitro* hypotheses, *in vivo* veritas. *Nat. Rev. Cancer* **6**: 909–923.

Uversky VN. 2002. Natively unfolded proteins: a point where biology waits for physics. *Protein Sci.* **11**: 739–756.

Veprintsev DB, Freund SMV, Andreeva A, Rutledge SE, Tidow H, Cañadillas JMP, Blair CM, Fersht AR. 2006. Core domain interactions in full-length p53 in solution. *Proc. Natl. Acad. Sci. USA* **103**: 2115–2119.

Vise PD, Baral B, Latos AJ, Daughdrill GW. 2005. NMR chemical shift and relaxation measurements provide evidence for the coupled folding and binding of the p53 transactivation domain. *Nucleic Acid Res.* **33**: 2061–2077.

Vogelstein B, Lane D, Levine AJ. 2000. Surfing the p53 network. *Nature* **408**: 307–317.

Whitmore L, Wallace BA. 2004. DICHROWEB an online server for protein secondary structure analyses from circular dichroism spectroscopic data. *Nucleic Acid Res.* **32**: 668–673.

Yamada T, Goto M, Punj V, Zaborina O, Chen ML, Kimbara K, Majumdar D, Cunningham E, Das Gupta TK, Chakrabarty AM. 2002. Bacterial redox protein azurin, tumour suppressor protein p53, and regression of cancer. *Proc. Natl. Acad. Sci. USA* **99**: 14098–14103.

Yamada T, Hiraoka Y, Ikehata M, Kimbara K, Avner SB, Tapas KDG, Chakrabarty AM. 2004. Apoptosis or growth arrest: modulation of tumor suppressor p53's specificity by bacterial redox protein azurin. *Proc. Natl. Acad. Sci. USA* **101**: 4770–4775.

Yamada T, Fialho AM, Punj V, Bratescu L, Das Gupta TK, Chakrabarty AM. 2005. Internalization of bacterial redox protein azurin in mammalian cells: entry domain and specificity. *Cell. Microbiol.* **7**: 1418–1431.

Yamada T, Mehta RR, Lekmine F, Christov K, King ML, Majumdar D, Shilkaitis A, Green A, Bratescu L, Beattie CW, Das Gupta TK. 2009. A peptide fragment of azurin induces a p53-mediated cell cycle arrest in human breast cancer cells. *Mol. Cancer. Ther.* **8**: 2947–2958.